Heteronuclear Spin Decoupling Sequences with Frequency Sweep in Solid-State NMR Spectroscopy

Vinod Chandran C.
Max-Planck-Institut für Festkörperforschung
Stuttgart

Dissertation an der Universität Stuttgart
Stuttgart
December 2011

Heteronuclear Spin Decoupling Sequences with Frequency Sweep in Solid-State NMR Spectroscopy

Von der Fakultät Chemie der Universität Stuttgart
zur Erlangung der Würde eines
Doktors der Naturwissenschaften (Dr. rer. nat.)
genehmigte Abhandlung

Vorgelegt von

Vinod Chandran C.

aus Kerala, Indien

Hauptberichter:	Prof. Dr. Martin Jansen
Mitberichter:	Prof. Dr. Michael Hunger
Prüfungsvorsitzender:	Prof. Dr. Dietrich Gudat

Tag der mündlichen Prüfung: 19 - 12 - 2011

Max-Planck-Institut für Festkörperforschung, Stuttgart 2011

To my loving family

Acknowledgements

I would like to express my sincere gratitude to ***Prof. Dr. Dr. h. c. Martin Jansen*** *for giving me the opportunity to become a member of his research team, and to do my doctoral research in Max-Planck-Institute for Solid-State Research, Stuttgart. He has always been a great inspiration for me, since I started working in his department. His style of presenting basic concepts in chemistry and deep and wide scientific knowledge have always fascinated me. I am thankful to him for his short teaching sessions too.*

My sincere thanks to my Ph. D. examination committee members ***Prof. Dr. Dietrich Gudat*** *and* ***Prof. Dr. Michael Hunger*** *for the evaluation of my Ph. D. thesis.*

I have worked under the guidance of ***Dr. Thomas Bräuniger*** *during my Ph. D. I wish to thank him whole-heartedly for taking me into his small NMR group, and then for finding interesting projects for me. I would like to thank him for his timely advices, constant motivation, frequent work discussions and all scientific and non-scientific conversations. I would also like to thank him for his excellent solid-state NMR lectures and for numerous suggestions on my writing and communicating styles. I thank you for being with me, in my professional and personal life, from the very first day in Leipzig Airport until today.*

I am very grateful to ***Prof. Dr. Kay Saalwächter*** *for allowing me to work in his research group, and for his wonderful NMR courses, in Martin-Luther-University of Halle-Wittenberg in the beginning of my Ph. D.*

Now I would like to thank ***Prof. P. K. Madhu*** *(TIFR, Mumbai),* ***Dr. Philip Wormald*** *(Uni - St. Andrews),* ***Dr. N. D. Kurur*** *(IIT, New Delhi) and* ***Dr. R. S. Thakur*** *(CSMCRI, Gujrat) for their help, advices, suggestions and successful research collaborations throughout my Ph. D. Thanks to* ***Prof. P. K. Madhu*** *again for his invitation to visit TIFR and hospitality.*

I would like to thank ***PD Dr. Detlef Reichert*** *and* ***Dr. Günter Hempel*** *(Uni-Halle) for their help, scientific collaborations, and advices.*

I would like to thank ***Dr. Ulrich Wedig*** *for his help in theoretical calculations and successful collaborations.*

I became fascinated to NMR, when I was doing my bachelor degree. Thanks to those lectures from ***Dr. Ushayamma Thomas****,* ***Dr. Jayasree****,* ***Dr. Johns Micheal****,* ***Dr. N. F. Francis*** *and* ***Dr. Rosily Mathew*** *(University of Kerala, Thiruvananthapuram).*

*During my masters, I was inspired by the philosophical lectures of **Prof. Pius Kuruvila** and **Prof. Ibnu Saud** (Mahatma Gandhi University, Kottayam). Many thanks to them. I would also like to thank **Dr. C. V. Ashokan**, **Prof. P. K. Radhakrishnan**, **Prof. A. S. Padmanabhan**, **Prof. M. Padmanabhan**, **Prof. Sabu Thomas** and **Prof. P. Madhavan Pillai** (MGU Kottayam).*

*The very first NMR experiment I did was with **Dr. P. R. Rajamohanan** (NCL, Pune), for my master thesis. I would like to express my sincere gratitude to him.*

*I would like to thank **Dr. S. Ganapathy**, with whom I worked as a project assistant. Thanks to him for my worth stay in NCL, Pune.*

*I would also like to thank **Dr. T. G. Ajithkumar**, for his help, suggestions and many research collaborations, and for his kind invitation to NCL and hospitality.*

*Now, I thank my friends who encouraged me in my career. **Ajayan**, **Babu** & **Sarith** are the firsts to mention. They are always remembered.*

*Thanks to friends from MGU. : **Padmesh**, **Renji**, **Vivek**, **Habeeb**, **Jousheed**, **Sreekumar**, **Sudhindran**, **Resmi**, **Shyla**, **Rani** & **Preetha**.*

*Thanks to friends from NCL. : **Deepak**, **Prinson**, **Kavitha**, **Surendran**, **Sarish**, **Smitha**, **Sreeprasanth**, **Rajsankar**, **Joly**, **Anesh**, **Jinto**, **Vinod**, **Sumesh**, **Hari**, **Eldho** & **Sabari**. Special thanks to **V. T. Sathe** & **K. D. Deshpande**.*

*Thanks to friends from Halle : **Juan**, **Fabian**, **Irene**, **Ovidiu**, **Cornalius**, **Frank**, **Walter**, **Anja**, **Christiane** & **Kerstin**. Thanks to friends in MPI. : **Andreas**, **Florian**, **Aniket**, **Prasad**, **Nico**, **Karolin**, **Moritz**, **Katarina**, **Sridhar**, **Vanya**, **Naveed**, **Hasan**, **Frank**, **Dennis** & **Caterina**. Special thanks to **Sabine**, **Florian** & **Moritz** for bureaucratic and technical assistance.*

*Many thanks to the **Deutsche Forschungsgemeinschaft** (DFG grants: **BR 3370/4-1, BR 3370/5-1**) for funding and **University of Halle**, Experimental Physics Institute of **Leipzig University** and **Max-Planck-Society** for providing time and space dimensions to my Ph. D. project. Also, partial funding by the **German Ministry of Research (BMBF)** within project **03KP801, "Elektrochemie für Elektromobilität - Verbund Süd"**, is gratefully acknowledged.*

*None of my achievements would have been possible without the support and affection of my family. Thanks to my father (**Chadrasekharan Nair. D**), mother (**Vijayakumari. R**) and brother (**Vineeth Chandran. C**) for supporting and letting me free to find my way of life. Last, but never the least, thanks to my wife **Dr. Resmi Mohan**, who has always been there as a source of inspiration to me.*

...

Vinod Chandran C.

Abstract

Solid-state Nuclear Magnetic Resonance (NMR) plays an increasingly important role in characterization of technologically relevant materials, such as ceramics, catalysts and glasses, primarily because of its capability to selectively probe the local environment of atomic nuclei. A major concern in NMR is spectral resolution, which may dramatically be improved by the application of heteronuclear spin decoupling, i.e. irradiation of a abundant nuclei (e.g. ^{1}H, ^{19}F) coupled to the observed rare nucleus (e.g. ^{13}C, ^{15}N). In solid-state NMR, the dipolar coupling between nuclei may be suppressed by multi-pulse sequences like Two-Pulse Phase Modulation (TPPM) and Small Phase Incremental ALteration (SPINAL) which show better decoupling efficiency than the Continuous Wave (CW) method. This thesis discusses the design and application of frequency-swept heteronuclear spin decoupling methods in solid-state NMR. A frequency sweep is implemented by defined increment of the pulse durations within the sequence. This concept was originally suggested by P. K. Madhu and coworkers in 2006, and termed SW$_f$-TPPM. The SW$_f$-TPPM sequence consistently outperforms the conventional non-swept TPPM and SPINAL sequences in ^{1}H decoupling efficiency and robustness towards NMR parameter changes, as shown by P. K. Madhu and coworkers using both experiments and numerical simulations. In the current work, we have investigated the dependence of decoupling performance on the sweep profile of SW$_f$-TPPM. It was found that linear sweeps work as efficiently as tan-shaped sweeps, but are easier to optimize. The influence of the sweep direction was also investigated by both experiment and theoretical Floquet analysis, and it could be shown that the decoupling efficiency is independent of the sweep direction. Furthermore, we have extended the frequency-sweep principle to the original SPINAL method, thereby creating the SW$_f$-SPINAL sequence. The new method delivers very good ^{1}H decoupling performance for rigid

organic solid systems and quadrupolar nuclei. Currently, it is one of the best sequences available for decoupling in partially ordered systems, as demonstrated on a liquid crystalline model compound. Also, a systematic investigation of the performance of TPPM, SPINAL and frequency-swept decoupling methods for ^{19}F was undertaken for the first time. The necessity for efficient decoupling of ^{19}F occurs frequently in solid-state NMR, as fluorine is present in many important materials like polymers, minerals, and ion conductors. ^{19}F is especially demanding for decoupling because of its chemical shielding effects are much larger than those observed for ^{1}H, on account of a significantly higher number of electrons in the system. By both experiment and numerical simulations, it is shown here that the improved decoupling efficiency of SW$_f$-TPPM and SW$_f$-SPINAL does also exist for ^{19}F decoupling of rigid organic solids.

In the context of structural studies of inorganic solids, NMR of quadrupolar nuclei such as ^{23}Na ($I = \frac{3}{2}$), ^{27}Al ($I = \frac{5}{2}$) and ^{45}Sc ($I = \frac{7}{2}$) becomes important. NMR characterization of these nuclides is usually limited to acquiring the central-transition signal, which is broadened by the quadrupolar interaction to second order. This second-order broadening can be eliminated only by the application of specialised NMR techniques, such as multiple-quantum magic-angle spinning (MQMAS). Additional broadening may be caused by dipolar interaction to the abundant spin-$\frac{1}{2}$ nuclei ^{1}H and ^{19}F, which can be suppressed by heteronuclear decoupling. The necessity for efficient decoupling of ^{19}F occurs, for example, in NMR investigations of ion conductors, as in many of them, fluorine is found in close vicinity of quadrupolar nuclei like ^{7}Li, ^{23}Na or ^{133}Cs. There is a definite advantage of using efficient ^{1}H and ^{19}F decoupling during multiple-quantum (MQ) evolution in half-integer spin quadrupolar systems, as for a MQ transition of coherence order p, the de-phasing of the MQ signal caused by the dipolar interaction is p-fold amplified. Thus, MQMAS spectra are an ideal proving ground for the quality of decoupling sequences. In the present work, we have demonstrated that the frequency-swept sequences were most efficient for ^{1}H decoupling of ^{45}Sc 3QMAS and 5QMAS of scandium sulphate pentahydrate (shortened as ScSPH) and ^{19}F decoupling of ^{23}Na 3QMAS of cryolite.

In addition to the method-oriented research related to heteronuclear spin decoupling, we have also carried out solid-state NMR investigation of some inorganic compounds. The NMR parameter (chemical shift and quadrupolar) determination of ScSPH ($Sc_2(SO_4)_3.5H_2O$), aluminium carbide (Al_4C_3), strontium aluminate ($SrAl_{12}O_{19}$) and aluminium oxide (Al_2O_3) deposited on spider silk was done with the help of various NMR techniques. For ScSPH and Al_4C_3, a combination of NMR experiments and DFT calculations helped in unambiguous site assignments.

Zusammenfassung

Festkörper-Kernresonanzspektroskopie (NMR) ermöglicht es, die lokale Umgebung von Atomkernen zu erkunden, und spielt daher eine immer bedeutendere Rolle bei der Charakterisierung von technologisch wichtigen Materialien wie Keramiken, Katalysatoren und Gläsern. Ein wichtiges Anliegen in der NMR-Spektroskopie ist die spektrale Auflösung, welche durch Anwendung von heteronuklearer Spin-Entkopplung oft drastisch verbessert werden kann, d.h. durch Radiofrequenz-Bestrahlung des Nuklides mit hoher natürlicher Häufigkeit (z.B. ^{1}H, ^{19}F), welches mit dem beobachteten Spin (z.B. ^{13}C, ^{15}N) koppelt. In der Festkörper-NMR werden dipolare Kopplungen üblicherweise durch Anwendung von Multi-Impuls-Sequenzen wie "Two-Pulse Phase Modulation" (TPPM) oder "Small Phase Incremental ALteration" (SPINAL) unterdrückt, wobei die Multi-Impuls-Sequenzen eine deutlich höhere Entkopplungseffizienz aufweisen als die herkömmliche Einfrequenz-Einstrahlung (CW-Continuous Wave). In der vorliegenden Arbeit werden Entwurf und Festkörper-NMR-Anwendungen von Multi-Impuls-Sequenzen mit inhärentem Frequenzdurchlauf ("sweep") diskutiert. Die Generierung eines Frequenzdurchlaufes in Multi-Impuls-Sequenzen wird durch definierte Inkrementierung der Impulslänge erreicht, und wurde im Jahr 2006 von der Arbeitsgruppe von P.K. Madhu vorgeschlagen. Die TPPM-Sequenz mit Frequenzdurchlauf wurde als SW$_f$-TPPM bezeichnet, und zeigte in verschiedenen Systemen eine im Vergleich zu TPPM und SPINAL verbesserte Entkopplungseffizienz, wie von P.K. Madhu und Mitarbeitern durch zahlreiche Experimente und numerische Simulationen demonstriert wurde. In der hier vorgestellten Arbeit wird unter anderem die Abhängkeit der SW$_f$-TPPM Entkopplungseffizienz von der Form des Frequenzprofils untersucht. Es konnte gezeigt werden, dass lineare Profile den ursprünglich vorgeschlagenen Profilen mit tan(x)-Form in Leistung ebenbürtig , aber einfacher zu implementieren und zu optimieren sind.

Auch die Abhängigkeit der Entkopplerleistung von der Richtung des Frequenzdurchlaufes wurde untersucht. Durch experimentelle Daten und Analyse mittels Floquet-Theorie konnte nachgewiesen werden, dass die Entkopplungseffizienz von SW$_f$-TPPM unabhängig von der Durchlaufrichtung ist. Weiterhin wurde in der vorliegenden Arbeit das Prinzip des Frequenzdurchlaufes auf die Entkopplungssequenz SPINAL übertragen, wodurch die neue SW$_f$-SPINAL-Sequenz entstand. Diese Sequenz zeigt gute Entkopplungseigenschaften für organische Festkörper und Systeme mit Quadrupolkernen. SW$_f$-SPINAL ist momentan eine der besten verfügbaren Entkopplungsmethoden für NMR-Untersuchungen von teilgeordneten Systemen, wie an einer flüssigkristallinen Modellsubstanz gezeigt werden konnte. Systematische Untersuchungen wurden außerdem ausgeführt zur Leistung von TPPM, SPINAL, SW$_f$-TPPM und SW$_f$-SPINAL für die Spinentkopplung von ^{19}F. Die Notwendigkeit zur Anwendung effizienter ^{19}F-Entkopplung tritt in der Festkörper-NMR häufig auf, da Fluor Bestandteil vieler wichtiger Materialien wie organischer Polymere, Minerale und Ionenleiter ist. Effektive Entkopplung von ^{19}F stellte eine besondere Herausforderung dar, da die Effekte der chemischen Verschiebung durch die höhere Elektronenanzahl bei Fluor viel stärker sind als bei Protonen. Sowohl durch experimentelle Daten als auch durch numerische Simulationen konnte nachgewiesen werden, dass die überlegene Entkopplungseffizienz von SW$_f$-TPPM und SW$_f$-SPINAL auch für ^{19}F-Entkopplung in organischen Festkörpern existiert.

Im Kontext von Strukturuntersuchungen anorganischer Festkörper ist die NMR-Spektroskopie von Quadrupolkernen wie ^{23}Na ($I = \frac{3}{2}$), ^{27}Al ($I = \frac{5}{2}$) und ^{45}Sc ($I = \frac{7}{2}$) wichtig. Die NMR-Charakterisierung solcher Nuklide beschränkt sich in den meisten Fällen darauf, die Resonanzlinie des Zentralüberganges aufzunehmen, welche durch die Quadrupolwechselwirkung zweiter Ordnung verbreitert ist. Diese Verbreiterung kann nur durch Anwendung spezieller NMR-Methoden, z.B. der "multiple-quantum magic-angle spinning" (MQMAS) Methode eliminiert werden. Zusätzliche Linienverbreiterung wird oft durch die dipolare Wechselwirkungen mit Nukliden wie ^{1}H und ^{19}F ($I = \frac{1}{2}$) verursacht. Die dipolare Verbreiterung kann durch Anwendung von Impulsfolgen zur heteronuklearen Spinentkopplung unterdrückt werden. Dieses Szenario besteht beispielsweise bei der NMR-Charakterisierung von Ionenleitern, in denen sich oft Fluor in unmittelbarer Nachbarschaft zu Quadrupolkernen wie ^{7}Li, ^{23}Na oder ^{133}Cs befindet. Die Nutzung effizienter ^{1}H- und ^{19}F-Entkopplung ist während der Evolutionszeit der MQMAS-Methode besonders vorteilhaft, da für eine MQ-Kohärenz der Ordnung p die Dephasierung des Signals durch die dipolare Wechselwirkung p-fach verstärkt wird. Damit sind MQMAS-Spektren von geeigneten Systemen eine ideale Versuchsumgebung zum Testen von Entkopplungssequenzen. In der vorliegenden Arbeit wird gezeigt, das die Impulssequenzen mit Frequenzdurchlauf am effektivsten bei der Entkopplung von ^{1}H für ^{45}Sc-3QMAS und 5QMAS von $Sc_2(SO_4)_3.5H_2O$, und für die Entkopplung von ^{19}F bei der Aufnahme von ^{23}Na-3QMAS von Na_3AlF_6 sind.

Zusätzlich zum methodenorientierten Teil über heteronukleare Spinentkopplung wurden Festkörper-NMR-Untersuchungen von einigen anorganischen Verbindungen durchgeführt. Die NMR-Parameter für chemische Verschiebung und Quadrupolkopplung wurden bestimmt für die Substanzen Scandiumsulfatpentahydrat ($Sc_2(SO_4)_3.5H_2O$), Aluminiumkarbid (Al_4C_3), Strontiumaluminat ($SrAl_{12}O_{19}$) und für auf Spinnenseide aufgedampftes Aluminiumoxid (Al_2O_3). Sowohl für Sc-SPH als auch für Al_4C_3 wurden ausserdem Dichtefunktionalrechnungen durchgeführt, die die Zuordnung der NMR-Signale zu den Kristallgitterplätzen ermöglichten.

List of Abbreviations

5CB	4-n-pentyl-4'-cyanobiphenyl
CPD	Composite Pulse Decoupling
CP	Cross Polarization
C_Q	Quadrupole Coupling constant
CSA	Chemical Shift Anisotropy
CT	Central Transition
CW	Continuous Wave
DAS	Dynamic Angle Spinning
DFT	Density Functional Theory
DOR	DOuble Rotation
EFG	Electric Field Gradient
FAM	Fast Amplitude Modulation
FWHM	Full-Width Half-Maximum
MAS	Magic-Angle Spinning
MQMAS	Multiple-Quantum Magic-Angle Spinning
NMR	Nuclear Magnetic Resonance
NFBS-K	potassium nonafluoro-1-butanesulfonate
PAS	Principal Axis System
PFP-Na	sodium pentafluoro propionate
P_H	Hard Pulse
P_H^{con}	Hard Pulse for Conversion
P_H^{exc}	Hard Pulse for Excitation
RF	Radio-Frequency
ScSPH	Scandium Sulphate PentaHydrate
SPINAL	Small Phase Incremental ALteration
SSB	Spinning Side-Band
ST	Satellite Transition
SW_f^{for}	Forward Frequency Sweep
SW_f^{lin}	Linear Frequency Sweep
SW_f^{rev}	Reverse Frequency Sweep
SW_f-SPINAL	Frequency-Swept SPINAL
SW_f^{tan}	Tangential Frequency Sweep
SW_f-TPPM	Frequency-Swept TPPM
TPPM	Two Pulse Phase Modulation
XRD	X-Ray Diffraction

Publications

List of publications related to the thesis:

1. C. V. Chandran, P. K. Madhu, N. D. Kurur, T. Bräuniger, Swept-frequency two-pulse phase modulation (SW$_f$-TPPM) sequences with linear sweep profile for heteronuclear decoupling in solid-state NMR, Magn. Reson. Chem. 46 (2008) 943–947 [read].
2. S. M. Lee, E. Pippel, U. Gösele, C. Dresbach, Y. Qin, C. V. Chandran, T. Bräuniger, G. Hause, M. Knez, Greatly increased toughness of infiltrated spider silk, Science 324 (2009) 488–492 [read].
3. C. V. Chandran, T. Bräuniger, Efficient heteronuclear dipolar decoupling in solid-state NMR using frequency-swept SPINAL sequences, J. Magn. Reson. 200 (2009) 226–232 [read].
4. K. Harindranath, K. A. Viswanath, C. V. Chandran, T. Bräuniger, P. K. Madhu, T. G. Ajithkumar, P. A. Joy, Evidence for the co-existence of distorted tetrahedral and trigonal bipyramidal aluminium sites in $SrAl_{12}O_{19}$ from ^{27}Al NMR studies, Solid State Commun. 150 (2010) 262–266 [read].
5. C. V. Chandran, J. Cuny, R. Gautier, L. Le Polles, C. J. Pickard, T. Bräuniger, Improving sensitivity and resolution of MQMAS spectra: A ^{45}Sc-NMR case study of scandium sulphate pentahydrate, J. Magn. Reson. 203 (2010) 226-235 [read].
6. C. V. Chandran, P. K. Madhu, P. Wormald, T. Bräuniger, Frequency-swept pulse sequences for ^{19}F heteronuclear spin decoupling in solid-state NMR, J. Magn. Reson. 206 (2010) 255-263 [read].
7. S. Paul, C. V. Chandran, T. Bräuniger, P. K. Madhu, Sweep direction and efficiency of the swept-frequency two pulse phase modulated scheme for heteronuclear dipolar-decoupling in solid-state NMR, J. Magn. Reson. 209 (2011) 261–268 [read].
8. T. Bräuniger, C. V. Chandran, U. Wedig, M. Jansen, NMR chemical shift and quadrupolar interaction parameters of carbon-coordinated ^{27}Al in aluminium carbide, Al_4C_3, Z. Anorg. Allg. Chem. 637 (2011) 530–535 [read].
9. C. V. Chandran, G. Hempel, T. Bräuniger, ^{19}F decoupling of half-integer spin quadrupolar nuclei in solid-state NMR: Application of frequency-swept decoupling methods, Solid State Nucl. Magn. Reson. 40 (2011) 84–87 [read].

Contents

Contents **xvii**

List of Figures **xxi**

1 Introduction **1**

1.1 NMR Phenomena: Basic Principles 2
1.2 NMR Interactions 10
1.2.1 The *Zeeman* interaction 11
1.2.2 The Radio-frequency field 12
1.2.3 The chemical shift 12
1.2.4 The direct dipole-dipole interaction 15
1.2.5 The scalar spin-spin coupling 19
1.3 Resolution and Sensitivity in Solid-State 20
1.3.1 Magic-angle spinning 20
1.3.2 Cross-polarization 23

2 Spin Decoupling **24**

2.1 Introduction 24
2.2 Origin of Line Broadening in Solid State 26
2.3 Decoupling methods in Solid State 27
2.3.1 Continuous wave (CW) decoupling 27
2.3.2 Two pulse phase modulation (TPPM) 28
2.3.3 Small phase incremental alteration (SPINAL) 29
2.3.4 Other decoupling sequences 30
2.4 Dipolar Decoupling Related Phenomena 31

2.4.1 Interaction between *RF* field and MAS 31
2.4.2 Second-order recoupling of chemical shielding and dipolar coupling 32
2.4.3 Effect of MAS on abundant spin network 34
2.4.4 Off-resonance behavior of decoupling 35

3 Frequency-Swept TPPM 37
3.1 Introduction 37
3.2 Frequency Sweep Profiles 37
3.2.1 Tangent sweep profiles 38
3.2.2 Linear Frequency Sweeps 40
3.3 Improved efficiency of frequency-swept decoupling 46
3.4 Frequency Sweep Direction 47
3.4.1 Floquet analysis 50

4 Frequency-Swept SPINAL 52
4.1 Introduction 52
4.2 Design of Sequences 53
4.3 Applications 54
4.3.1 Rigid Solids 55
4.3.2 Liquid Crystals 59
4.4 Numerical Simulations 61

5 ^{19}F Decoupling 65
5.1 Introduction 65
5.1.1 Experimental details 68
5.2 Decoupling in Rigid Solids 69
5.3 Numerical Simulations 73
5.4 ^{19}F Decoupling: Reversal of sweep direction 76

6 Decoupling while Observing Quadrupolar Nuclei 79
6.1 NMR of Quadrupolar Nuclei 79
6.2 Solid-state NMR of ^{27}Al 83
6.2.1 Aluminium carbide 83

6.2.2 Strontium aluminate 84
6.2.3 Aluminium oxide deposited spider-silk 84
6.2.4 Need of a high-resolution method 85
6.3 Solid-state NMR of ^{45}Sc 86
6.3.1 Multiple-Quantum Magic-Angle Spinning 86
6.3.2 MQMAS Sensitivity enhancement 88
6.3.3 Solid-state NMR and DFT calculations 90
6.4 Spin Decoupling during MQ Evolution 92
6.4.1 Proton decoupling 92
6.4.2 Fluorine decoupling 95

7 Conclusions **101**

Appendix **105**

References **109**

List of Figures

1.1 A schematic representation of Zeeman interaction for a nuclear spin with $I = \frac{1}{2}$. 3
1.2 The net magnetization vector $\vec{M}$ aligned along $\vec{B}_0$ in the static frame. 4
1.3 The Fourier analysis of RF pulses with different pulse durations (τ_p). 5
1.4 The net magnetization vector $\vec{M}$ precesses about $\vec{B}_0$ in the static frame. 6
1.5 The effect of RF pulse on the net magnetization vector $\vec{M}$ in the rotating frame. 7
1.6 The Fourier transform of (a) *sine* function is (c) a single frequency line, while for an (b) exponentially modified *sine* function the FT is (d) a Lorentzian. 8
1.7 The effect of 90° and 180° RF pulses on the net magnetization vector $\vec{M}$ in the rotating frame. 9
1.8 The sinusoidal dependence of the signal intensity with pulse duration. 10
1.9 A schematic chemical shift anisotropy (CSA) pattern of a spin $I = \frac{1}{2}$ system with $\eta_{CS} = 0.25$. 15
1.10 A diagrammatic representation of dipole-dipole interaction. 16
1.11 A dipole ”Pake doublet”, which is composed of two sub-spectra resulting from the two spin states of the coupled nuclei. 18
1.12 A schematic representation of Magic-Angle Spinning (MAS). . . . 21

1.13 An experimental ^{13}C NMR spectrum of solid alanine showing the effect of magic-angle spinning (MAS) at a magnetic field of strength 9.4 T. The anisotropic chemical shielding and dipolar effects are getting averaged, as the MAS frequency increases, from a static case (bottom) to 8 kHz MAS (top). The mechanical averaging is reflected by the gradual disappearance of the spinning side-bands (SSB). 22

2.1 The schematic representation of spin decoupling of the abundant spin (I) to observe the rare spin (S) using a long Continuous Wave (CW) irradiation in the I spin channel. 25

2.2 The schematic representation of Two-Pulse Phase Modulation (TPPM) decoupling pulse sequence with alternating pulses having inverse phase modulation ($+\phi$ and $-\phi$). 29

2.3 The schematic representation of the basic block of Small Phase Incremental ALteration (SPINAL) decoupling pulse sequence with alternating pulses having inverse phase modulation ($+\phi$ and $-\phi$) and with phase increments α and β. 30

2.4 The angular dependence behavior of second and fourth rank dipolar-chemical shielding recoupling interactions scaling like Legendre polynomials of the order two (grey) and four (black) respectively. 34

2.5 A schematic representation of (a) Lorentzian line shape of the S spin NMR signal under TPPM decoupling. The peak height (intensity) decreases and the full-width at half-maximum (FWHM) increases, while the decoupler (I spin) offset ($\Delta\nu_{RF}$) moves away from the *on-resonance* condition. The dependence of the S spin (b) intensity and (c) FWHM on the decoupler offset is also shown. 35

3.1 The schematic representation of SW$_f$-TPPM decoupling pulse sequence. 38

3.2 The tangential sweep profiles of SW$_f^{tan}$-TPPM decoupling sequence. 39

3.3 The Linear sweep profiles of SW$_f^{lin}$-TPPM decoupling sequence. . 41

3.4 Intensities of the ^{13}CH$_2$ resonance of crystalline tyrosine as a function of decoupler frequency offset at 10 kHz MAS.The methods compared are (■) TPPM, (□) SPINAL-64, (●) SW$_f^{lin}$-TPPM and (○) SW$_f^{tan}$-TPPM decoupling sequences. 42

3.5 (a) Plot of (^{13}CH$_2$ of tyrosine) summed intensities η as a function of sweep ranges d for SW$_f$-TPPM sequences with tangential sweep profile (○) and with linear sweep profile (●). For comparison, the d-independent ηs for TPPM (■) and SPINAL-64 (□) are also shown. (b) Intensities of the ^{13}CH$_2$ resonance of tyrosine as a function of pulse duration τ_p offset at 10 kHz MAS at optimal decoupler frequency. 43

3.6 (a) Plot of summed intensities η of the ^{13}CH$_2$ resonance of tyrosine as a function of the cut-off angle t_{co}, obtained with the SW$_f^{tan}$-TPPM sequence at 10 kHz MAS rate. Best performance is achieved for $t_{co} = 50°$. (b) Best sweep ranges d for the decoupling sequences SW$_f^{tan}$-TPPM (○), and SW$_f^{lin}$-TPPM profile (●), as a function of MAS rate. 44

3.7 SPINEVOLUTION numerical simulations of comparison of ^{1}H decoupling efficiencies of TPPM (top left), SPINAL-64 (top right), SW$_f^{lin}$-TPPM (bottom left) and SW$_f^{tan}$-TPPM (bottom right) in a system of one ^{13}C dipolar-coupled with four ^{1}Hs. Plotted are the ^{13}C signal intensities (increase from green to red) as a function of phase angles (ϕ) of the decoupling sequence and the range of RF strengths (ν_1). 45

3.8 The SW$_f$-TPPM decoupling sequence with (a) forward (SW$_f$-for-TPPM) and (b) reverse (SW$_f$-rev-TPPM) sweep profiles. 48

3.9 (a) Comparison ^{13}C CPMAS spectra of tyrosine acquired with (i) SW$_f$-for-TPPM and (ii) SW$_f$-rev-TPPM decoupling sequences with linear sweep profiles (b) Decoupler offset dependence of SW$_f$-for-TPPM (▷) and SW$_f$-rev-TPPM (◀) decoupling sequences as a function of ^{13}CH$_2$ signal intensities of tyrosine. 48

3.10 SPINEVOLUTION numerical simulations of comparison of ^{1}H decoupling efficiencies of SW$_f$-for-TPPM (left) and SW$_f$-rev-TPPM (right) in a system of one ^{13}C dipolar-coupled with four ^{1}Hs. Plotted are the ^{13}C signal intensities as a function of phase angles (ϕ) of the decoupling sequence and the range of RF strengths (ν_1). . . 49

4.1 The schematic representation of SW$_f$-SPINAL decoupling pulse sequence. 53

4.2 ^{1}H off-resonance effects for the ^{13}C resonance from the methylene group of L-tyrosine hydrochloride molecule obtained with several SW$_f$-SPINAL decoupling methods with (a) different SPINAL basic units and (b) with different SPINAL-64 sweep units obtained from its ^{13}C CPMAS spectrum at 10 kHz MAS frequency. 57

4.3 (a) The L-tyrosine hydrochloride molecule and (b) its ^{13}C CPMAS spectrum of the aliphatic region. The ^{1}H off-resonance effects were studied for all the ^{13}C resonances for a range of MAS spinning frequencies and that of (c) the methylene carbon at 8 kHz MAS is shown along with (d) the MAS frequency dependence of the ^{13}C signal intensity. A figure-of-merit parameter η is introduced here, with $\eta = I_{0kHz} + I_{2kHz} + I_{4kHz} + I_{6kHz}$, where I_{xkHz} is the absolute intensity of the CH$_2$ signal at x kHz ^{1}H offset. 58

4.4 (a) The 4-n-pentyl-4'-cyanobiphenyl (5CB) molecule and (b) its ^{13}C static CP spectrum of the aliphatic region. The ^{1}H off-resonance effects were studied for all the ^{13}C resonances and those of (c) α-carbon and (d) γ-carbon are shown. 60

4.5 The results of SPINEVOLUTION [84] simulations (a) SW$_f^{lin}$(08)-SPINAL-08 (b) SW$_f^{lin}$(16)-SPINAL-16 (c) SW$_f^{lin}$(32)-SPINAL-32 and (d) SW$_f^{lin}$(64)-SPINAL-64, being plotted as the absolute intensity of the ^{13}C resonance as a function of RF strength ν_1 and the phase angle ϕ. A four-proton system dipolar-coupled with ^{13}C was assumed for the simulations, and a MAS frequency of 8.3333 kHz was used. 62

4.6 The results of SPINEVOLUTION [84] simulations of (a) SW_f^{lin}-TPPM and (b) SW_f^{lin}(32)-SPINAL-32, being plotted as the absolute intensity of the ^{13}C resonance as a function of *RF* strength ν_1 and the phase angle ϕ. A four-proton system dipolar-coupled with ^{13}C was assumed for the simulations, where a MAS frequency of 8.3333 kHz was used for SW_f-SPINAL and 9.0909 kHz for SW_f-TPPM. . 63

5.1 ^{19}F decoupled ^{13}C CPMAS spectra of (top row) CF_2 and CF_3 groups of sodium pentafluoropropionate (PFP-Na) and (bottom row) potassium nonafluoro-1-butanesulfonate (NFBS-K). Decoupling performance of TPPM, SPINAL, SW_f-TPPM and SW_f-SPINAL are compared for both model compounds. All the spectra were collected at an MAS frequency of 10 kHz, with the decoupler frequency being *on-resonance*. 70

5.2 The ^{19}F *off-resonance* effects are shown for the ^{13}C CPMAS spectra of NFBS-K for the signals from (a) α, (b) δ, (c) β and (d) γ-carbons. Decoupling performance of TPPM, SPINAL, SW_f-TPPM and SW_f-SPINAL are compared based on the ^{19}F offset dependence at a MAS frequency of 10 kHz. 71

5.3 The decoupling performance at different MAS frequencies are compared here by plotting the full-width at half-maximum (FWHM) of the ^{13}C CPMAS signals from (a) α, (b) δ, (c) β and (d) γ-carbons of NFBS-K for different decoupling sequences, namely TPPM, SPINAL, SW_f-TPPM and SW_f-SPINAL at 10, 15 and 20 kHz MAS. Here, in contrast to intensity plots, lower values (i.e., narrower lines) indicate better decoupling. 72

5.4 The 2D representation of SPINEVOLUTION [84] simulations of TPPM (top left), SW$_f^{lin}$-TPPM (bottom left): (both with 8.0808 kHz MAS); and SPINAL-64 (top right), SW$_f^{lin}$-SPINAL(bottom right): (both with 8.3333 kHz MAS) being plotted as the absolute intensity of the ^{13}C resonance as a function of RF strength (ν_1) and the phase angle (ϕ). A structural unit of 4 fluorines (^{19}F, with $\Delta\delta$ = 16 kHz) dipolar-coupled with a ^{13}C ($\Delta\delta = 0$ kHz) was used for the calculations. 73

5.5 SPINEVOLUTION [84] simulations showing the decoupling performance of (i) SPINAL-64, (ii) SW$_f^{lin}$-SPINAL and (iii) SW$_f^{lin}$-TPPM sequences plotted as a function of (a) the highest intensity values in the 2D plot and (b) the collapsed (summed) intensities of the 2D landscapes, normalized by the matrix size. The decoupling performance was calculated for different chemical shielding anisotropies, $\Delta\delta$ = 8, 16, 32, and 64 kHz. 74

5.6 SPINEVOLUTION [84] simulations showing the decoupling performance of SPINAL-64, SW$_f^{lin}$-SPINAL and SW$_f^{lin}$-TPPM sequences plotted as a function of the collapsed (summed) intensities of the 2D landscapes of phase angles (ϕ) and RF strengths (ν_1) normalized by the matrix size. The ^{19}F parameters for the four fluorine in the structural units were: (a) $\Delta\delta$ = 0 kHz; $d\delta_{iso}$ = 16 kHz (with δ_{iso} = −8, −8, +8, +8 kHz) and (b) $\Delta\delta$ = 16 kHz; $d\delta_{iso}$ = 0 kHz (with δ_{iso} = 0, 0, 0, 0 kHz). The exact MAS frequencies used were 8.0808, 11.1111, 13.1313, 16.6666 and 20.0000 kHz for SW$_f^{lin}$-TPPM simulations, while for SPINAL-64 and SW$_f^{lin}$-SPINAL those were 8.3333, 11.4583, 13.5415, 16.6666 and 20.8333 kHz , to avoid interference effects of τ_c and τ_r. 75

5.7 Spectral comparison of the ^{13}C resonances of the compound NBFS-K obtained by decoupling the ^{19}F abundant spins at ν_r = 10 kHz and $\nu_1 = 80$ kHz, with (a) SW$_f$-for-TPPM and (b) SW$_f$-rev-TPPM methods. 77

5.8 Offset dependence of the β (left) and γ(right) - ^{13}C resonances NBFS-K for forward (filled triangles) and reverse sweeps (hollow triangles) on SW$_f$-TPPM. The offset on the protons was varied in the range of ±10 kHz. The MAS frequency was kept at 10 kHz and the decoupling RF amplitude employed was 80 kHz. 78

6.1 A schematic representation of the effects introduced by the Zeeman ($\hat{\mathscr{H}}_Z$) and the first ($\hat{\mathscr{H}}_Q^I$) and second ($\hat{\mathscr{H}}_Q^{II}$) order quadrupolar interactions on the energy levels of a nucleus with spin $I = \frac{3}{2}$. . . 80

6.2 Simulated static first-order broadened powder line-shape of a nucleus with spin $I = \frac{5}{2}$, showing (left) central transition (CT) and satellite transitions (ST), and (right) a static powder line-shape of the CT alone. $C_Q = 1.6$ MHz, $\delta_{iso} = 0.00$ ppm and $\eta = 0.00$. . . . 81

6.3 Simulated static first-order broadened powder line-shape of a nucleus with spin $I = \frac{5}{2}$, showing (left) central transition (CT), and (right) a MAS powder line-shape of the CT. $C_Q = 1.6$ MHz, $\delta_{iso} = 0.00$ ppm and $\eta = 0.00$. 82

6.4 2D ^{45}Sc-3QMAS (left) and 5QMAS (right) spectra of scandium sulphate pentahydrate powder at $B_0 = 9.4$ T and 12 kHz MAS. The 5QMAS spectrum shows high-resolution in the indirect (F_1) dimension. 87

6.5 Diagrammatic representation of the 5QMAS split-t_1 pulse sequences with different 5Q coherence excitation and conversion parts. (a) Use of hard RF pulses, $P_H^{exc} - P_H^{con}$; (b) use of FAM-II coherence conversion, P_H^{exc}-FAM-II; (c) additional use of a FAM-I pulse train for improved 5Q excitation, [P_H^{exc}-FAM-I]–FAM-II. Below, the schematic coherence pathway of the 5QMAS experiment is given. The 5Q-filtered ^{45}Sc-NMR spectra of scandium sulphate pentahydrate (ScSPH) obtained with the pulse schemes (a)–(c) are shown on the right. 89

6.6 2D ^{45}Sc 5QMAS (left) spectrum of scandium sulphate pentahydrate powder at $B_0 = 9.4$ T and 12 kHz MAS and the F_2 traces and DMFIT [136] simulations (right) of the three ^{45}Sc crystallographic sites. 90
6.7 5Q-filtered ^{45}Sc NMR spectra (F_2 dimension) of ScSPH acquired (a) without ^{1}H decoupling and with (b) TPPM, (c) SPINAL-64, (d) SW_f^{tan}-TPPM and (e) SW_f^{lin}-TPPM ^{1}H decoupling methods at 12 kHz MAS. 93
6.8 The F_1 (isotropic) projections of ^{45}Sc 5QMAS spectra of ScSPH at 12 kHz MAS acquired (a) with SW_f^{lin}-TPPM ^{1}H decoupling and (b) without ^{1}H decoupling. 94
6.9 The ^{23}Na MAS NMR spectrum of cryolite (a) without and (b) with ^{19}F decoupling at 9.4 T magnetic field and 12 kHz MAS frequency. The decoupling method employed was SW_f-SPINAL. 96
6.10 The ^{23}Na 3QMAS NMR spectrum of cryolite with ^{19}F decoupling at 9.4 T magnetic fieeld and 10 kHz MAS frequency. The decoupling method employed was SW_f-TPPM. 97
6.11 Comparison of ^{19}F decoupling efficiency of TPPM using the indicated phase angles ϕ at 10 kHz MAS frequency. (a) ^{23}Na 3Q-filtered spectra (F_2 traces), using a 3Q evolution time of $t_1 = 10\mu$s, with 2400 transients acquired. (b) ^{23}Na isotropic (F_1) projections of full 3QMAS spectra (360×128 transients acquired). 98
6.12 Comparison of ^{23}Na 3QMAS isotropic (F_1) projections of cryolite with (a) TPPM, (b) SPINAL-64, (c) SW_f-TPPM, (d) SW_f(32)-SPINAL-32 methods at MAS frequency of 10 kHz in a 9.4 T magnetic field. 99

1 (Appendix): Schematic representation of the energy levels of two dipolar coupled spins $I = \frac{3}{2}$ and $I = \frac{1}{2}$, showing the modification of the energy levels by the dipolar interaction (only the branch with $m_S = -\frac{1}{2}$). The triple-quantum transition is affected three times as much as the single-quantum transition by the secular dipole–dipole coupling d_{IS}. For clarity, effect of the quadrupolar interaction is omitted in this graphics. 106

Chapter 1

Introduction

Nuclear Magnetic Resonance (NMR) [1, 2] is one of the most useful spectroscopic techniques to explore chemical, physical and biological properties of matter. This is realized by providing detailed information on local environments of liquid, solid and gaseous material phases. For this, NMR looks into the quantum world of very tiny magnetic moments of atomic nuclei in molecules, by making use of the very special quantum mechanical property called *spin*. *Spin* is a form of intrinsic angular momentum of a fundamental particle. NMR spectroscopy, in general, is all about inducing transitions between the nuclear spin energy levels, which are split with the help of a homogeneous external magnetic field. Radio-frequency waves are used to induce such a transition and hence to be in *resonance* [3–5].

Soon after the realization of electronic influence in such a spectrum, these fine-structured sharp peaks led to a revolution in NMR applications for the assignment of molecular structure, dynamics and spatial orientation. Also, different NMR responses of different phases of matter gained large scientific attention. NMR behaviour of systems with both mobile and rigid molecular species also provoked thoughts. But every such challenge, later led to new innovative experiments to manipulate spin dynamics for high resolution in NMR. Thus, the design of any NMR experiment does largely depend on the physical state of the material under study.

The very first NMR experiments were done by Purcell, Torrey and Pound (in solid paraffin) [1] and Bloch, Hansen and Packard (in liquid water) [2] independently in 1945. In a sample in liquid state one can observe very narrow resonance lines. But considerably large line-broadening occurs in NMR signals from a solid sample, which makes it difficult to interpret. Nevertheless, now-a-days there are many high-resolution methods available for NMR in solid-state [6–8]. The intention of this thesis is also the introduction of such a method. After having presented the basic principles of NMR spectroscopy, this thesis describes the design and applications of such methods for heteronuclear decoupling with frequency-swept multipulse sequences in solid-state NMR.

1.1 NMR Phenomena: Basic Principles

All the three main subatomic particles, electrons, protons and neutrons possess the intrinsic property of *spin*. Therefore, atomic nuclei also have *spin*. The net spin angular momentum of a nucleus, thus, has sub-atomic contributions from neutrons and protons. The magnitude of nuclear spin angular momentum is equal to $\hbar[I(I+1)]^{1/2}$ for all values of nuclear spin number I. The spin number has very high influence in the NMR characteristics of the nucleus. The basic criteria for a nucleus to be NMR-active is to have a non-zero spin number (or a net magnetic moment). Hence, even-though highly abundant in nature, ^{12}C, ^{16}O, ^{28}Si, ^{40}Ca (I=0) etc., are NMR inactive. The NMR active nuclei are further classified into half-integer spin nuclei (like ^{1}H (I=1/2), ^{7}Li (I=3/2), ^{17}O (I=5/2), ^{45}Sc (I=7/2), ^{93}Nb (I=9/2) etc.,) and integer spin nuclei (like ^{2}H (I=1), ^{10}B (I=3), ^{40}K (I=4), ^{138}La (I=5), ^{50}V (I=6), ^{176}Lu (I=7) etc.). Since nuclei with $I = 1/2$ and $I > 1/2$ behave magnetically different, they are classified separately.

For a nucleus with spin number I, there are $(2I+1)$ possible energy levels, corresponding to each different magnetic quantum number m_I; (where $m_I = -I, -I+1, ..., I-1, I$). Therefore, for a nucleus with spin I=1/2, there are two such degenerate energy states. But as soon as a static magnetic field is applied to such a system, these energy levels become non-degenerate. This splitting of energy levels (otherwise degenerate) in the presence of a magnetic field is called *Zeeman* interaction [9]. Energy for a given spin state m_I, in presence of a magnetic field (B_0) can be expressed as,

$$E_{m_I} = -m_I\gamma\hbar\vec{B}_0 \tag{1.1}$$

Here γ is the gyro-magnetic ratio (expressed in $rad.s^{-1}.T^{-1}$), which is unique for each nucleus. For example, γ of ^{1}H nucleus is 26.7513×10^7 rad . s^{-1} . T^{-1} (or 42.576 MHz . T^{-1}) and that of ^{19}F nucleus is 25.1662×10^7 rad . s^{-1} . T^{-1} (or 40.053 MHz . T^{-1}) [10].

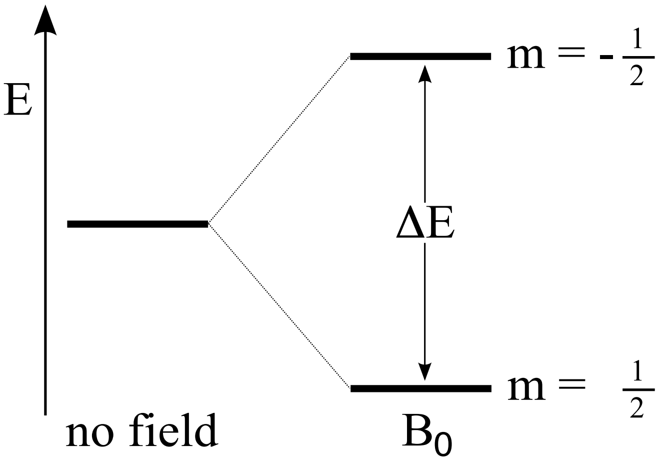

Figure 1.1: A schematic representation of Zeeman interaction for a nuclear spin with $I = \frac{1}{2}$.

It requires another oscillating magnetic field perpendicular to the static magnetic field to induce transitions between already split energy levels. This is carried out by applying electromagnetic radiation (radio-frequency for NMR) with suitable energy $h\nu_0$, and hence satisfying the *resonance* condition.

$$\Delta E = h\nu_0 = \gamma\hbar\vec{B}_0 \tag{1.2}$$

Therefore,

$$\nu_0 = \frac{\gamma\vec{B}_0}{2\pi} \tag{1.3}$$

This resonance frequency is known as Larmor frequency.

The population difference between the high and low nuclear spin energy levels given by Boltzmann distribution depends heavily upon the magnetic field $\vec{B}_0$ and temperature. The relation is,

$$\frac{N_a}{N_b} = exp\left(\frac{\gamma\hbar\vec{B}_0}{kT}\right) \tag{1.4}$$

Here k is the Boltzmann constant. Since the population difference is directly proportional to the intensity of NMR signal, for intense resonances, a large magnetic field and/or low temperatures are preferred.

To describe the NMR principles, at least partially, one may find the precession model quite useful. Nuclear magnetic moments, when placed in an external magnetic field (let's say, along the z-axis), can align either along or against the direction of the applied field and start to precess in Larmor frequency. But precession is not *visible*, until the observer uses a resonant radio-frequency (RF) wave to flip the magnetization from the z-axis to a transverse plane with the detector. The picture of nuclear precession is easy to understand in the case individual nuclear magnetic moments. But for an ensemble of magnetic moments, one prefers to use macroscopic net magnetization vector model or simply vector model (Fig. 1.2). The vector model is very useful model to understand simple NMR experiments.

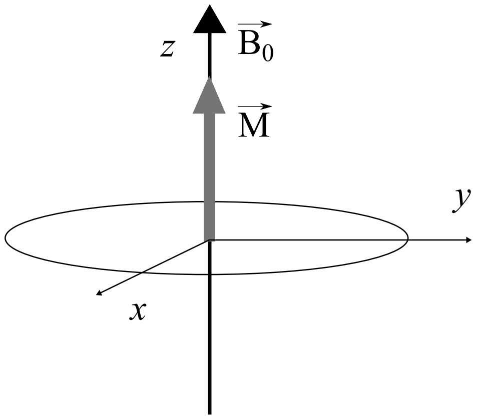

Figure 1.2: The net magnetization vector $\vec{M}$ aligned along $\vec{B}_0$ in the static frame.

One of the most important inventions in NMR spectroscopy is the introduction of RF pulses followed by Fourier transformation (FT) technique. Before that one needed a sweep of either magnetic field or radio-frequency to find out the resonance absorption (In terms of practicality, magnetic field sweeps were indeed preferred). But this method suffered from poor sensitivity and long measurement times. With the help of a *RF* pulse, a large range of frequencies can be excited for a quantitative detection of several resonances simultaneously. To understand the mechanism a Fourier analysis of the pulse should be done. For example, for a rectangular pulse the Fourier space expression is a Cardinal Sine (or *sinc*) function.

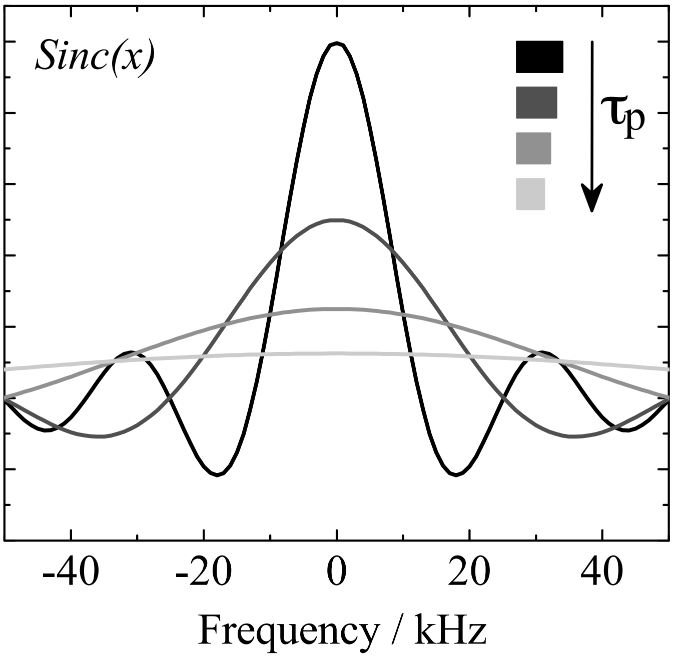

Figure 1.3: The Fourier analysis of *RF* pulses with different pulse durations (τ_p).

As shown in the Fig. 1.3, the shorter the pulse becomes, the flatter is the corresponding *sinc* function. This means, quantitative excitation and thereby detection of a large spread of frequencies can be done with very short pulses. Generally, for standard NMR experiments, *RF* pulses, which exist for a few μs duration are used.

Now to understand a simple NMR experiment using *RF* pulses, a bulk magnetization vector ($\vec{M}$) is introduced. $\vec{M}$ is the sum of individual nuclear magnetizations and it aligns along the applied magnetic field $\vec{B}_0$ (parallel to z-axis, as shown in the Figure 1.4). When perturbed by an another magnetic field (here, RF pulse), $\vec{M}$ precesses about $\vec{B}_0$. The second applied magnetic field ($\vec{B}_1$) should oscillate with an angular velocity of ω_0 which is equal to $\gamma\vec{B}_0$, to have a constant hold on $\vec{M}$.

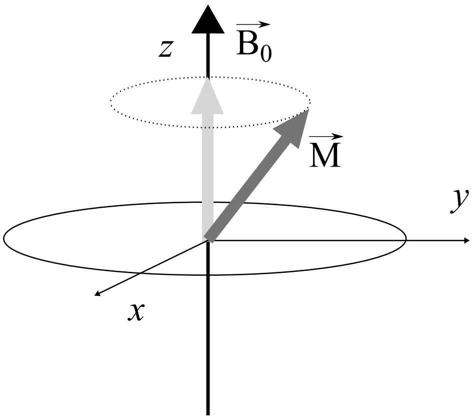

Figure 1.4: The net magnetization vector $\vec{M}$ precesses about $\vec{B}_0$ in the static frame.

In addition to the vector picture of the bulk magnetization, one should have a rotating frame of reference to visualize the motion of $\vec{M}$. If the coordinate frame rotates in a frequency equal to the Larmor frequency of the nucleus, the vector $\vec{M}$ is static , and can now be used to demonstrate experiment mechanisms. In the frame of the Laboratory, $\vec{M}$ rotates about $\vec{B}_0$, and when $\vec{B}_1$ is applied it rotates about both $\vec{B}_0$ and $\vec{B}_1$. But in the rotating frame, $\vec{M}$ rotates only about $\vec{B}_1$. By convention, z'-axis defines $\vec{B}_0$ and x'-axis defines $\vec{B}_1$ in the rotating frame. By the application of the RF pulse, $\vec{B}_1$ tries to rotate $\vec{M}$ away from the static magnetic field $\vec{B}_0$ (from the z'-axis) to the transverse ($x'y'$) plane as shown in the Figure 1.5. The projection of this vector to the $x'y'$-plane gives the intensity of the NMR signal.

The laws of motion of the magnetization vector $\vec{M}$ components were derived by Felix Bloch, and these very basic principles of NMR are called Bloch equations [11]. In the laboratory frame of resonance, the Bloch equations for the three

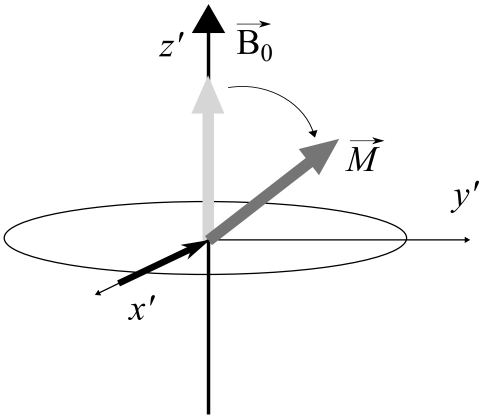

Figure 1.5: The effect of RF pulse on the net magnetization vector $\vec{M}$ in the rotating frame.

components $\vec{M}_x$, $\vec{M}_y$ and $\vec{M}_z$ on free precession are:

$$\frac{dM_x}{dt} = \gamma(M_y B_0) - \frac{M_x}{T_2} \tag{1.5}$$

$$\frac{dM_y}{dt} = -\gamma(M_x B_0) - \frac{M_y}{T_2} \tag{1.6}$$

$$\frac{dM_z}{dt} = -\frac{M_z - M_0}{T_1} \tag{1.7}$$

Here M_0 is the steady state equilibrium magnetization, and T_1 and T_2 are the characteristic relaxation time constants.

The T_1-relaxation or the spin-lattice relaxation involves the loss of energy to the surroundings from the high energy spins after being irradiated by the RF pulse. It is the mechanism to restore the longitudinal magnetization (along z'-axis) and hence to be in thermal equilibrium. So, for a multi-scan experiment, one has to wait more than T_1, between scans, to attain thermal equilibrium. The equation governing the behavior of exponential return of the longitudinal magnetization ($\vec{M}_z$), as a function of the time t after its displacement is:

$$\vec{M}_{z'} = \vec{M}_0(1 - e^{\frac{-t}{T_1}}) \tag{1.8}$$

T_2-relaxation or the spin-spin relaxation describes the loss of the transverse (in $x'y'$-plane) component of the magnetization. It involves no loss of energy to the surroundings, but energy exchange among spins.

$$\vec{M_{x'y'}} = \vec{M_{x'y'0}}(e^{\frac{-t}{T_2}}) \tag{1.9}$$

Every relaxation mechanism is triggered by a fluctuating local field or tumbling motions of magnetic moments. Therefore, molecular dynamics play an important role in NMR relaxation mechanisms. Long T_2-relaxation times yield sharp and intense resonances, and on the other hand fast T_2-relaxation results in broad resonances. This is observed in the time-domain data as two extreme cases of exponential modification on the sinusoidal frequency component. A monochromatic sinusoidal function, on FT, yields a single line on the frequency-domain, positioned exactly at the frequency of the wave. But if such a function is modified by an exponentially decaying function with the T_2-relaxation (or decay) time, one obtains a Lorentzian function in frequency domain (Fig. 1.6) on FT. The full width at half-height of this function is then equal to $(1/\pi T_2)$ Hz.

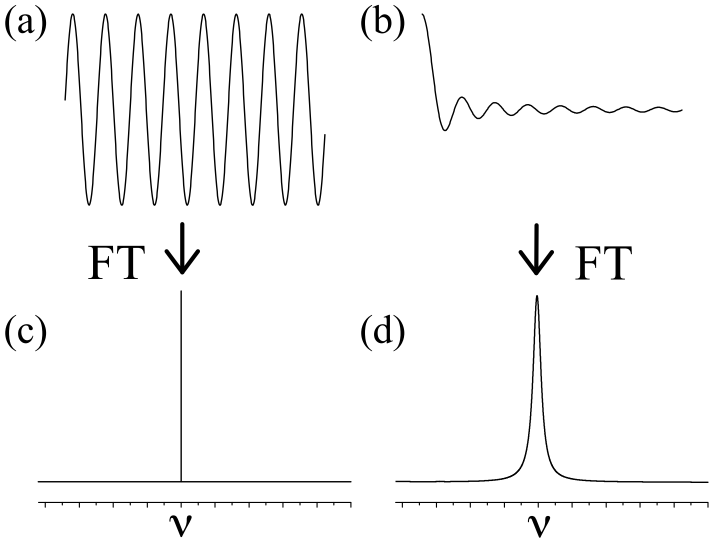

Figure 1.6: The Fourier transform of (a) *sine* function is (c) a single frequency line, while for an (b) exponentially modified *sine* function the FT is (d) a Lorentzian.

The exponentially decaying time domain NMR signal is called a Free Induction Decay (FID). This is detected by the detector coil as a weak induced voltage and is later amplified, digitized and stored. Fourier transformation is later done as a processing step to identify the frequency components with Lorentzian line shapes. Both the time-domain signal and the frequency-domain spectrum are complex functions.

It is important to understand the strength of the *RF* field used for NMR experiments. This is done in following way. The pulse which is able to flip the net magnetization vector $\vec{M}$ from the z'-axis to the $x'y'$-plane is called a 90° pulse, as shown in the Figure 1.7. Similarly, a 180° pulse is one which can invert $\vec{M}$ from the z'-axis to $-z'$-axis. Since the 90° pulse flips the magnetization to the transverse plane, the NMR signal (which is the projection of $\vec{M}$ to $x'y'$-plane) has maximum intensity. But signal intensity is zero with a 180° pulse. If one increments the pulse durations in very small steps from a very low value, and then observes the signals in an array, a sinusoidal dependence of the intensities to the pulse durations is seen (Figure 1.8). This oscillation depends on the nutation frequency, and it refers to the strength of the *RF* field used. The nutation frequency (usually expressed in kHz) is the inverse of a 360° pulse duration. Therefore, a short 360° pulse corresponds to a strong *RF* field.

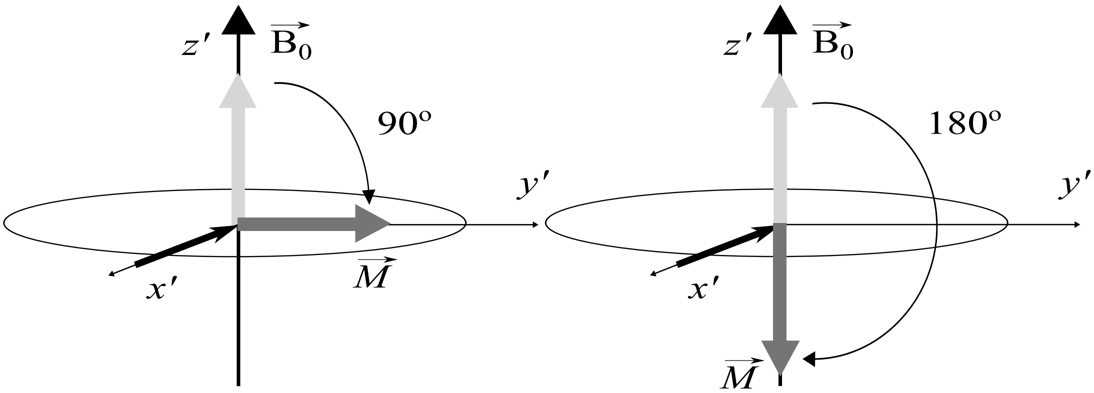

Figure 1.7: The effect of 90° and 180° *RF* pulses on the net magnetization vector $\vec{M}$ in the rotating frame.

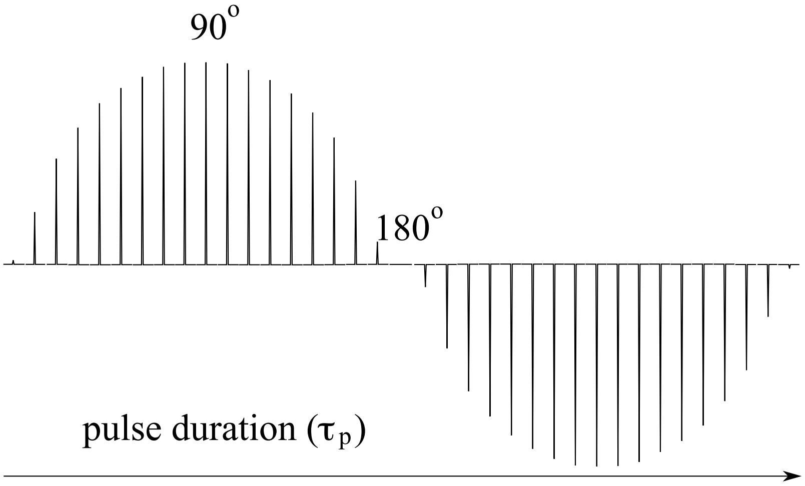

Figure 1.8: The sinusoidal dependence of the signal intensity with pulse duration.

1.2 NMR Interactions

NMR interactions may be classified into external and internal spin interactions. The interactions which are instrumental, constitute external interactions, whereas those from the sample itself are in the latter case. External spin interactions are mostly magnetic in nature. But the internal interactions depend on the physical state and electric and magnetic properties of the material analyzed. All these interactions are usually represented by nuclear spin Hamiltonians ($\hat{\mathscr{H}}$). The external interaction Hamiltonian ($\hat{\mathscr{H}}_{Ext}$) can be expressed as,

$$\hat{\mathscr{H}}_{Ext} = \hat{\mathscr{H}}_Z + \hat{\mathscr{H}}_{RF} \tag{1.10}$$

Here $\hat{\mathscr{H}}_Z$ is the *Zeeman* interaction, which is related to the applied static magnetic field $\vec{B}_0$. The magnitude of this interaction is usually in the range of $\sim 10^{6-9}$ Hz. $\hat{\mathscr{H}}_{RF}$ is the RF interaction from the applied oscillating magnetic field with a magnitude of hundreds of kHz ($\sim 10^5$ Hz).

The internal Hamiltonian $\hat{\mathscr{H}}_{Int}$ is the sum of many contributions,

$$\hat{\mathscr{H}}_{Int} = \hat{\mathscr{H}}_{CS} + \hat{\mathscr{H}}_{DD} + \hat{\mathscr{H}}_J + \hat{\mathscr{H}}_Q + ... \tag{1.11}$$

Here $\hat{\mathscr{H}}_{CS}$ is the chemical shift interaction, which is due to the electronically induced magnetic fields spanning tens of kHz ($\sim 10^4$ Hz). $\hat{\mathscr{H}}_{DD}$ is the direct through-space interaction between nuclear dipole moments and is of the order of $\sim 10^5$ Hz. $\hat{\mathscr{H}}_J$ is usually called the J-coupling or indirect spin-spin coupling. It is scalar bond-mediated interaction of nuclear magnetic moments. They range from a few Hz to hundreds of Hz usually. The biggest internal spin interaction $\hat{\mathscr{H}}_Q$ is the quadrupolar interaction of the nuclei with spin $I > 1/2$ with the electric field gradients in the vicinity of the nucleus. It has magnitudes ranging from a few hundreds of kHz to tens of MHz ($\sim 10^{5-7}$ Hz). Other internal interactions include Knight shift and hyperfine interactions, which are special cases of nuclear-electron interactions.

Generally, a *high-field* approximation to spin interactions is assumed for theoretical evaluations. In other words, all other spin interactions are considered to be perturbations to the *Zeeman* Hamiltonian. Therefore, these interactions modify the *Zeeman* energy levels and hence the frequency of transitions. This makes NMR heavily dependent on the local structural and chemical environments of the probing nucleus. In the following sections, the *Zeeman*, *RF*, chemical shift, scalar and dipolar interactions are discussed in detail. The quadrupolar interaction is discussed in the beginning of Chapter 6.

1.2.1 The *Zeeman* interaction

The NMR super-conducting magnet provides a highly homogeneous strong static magnetic field, usually represented as $\vec{B}_0$, the strength of which is in the order of a few *Teslas*. In presence of such strong magnetic fields, the nuclear spin energy levels lose degeneracy and the spin Hamiltonian for this interaction is given as,

$$\hat{\mathscr{H}}_Z = -\gamma \vec{B}_0 \hat{I}_z \tag{1.12}$$

$\hat{I}_z$ is the spin operator for the spin I along the direction of the static magnetic field $\vec{B}_0$, with a Larmor frequency of $-\gamma\vec{B}_0$. This interaction is the nuclear *Zeeman* interaction (Fig. 1.1), and all internal spin interactions modify the *Zeeman* energy levels.

1.2.2 The Radio-frequency field

This is the oscillating magnetic field applied perpendicular to the static magnetic field to induce transitions between the *Zeeman* energy levels. A radio-frequency (RF) field is used to force such a transition. The RF interaction Hamiltonian, in general, is given as,

$$\hat{\mathscr{H}}_{RF} = \vec{B}_1 sin(\omega t + \phi) \tag{1.13}$$

Here ϕ is called the phase angle of the RF pulse and it denotes the phase shift of the short-lived RF wave from the origin. $\vec{B}_1$ is the maximum RF amplitude during the pulse. This is very often represented in frequency units (ω_1).

$$\omega_1 = \frac{1}{2}\gamma\vec{B}_1 \tag{1.14}$$

The nutation on nuclear precession induced by RF field has an important role here. The nutation frequency ω_{nut} is equal to ω_1 only at an *on-resonance* condition. Within the NMR community, the strength of the RF field is represented by ν_{nut} in the units of Hz (i. e., $\omega_{nut}/2\pi$). For most of the NMR experimental purposes, ν_{nut} is in the range of 1-200 kHz.

The RF interaction provides a variety of tools to handle all internal spin interactions by different spin-space manipulations. Recently developed sophisticated NMR experiments can reduce, average, and re-introduce many of internal spin interactions to yield information about structure, chemical environment, physical state, dynamics etc., of the materials under study.

1.2.3 The chemical shift

The chemical shift interaction is introduced by the electronic presence in the vicinity of a nucleus [12, 13]. The interaction shifts the *Zeeman* energy levels, so that the frequency of transition between the levels also gets shifted. This shift can either add to or subtract from the original frequency. The reason of this is the electronic shielding of the nucleus from the external static magnetic field. Therefore, the chemical shift is very sensitive to number of electrons in the system, number and types of chemical bonds, electronegativity of the substituents etc. This interaction also has a linear dependence to the external field $\vec{B}_0$, like the *Zeeman* interaction. In the laboratory frame, the interaction Hamiltonian is,

$$\mathscr{H}_{CS} = \sum_i \gamma^i \hat{I}_z^i . \sigma^i . \vec{B}_0 \tag{1.15}$$

Here σ is the chemical shielding. It is represented as a tensor because the magnitude of chemical shielding depends on the orientation of the molecule with respect to $\vec{B}_0$. But this tensor shows orientation dependence of the interaction in Cartesian coordinates with respect to the molecule. Diagonalization of this tensor results in another tensor with three principal elements. Thus the interaction can be described in its own principal axis system (PAS). The PAS and the laboratory frame are thus different expressions for convenience.

A suitable transformation from PAS to LAB frame retains the magnitude of σ_{zz}:

$$\sigma_{zz} = \sigma_{iso} + \frac{1}{2}\Delta\sigma[(3cos^2\theta - 1) - \eta(sin^2\theta cos2\phi)] \tag{1.16}$$

Here σ_{iso} is the average of all three principal elements, and it is termed as the isotropic chemical shielding. θ (inclination angle) and ϕ (azimuthal angle) are the polar angles, expressing the orientation of the PAS in the LAB frame.

$$\sigma_{iso} = \frac{1}{3}(\sigma_{xx} + \sigma_{yy} + \sigma_{zz}) \tag{1.17}$$

$\Delta\sigma$ is termed as shielding anisotropy,

$$\Delta\sigma = \sigma_{zz} - \sigma_{iso} \tag{1.18}$$

and η represents the asymmetry parameter,

$$\eta = \frac{\sigma_{yy} - \sigma_{xx}}{\sigma_{zz} - \sigma_{iso}} \tag{1.19}$$

The convention for assigning values to the principal components follows the order: $|\sigma_{zz} - \sigma_{iso}| \geqslant |\sigma_{yy} - \sigma_{iso}| \geqslant |\sigma_{xx} - \sigma_{iso}|$.

Chemical shielding (σ) represents the difference of the resonance frequency from the Larmor frequency ω_0 of the naked nucleus. While a well-shielded nucleus shows lower resonance frequency than the Larmor frequency, a de-shielded nucleus resonates at higher frequency. *Chemical shift* (δ) represents the difference in resonance positions of an *observed* sample (ν_{obs})and a *reference* sample (ν_{ref}). Both chemical shielding and chemical shift are normalized and expressed in parts per million (ppm) units. Chemical shift, in units of Hz, varies with the strength of the static magnetic field, but in ppm unit it stays the same in different fields. This makes it one of the most useful conventions in NMR to have definite δ ppm values for chemical entities universally. The chemical shift in ppm is expressed as,

$$\delta_{obs} = \frac{\nu_{obs} - \nu_{ref}}{\nu_{ref}} \times 10^6 \tag{1.20}$$

To express chemical shift tensor components ($\delta_{11}, \delta_{22}, \delta_{33}$) in terms of the magnitude of the interaction, one can again define certain parameters for isotropic chemical shift δ_{iso}, anisotropy $\Delta\delta$ and asymmetry η_{CS}. They are then used to describe the NMR line shapes, like in the Figure 1.9. The anisotropy parameter $\Delta\delta$ gauges the width of CSA and the asymmetry parameter (η_{CS}) describes the deviation from an axially symmetric case. The relations between the diagonal elements of chemical shift tensor and the chemical shift parameters are:

$$\delta_{iso} = \frac{1}{3}(\delta_{11} + \delta_{22} + \delta_{33}) \tag{1.21}$$

$$\Delta\delta = \delta_{33} - \delta_{iso} \tag{1.22}$$

$$\eta_{CS} = \frac{\delta_{22} - \delta_{11}}{\delta_{33} - \delta_{iso}} \tag{1.23}$$

Here, the magnitudes of the diagonal elements are assigned as follows: $|\delta_{33} - \delta_{iso}| \geqslant |\delta_{22} - \delta_{iso}| \geqslant |\delta_{11} - \delta_{iso}|$, according to IUPAC rules.

Different molecular orientations, in NMR, can cause different electronic shieldings to the observed nuclei. Therefore, a single crystal shows single sharp resonance positioned according to the orientation of the crystal. But it is different in the case of a polycrystalline powder sample. *Chemical shift anisotropy* scales linearly with the static magnetic field $\vec{B}_0$. It creates an envelope of different chemical shift contributions from differently oriented crystallites (Figure 1.9) in a polycrystalline (powder) sample. The characteristic shape is known as a ”Pake” pattern [14]. The asymmetry parameter η_{CS} has an influence on the shape of the

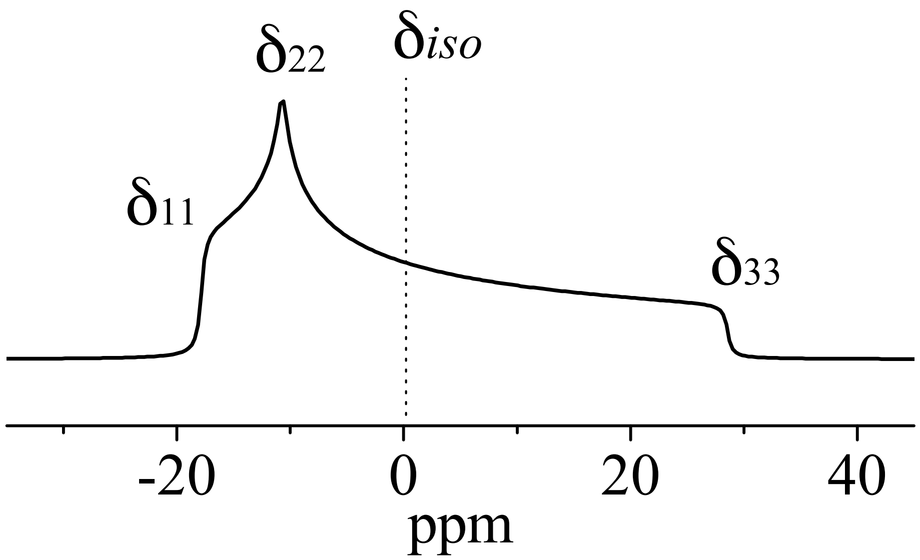

Figure 1.9: A schematic chemical shift anisotropy (CSA) pattern of a spin $I = \frac{1}{2}$ system with $\eta_{CS} = 0.25$.

pattern. A rapidly moving molecular system feels only a time-average of the CSA interaction. This is called *motional averaging*, and this is indeed the case with fast moving gases and liquids. This helps the resonances for different molecular orientations to fall in the average value (δ_{iso}) position, and thus to have very narrow NMR signals. The time-scale of the motion (or the material phase) is one of the factors which influences the motionally averaged interaction Hamiltonian. Therefore, CSA contributes heavily to the large line-widths of NMR signals of rigid solids.

1.2.4 The direct dipole-dipole interaction

The interaction of two magnetic dipoles through-space is called direct dipole-dipole interaction. Therefore, the nuclear spins with magnetic moments also undergo dipolar coupling. The magnitude of this interaction is directly proportional to the product of the coupling magnetic moments and inversely proportional to the cube of the distance between them.

If μ_1 and μ_2 are the magnetic moments of the spins which are coupling in a

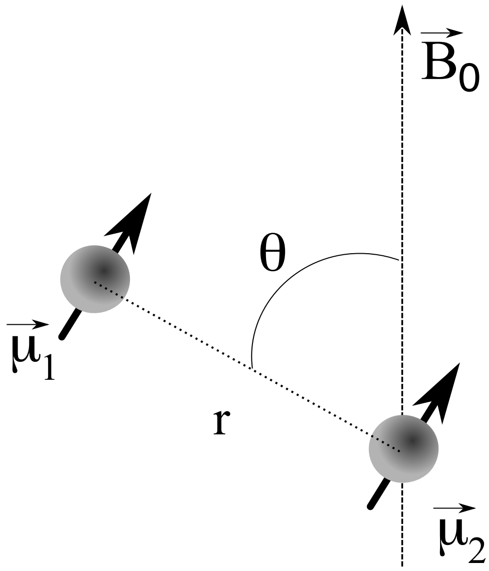

Figure 1.10: A diagrammatic representation of dipole-dipole interaction.

static magnetic field of $\vec{B}_0$, then the dipolar interaction Hamiltonian, $\hat{\mathscr{H}}_{DD}$ scales with $\vec{\mu}_1\vec{\mu}_2/r^3$. The interaction is also dependent on the angle (θ) between the vectors $\vec{B}_0$ and $\vec{r}$ (Fig. 1.10). If one replaces the magnetic moment vector μ by operators $\hbar\gamma\hat{I}$, the full dipolar coupling Hamiltonian is expressed as,

$$\hat{\mathscr{H}}_{DD} = -\frac{\mu_0\gamma^j\gamma^k}{4\pi}\hbar\,(A+B+C+D+E+F) \tag{1.24}$$

Here A, B, C, D, E, and F are called the dipolar alphabet and they are represented by the following relations:

$$A = -\hat{I}_z^j\hat{I}_z^k\,(3cos^2\theta - 1) \tag{1.25}$$

$$B = \frac{1}{4}\,(\hat{I}_+^j\hat{I}_-^k + \hat{I}_-^k\hat{I}_+^j)\,(3cos^2\theta - 1) \tag{1.26}$$

$$C = -\frac{3}{2}\,(\hat{I}_+^j\hat{I}_z^k + \hat{I}_z^k\hat{I}_+^j)\,sin\theta cos\theta e^{-i\phi} \tag{1.27}$$

$$D = -\frac{3}{2}\,(\hat{I}_-^j\hat{I}_z^k + \hat{I}_z^k\hat{I}_-^j)\,sin\theta cos\theta e^{+i\phi} \tag{1.28}$$

$$E = -\frac{3}{4}\ \hat{I}_{+}^{j}\hat{I}_{+}^{k}\ sin^2\theta e^{-2i\phi} \tag{1.29}$$

$$F = -\frac{3}{4}\ \hat{I}_{-}^{j}\hat{I}_{-}^{k}\ sin^2\theta e^{+2i\phi} \tag{1.30}$$

Here, $\hat{I}_{\pm}$ represents the spin *ladder operators.* For the *heteronuclear* dipolar Hamiltonian, $\hat{\mathscr{H}}_{DD}^{IS}$, only the term A makes a *secular* contribution. The *non-secular* terms do not commute with the *Zeeman* Hamiltonian. But for $\hat{\mathscr{H}}_{DD}^{II}$, i.e., the *homonuclear* case, both the terms A and B contribute. The first part in term B is otherwise called the "flip-flop" term and it contributes to spin polarization exchange mechanism. In the homonuclear case of two I spins (e.g. ^{1}H-^{1}H), the interaction is given as,

$$\hat{\mathscr{H}}_{DD}^{II} = -\frac{\mu_0}{4\pi}\hbar\sum_{j}\sum_{j<k}\frac{(\gamma^I\gamma^I)}{r_{jk}^3}\frac{1}{2}(3cos^2\theta_{jk} - 1)(3\hat{I}_z^j\hat{I}_z^k - \hat{I}^j.\hat{I}^k) \tag{1.31}$$

But for a heteronuclear coupling case of I and S spins (e.g. ^{1}H-^{13}C),

$$\hat{\mathscr{H}}_{DD}^{IS} = -\frac{\mu_0}{4\pi}\hbar\sum_{j}\sum_{j<k}\frac{(\gamma^I\gamma^S)}{r_{jk}^3}\frac{1}{2}(3cos^2\theta_{jk} - 1)(2\hat{I}_z^j\hat{I}_z^k) \tag{1.32}$$

Here a quantity, heteronuclear dipolar coupling constant (d_{IS}) is defined as,

$$d_{IS} = \frac{\mu_0}{4\pi}\frac{\gamma^I\gamma^S}{r_{IS}^3}\hbar \tag{1.33}$$

Here μ_0 is the vacuum permeability. Having very large gyro-magnetic ratios, ^{1}H and ^{19}F exhibit very large dipolar couplings. Usually dipolar coupling is expressed in the units of kHz.

The dipolar interactions can be represented in spherical tensor notation, and the trace of the dipolar tensor is zero. This means that, in an isotropic liquid, the dipolar interaction is time-averaged to zero. But in the case of solids, it remains as another source of line-broadening. For an isolated spin pair in a single crystal, the dipolar interaction induces two transitions for one orientation to the external magnetic field. But for a powder with crystallites oriented in all possible directions, one can observe an envelope of all the contributions. This generates

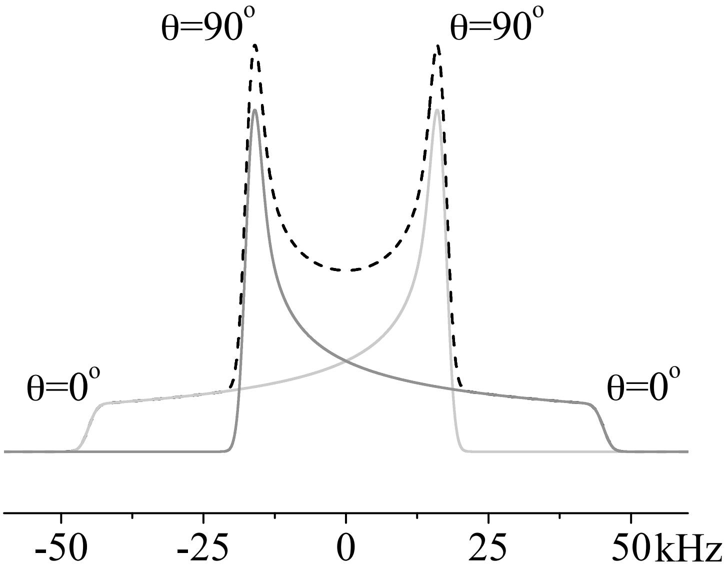

Figure 1.11: A dipole ”Pake doublet”, which is composed of two sub-spectra resulting from the two spin states of the coupled nuclei.

the characteristic ”Pake doublet” pattern [14], as shown in the Figure 1.11. If we go from the case of a isolated spin pairs (as described above) to the case of many spins interacting which each other, lots of Pake patterns overlap in an ill-defined fashion, leading to a broad line shape that cannot be quantitatively interpreted. There are many NMR methods now-a-days (a) to average out dipolar couplings for better resolution (see Chapter 2) and (b) to reintroduce (recouple) them after their partial averaging due to MAS. The recoupling of dipolar interaction is useful in structural studies of chemical compounds, because it is scaled by the distance between interacting nuclei. For a single spin pair, calculation of the dipolar coupling d_{IS} is a straightforward process from the ”Pake” pattern. But for a non-isolated spin pair in single crystals or powder samples, the observation of d_{IS} with high-resolution requires advanced recoupling techniques like Rotational-Echo DOuble-Resonance (REDOR) [15, 16]. Efficient decoupling of the abundant spin (e.g. ^{1}H) is also needed to see the interaction of the chosen spin pair (e.g. ^{13}C-^{15}N). In liquids, due to rapid molecular motions, the dipolar interaction is averaged. But in solutions of molecules with very high molecular weights, anisotropic liquids and in solids, they do not vanish completely. If the dipolar information is provided, the internuclear distance can be calculated from this equation. Another important application of dipolar interaction is that it is used as a bridge to transfer polarization between nuclei.

1.2.5 The scalar spin-spin coupling

The scalar spin-spin-coupling (or J coupling) is the indirect (bond-mediated) coupling interaction between two spins. This also modifies the *Zeeman* energy levels, but usually to a very small extent. The J-interaction travels from nucleus-to nucleus through bonds with the help of *Fermi contact interaction* and electron-spin-pairing interaction (according to *Pauli's* principle). Since closely related to local electronic and nuclear environments, J-coupling interaction is a very useful tool for the determination of chemical structure. The J-coupling Hamiltonian is given as,

$$\hat{\mathscr{H}}_J = 2\pi \sum_{j<k}^{N} \hat{I}_z^j J_{jk} \hat{I}_z^k \tag{1.34}$$

Here J_{jk} is the scalar coupling tensor. But the isotropic part of J-coupling contains scalar coupling constant expressed in Hz. Unlike dipolar coupling or CSA, J-coupling always has a non-zero isotropic value in the case of bonded nuclear systems.

In NMR spectra J-coupling is observed as fine-splittings, the number and intensity ratios of which provides a very clear idea about the chemical neighborhood. The number of the J-splittings depends on the spin (I) of the nucleus involved in the coupling and the number of such neighboring nuclei (n). For any given nuclei, there are $2nI + 1$ J-splittings with a defined intensity distribution. Usually in liquid samples, the J coupling has magnitudes in the order of 1-100 Hz. But in the case of solids, the J-couplings are hidden by the prominent anisotropic interactions, like dipolar coupling. Therefore, usually in solid-state NMR J-couplings are not *visible*. But there are occasions, when the J-coupling constant has very high magnitudes, especially in cases, where heavy nuclei (like ^{93}Nb, ^{119}Sn, ^{207}Pb etc.) are involved [17, 18]. One of the main applications of J-coupling is that, the presence of it in NMR spectra confirms the covalency of chemical bonding in the system.

1.3 Resolution and Sensitivity in Solid-State

Solid-state NMR suffers severely from anisotropic broadening of NMR lines, arising from different above-mentioned internal interactions, when compared to solution-state NMR. Rapid motion of molecules in liquid (of the order of GHz) can average almost fully the anisotropic contributions to the line-width. Since molecules are either less mobile or immobile in solids, large line-broadening occurs. There are methods available now-a-days for line-narrowing in NMR. This can either be done mechanically or by manipulating spin states. In the following section, such two methods are discussed, which were extensively used for the research work presented in this thesis.

1.3.1 Magic-angle spinning

All the anisotropic NMR internal interactions have a strong dependence on the nuclear orientation with respect to the external magnetic field, $\vec{B}_0$. In single crystals, one can observe only a contribution from one orientation of the sample. But in a powder sample, with numerous crystallite orientations, a large overlap of contributions from all the orientations is observed. This line-broadening effect made the measurement of powder sample difficult in former times, until E. R. Andrew *et. al.* [19] introduced a method for mechanical averaging of anisotropic interactions. Most of orientation dependent NMR interactions have a common term in their interaction Hamiltonian, a Legendre polynomial of the order two with the orientation dependence, $3cos^2\theta - 1$. The interactions vanish, as this this term turns zero. This is possible when,

$$\theta = cos^{-1}\left(\sqrt{\frac{1}{3}}\right) = 54.74^\circ \tag{1.35}$$

This angle is called *magic angle*. For attaining this condition, the powder sample is filled in a cylindrical holder (known as rotor) and kept tilted 54.74° to the external magnetic field as shown in the Figure 1.12. But keeping the sample itself in the magic angle does not have an impact on anisotropic interactions. Mechanical mimicking of molecular motion also should be done by fast rotation of the

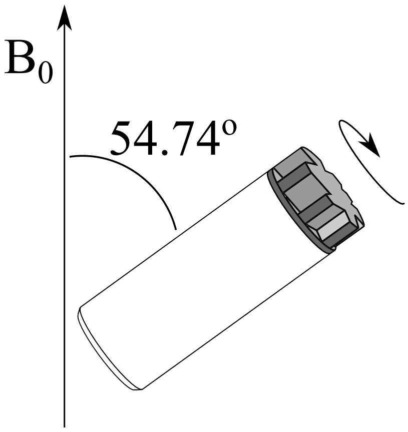

Figure 1.12: A schematic representation of Magic-Angle Spinning (MAS).

sample about this axis. This method is called *magic-angle spinning* (MAS) [19]. In a frequency-domain spectrum one can see only the isotropic spectrum while the anisotropic contributions are spun away. Therefore, a considerable line-width narrowing is achieved. The intensity which spread over the anisotropic contributions are then folded back to the averaged isotropic lines. An example of ^{13}C MAS NMR spectra as a function of spinning frequency is shown in the following Figure 1.13.

To average the anisotropic interactions effectively to zero, the MAS frequency (ω_r) must be much larger (about 5x) than the magnitude of the broadening interaction. If the MAS rate is smaller than the interaction, the spinning sideband (SSB) manifold is visible in the spectrum. Since the position of SSB's depends on ω_r, one can identify the isotropic chemical shift peaks by comparing spectra at different ω_r's. The isotropic peaks remains at the same position at any given spinning speed.

Although the application of MAS can average dipolar and CSA interactions, only a partial averaging of quadrupolar interaction (in the case of spin $I > \frac{1}{2}$ nuclei) is done. Only the interaction to the first-order can be averaged by MAS. The second-order quadrupolar interaction survives and this is a very large line-broadening interaction. This is later explained in Chapter 6. But there is one more second-order term which is not averaged completely by MAS alone. This is the second-order dipolar-CSA cross term [20, 21], which will be discussed in

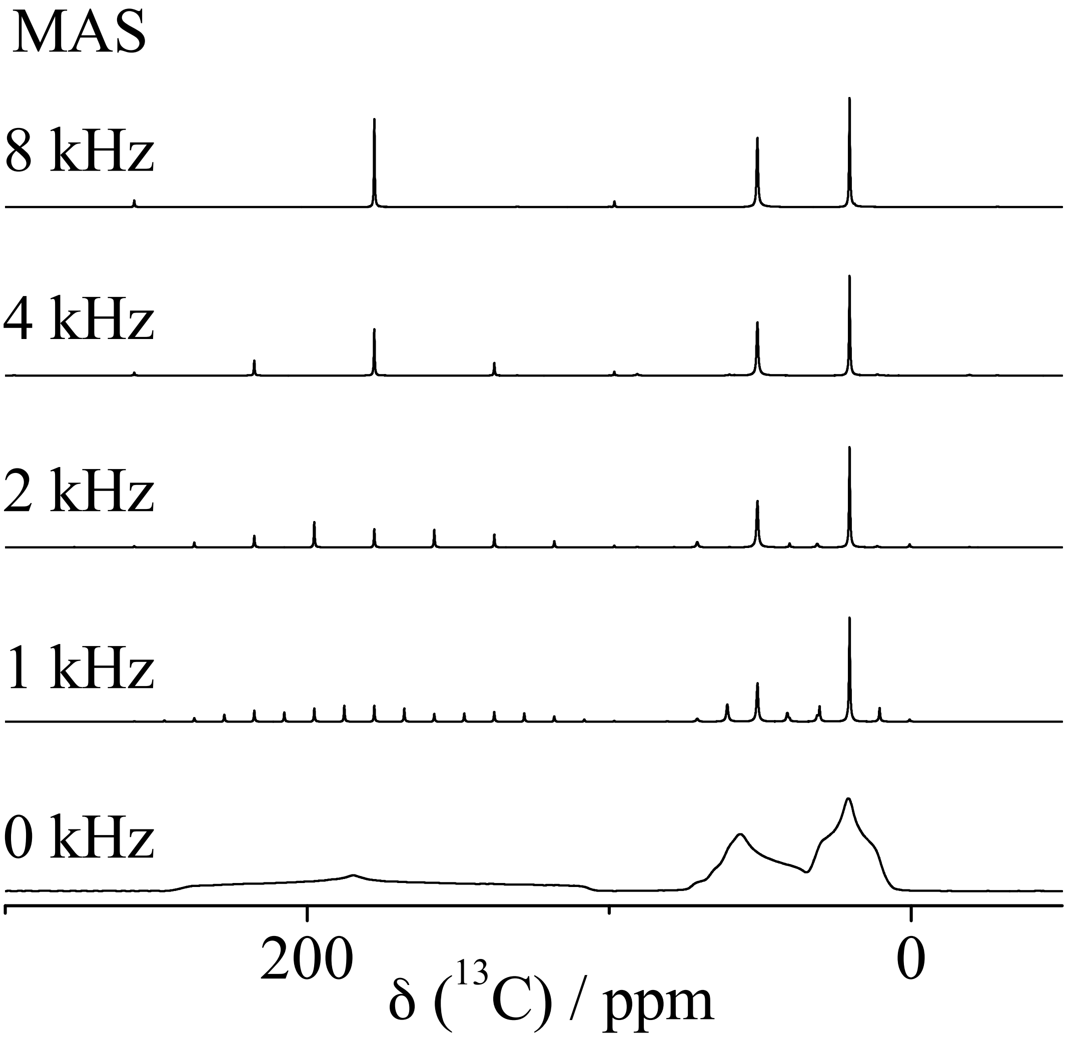

Figure 1.13: An experimental ^{13}C NMR spectrum of solid alanine showing the effect of magic-angle spinning (MAS) at a magnetic field of strength 9.4 T. The anisotropic chemical shielding and dipolar effects are getting averaged, as the MAS frequency increases, from a static case (bottom) to 8 kHz MAS (top). The mechanical averaging is reflected by the gradual disappearance of the spinning side-bands (SSB).

more detail in Section 2.4.2. In such cases, *spin decoupling* [22–25] along with MAS should be made use of, and will discussed in Chapter 2.

1.3.2 Cross-polarization

In this technique, polarization from abundant spins (such as ^{1}H or ^{19}F) is transferred to rare spins (like ^{13}C or ^{15}N) to enhance the sensitivity of the nucleus with low gyro-magnetic ratio. In this method, the field strengths in the rotating frame of the abundant (I) and rare (S) nuclei are set equal (Hartmann-Hahn condition) [26]. This makes the ground for polarization transfer through dipolar coupling and this NMR experiment is called *cross-polarization* (CP) [27, 28].

The Hartmann-Hahn condition is achieved by using optimized RF pulses which can make $\vec{B}_1$ fields so strong that $\gamma^I \vec{B}_1^I$ is equal to $\gamma^S \vec{B}_1^S$. In this condition, the *flip-flop* terms described in the homonuclear dipolar interaction case has a big role. They are the factors, really are responsible for the polarization transfer to the S spin, as they find both I and S precess in equal frequency in the rotating frame. In a homonuclear multi-spin (I) system, the *flip-flop* transitions transfer magnetization from one part of the system to other, and the process is called *spin diffusion*. This is a spontaneous process in the presence of strong homonuclear dipolar interaction. So, in other words, CP experiment helps the S spins look similar to I spins in the rotating frame and transfers the large I spin magnetization to S spins. But here the polarization bridge is the dipolar coupling between I and S spins. Therefore, the efficiency of CP heavily depends upon the molecular motion and the MAS spinning rates. But, usually, moderately fast MAS is used along with CP (known as CP-MAS), as one aims better resolution and sensitivity. The CP build-up can address some of the molecular dynamics aspects as well.

Chapter 2

Spin Decoupling

2.1 Introduction

There are two conceptually different classes of spin decoupling in NMR spectroscopy. One is the decoupling of same type of nuclei from each other (like ^{1}H from ^{1}H). This is called homonuclear spin decoupling. The second case is decoupling a nucleus from another (hetero) nucleus (like ^{13}C from ^{1}H). This is the case of heteronuclear spin decoupling. The difference in heteronuclear and homonuclear dipolar interaction Hamiltonians is described in Section 1.2.4. So it needs different approaches to decouple these two interactions. In heteronuclear decoupling, the decoupling frequency (e.g. ^{1}H frequency) and the observed frequency (e.g. ^{13}C frequency) differ by tens or hundreds of MHz usually. This makes it possible to irradiate the abundant nucleus, while the frequency points of the observed nucleus are sampled. In contrast, for homonuclear decoupling, the decoupler frequency lies within the observed frequency range of the spectrum. The method of homonuclear decoupling therefore depends on the time between consecutive sampling points (i. e., dwell time) and decoupling pulse schemes are applied during the dwell time, after each sampling. Then, in solid-state, one has to apply a decoupling RF field so off-resonant that the effective field makes an angle of 54.74° to the static magnetic field. This helps to remove homonuclear dipolar interactions. In solid-state, the presence of CSA and the interference with MAS frequencies make the situation quite complicated. But there are many efficient homonuclear decoupling methods implementing multi-pulse sequences [29]. The popular methods can be divided into four branches, namely, (i) Lee-Goldberg decoupling schemes [30–32], (ii) solid-echo pulse trains [33–35] (iii) magic sandwich echo pulses [36, 37] and (iv) rotor-synchronized schemes [38, 39]. Widely used pulse sequences for homonuclear decoupling include FSLG [31], PMLG [32], DUMBO [40] etc. However, in the present work, we will be solely concerned with heteronuclear spin decoupling.

Heteronuclear spin decoupling is one of the most important tools in NMR spectroscopy for obtaining narrow, highly-resolved spectral lines. The method involves irradiating the nucleus which has a spin-spin interaction (direct or indirect) to the observed nucleus. This is done with a RF field with a frequency equal to the Larmor frequency of the nucleus to be irradiated. The mechanism of this method depends on how efficiently the RF field can average the interaction in spin space, because in real-life samples there are many interactions acting on a spin system. The efficiency may depend upon the range of chemical shift effects

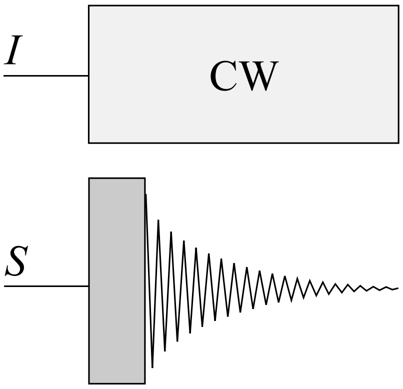

Figure 2.1: The schematic representation of spin decoupling of the abundant spin (I) to observe the rare spin (S) using a long Continuous Wave (CW) irradiation in the I spin channel.

and the interactions like spin-spin couplings. The indirect spin-spin coupling (or J-coupling) and the direct spin-spin coupling (or dipolar coupling) introduces either line splitting (for well-defined spin pairs) or line broadening (for spin ensembles, which are usually encountered in 'real' samples). In solution state, only the isotropic part of scalar J-coupling survives and the dipolar coupling vanishes due to molecular tumbling. In solids the dipolar interaction is much stronger than the indirect coupling and tends to hide the small J-interaction. Therefore, in liquid samples the spin-interaction to be decoupled is the J-coupling and in solids, it is mainly the dipolar coupling. Decoupling the J-interaction with single frequency radio-waves is a relatively easy process, and this results in the NMR spectrum with chemical shift information alone. In a solid sample, one needs very strong RF fields to average dipolar interactions in the spin space. Usually, spin decoupling is applied while observing rare nuclei (like ^{13}C or ^{15}N) dipolar-coupled with abundant nuclei (like ^{1}H or ^{19}F). This method of using a single frequency irradiation, while the nucleus of interest is observed, is called a Continuous Wave (CW) irradiation (Fig. 2.1). Even-though the concept of this double resonant experiment was coined by F. Bloch (1954) [22], the first decoupling experiments were done by A. L. Bloom and J. N. Shoolery in 1955 [23]. Later, F. Bloch described the relevant theoretical aspects [24] behind double resonance experiments. Now-a-days one usually uses multi-pulse sequences to decouple J-interaction, instead of a long single pulse. Popular sequences include MLEV [41], WALTZ [42], GARP [43], DIPSI [44] and WURST [45]. They are also called broad-band decoupling sequences because of their insensitivity to the decoupler offset over a larger range than that with the CW method.

2.2 Origin of Line Broadening in Solid State

When it comes to solid-state NMR, the dipolar interaction to be decoupled is very large when compared to the J-couplings. Spin decoupling in solid state helps to obtain high-resolution NMR spectra. But even under CW spin decoupling, solids show NMR lines of considerable line width. Before understanding the different line broadening mechanisms under decoupling one has to classify general reasons for line broadening in solid state. It can be divided into contributions from both homogeneous and inhomogeneous mechanisms. While homogeneous line broadening is caused by fluctuating local magnetic fields in random fashion, the latter has a stable source. The homogeneous part is mainly composed of homonuclear dipolar interactions among abundant spins. Here MAS is inefficient to average this huge interaction. Large external magnetic fields can increase the separation between closely resonating spins, and slow down the flip-flop process. This situation can help MAS to average dipolar interaction more efficiently. But the most efficient way is to do homonuclear dipolar decoupling [29]. The inhomogeneous broadening mechanisms involve CSA and magnetic field inhomogeneities. MAS can efficiently get rid of some part of the inhomogeneous broadening. The inhomogeneous contribution can be observed by comparing the natural line width and a spin-echo [46] refocused line width. The natural line width is measured from the full width at half maximum (FWHM) of the NMR signal in the frequency domain. A spin-echo line width can be calculated from the T_2 relaxation time obtained from a spin-echo experiment [46–48]. For chemically equivalent spins, fast MAS can finally result in homogeneously broadened lines, with very small contributions from bulk magnetic field inhomogeneities.

But for rare nuclei, the situation is different, as they hardly find each other as neighbors, the homonuclear dipolar coupling contribution to the line width is negligible. On the other hand, the heteronuclear dipolar coupling to abundant nuclei broadens the line. The abundant spin decoupling combined with MAS is an efficient way to get rid of this broadening. The different contributions to residual line-width under CW decoupling are described extensively in the literature [53–56]. The contributions include broadenings due to (i) isotropic spread of chemical shifts of the decoupled abundant nuclei, (ii) off-resonance irradiation of the abundant spins, (iii) insufficient decoupling power and (iv) magnetic susceptibility distributions.

2.3 Decoupling methods in Solid State

In the following subsections, different decoupling methods applied in solid-state NMR are discussed.

2.3.1 Continuous wave (CW) decoupling

After the first introduction of Continuous Wave (CW) dipolar decoupling in solid-state NMR [22–25], this method was used extensively for decades. The decoupling mechanism and the source of residual line-width were still not well-understood.

But it was known experimentally that one should use a RF field stronger than the interaction to observe narrow lines. It was also known that the flip-flop process driven modulations in a homonuclear spin bath can average the heteronuclear couplings (known as *self-decoupling*), if the homonuclear spin-diffusion rates fall in certain regimes [49–51]. The influence of MAS (see Section 1.3.1) on the efficiency of CW decoupling was also studied [52]. Except the instrumental contributions, the main contributor to line width under CW decoupling is the chemical shielding and the dipolar interaction of the abundant spin nuclei. The second-order interaction between the chemical shielding and the heteronuclear dipolar interaction (see Section 2.4.2) is not averaged by CW decoupling. This demanded high efficiency in spin decoupling, and a new era of multi-pulse decoupling sequences followed.

2.3.2 Two pulse phase modulation (TPPM)

R. G. Griffin and co-workers (1995) [57] implemented decoupling experiments with a multi-pulse sequence, namely Two Pulse Phase Modulation (TPPM), which resulted in improved decoupling performance compared to CW method. The TPPM sequence consists of repeating units of two pulses with alternating phases $\tau_{(+\phi)}\tau_{(-\phi)}$, where τ is the pulse duration with a flip angle usually between 160° and 180° and ϕ is the phase angle (usually from 5° to 15°) (Fig 2.2). The TPPM pulse sequence is quite easy to implement, and the two parameters to be optimized are the pulse duration (τ) and the phase angle (ϕ). Under moderate MAS frequencies, TPPM has a comparatively good decoupling efficiency and it is still widely used. The TPPM model has been the base for a large number of decoupling sequences. A survey of such variants of TPPM is done in section 2.3.4. Even-though TPPM is better than CW method in decoupling performance, it shows high sensitivity towards changes in NMR parameters, like frequency offsets, pulse durations, phase angles, RF strengths and MAS frequencies. These experimental observations are explained in chapters 3 and 4.

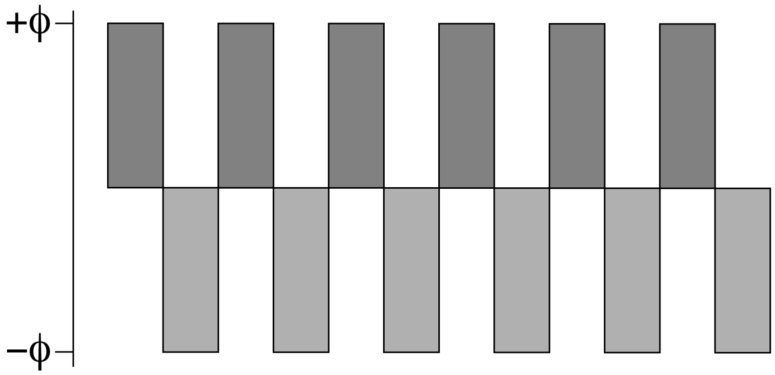

Figure 2.2: The schematic representation of Two-Pulse Phase Modulation (TPPM) decoupling pulse sequence with alternating pulses having inverse phase modulation ($+\phi$ and $-\phi$).

2.3.3 Small phase incremental alteration (SPINAL)

An alternative method was suggested by Fung *et al.* in the year 2000, with the Small Phase Incremental ALteration (SPINAL) sequence [58], which includes phase increments within a block of pulses Q of the form $\tau_{(+\phi)}\tau_{(-\phi)}$ $\tau_{(\phi+\alpha)}\tau_{(-\phi-\alpha)}$ $\tau_{(\phi+\beta)}\tau_{(-\phi-\beta)}$ $\tau_{(\phi+\alpha)}\tau_{(-\phi-\alpha)}$ (Fig 2.3). The most efficient phase increments usually are $\alpha = 5°$ and $\beta = 10°$. Many super-cycled sequences of SPINAL were tested. One of the most efficient was the one with eight pulse-train-blocks arranged as $Q\bar{Q}\bar{Q}Q\bar{Q}QQ\bar{Q}$, known as SPINAL-64. Here, $\bar{Q}$ indicates Q block with inverse phases. Since a Q block starts without any phase increment and ends with α increment, the block itself and its super-cycles are not completely symmetric. In TPPM, the phase modulation is confined between the two consecutive pulses, but in SPINAL, the phase modulation is extended to many pulses. This is considered to be the reason for its improved decoupling performance over CW and TPPM methods. Although SPINAL-64 was initially designed for liquid crystal NMR, it also works well for crystalline solids and has been shown to outperform TPPM in many instances [58–60]. However, like TPPM, the performance deterioration due to different NMR parameter offsets, is still a drawback of the method.

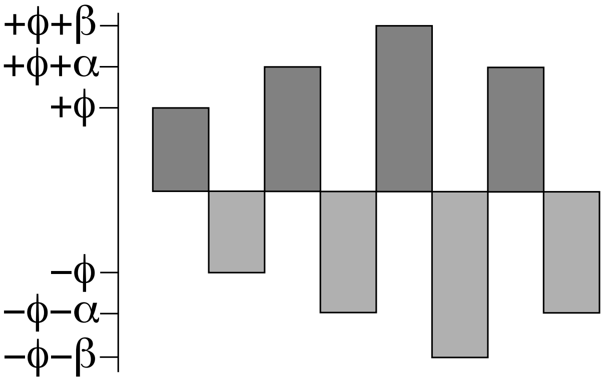

Figure 2.3: The schematic representation of the basic block of Small Phase Incremental ALteration (SPINAL) decoupling pulse sequence with alternating pulses having inverse phase modulation ($+\phi$ and $-\phi$) and with phase increments α and β.

2.3.4 Other decoupling sequences

Several other multi-pulse decoupling sequences were introduced based on the concept of phase modulation. Based on an earlier suggestion by Tekely *et al.* [61], a phase modulated decoupling scheme was presented with repeating units of two pulses with 180° phase shift, known as X-inverse-X (XiX) [62]. For the XiX scheme, one has to multiply a constant to the rotor period (τ_r) to get a good decoupling pulse (τ_p). Since the performance of the sequence heavily depends on both τ_r and τ_p, the regions for good decoupling are very narrow. It is also known that the XiX sequence works well only at high MAS frequencies ($\geq$ 25 kHz) [62]. Other approaches based on the TPPM model include Frequency and Phase Modulation (FMPM) [63], Cosine Modulated (CM) TPPM [64], Phase-Wiggled (PW) TPPM [65] and the recently introduced High Phase TPPM [66]. Similar to XiX, the High Phase TPPM also works good at high MAS frequencies, and as the name suggests, it has very high phase angles ($\sim$ 150°). A theoretical analysis of phase-modulated sequences was presented recently by M. Ernst and co-workers [67]. Further, there are conceptually different symmetry-based sequences [68, 69], rotor synchronized PISSARRO (Phase-Inverted Supercycled Sequence for Attenuation of Rotary Resonance) [70] and Hahn-Echo trains [71], which also result in efficient dipolar decoupling. Among the above-mentioned sequences, XiX, PISSARRO and High Phase TPPM are used in regimes, where the MAS frequencies and the *RF* strengths become comparable. Since, in the present work, decoupling under only moderate MAS frequencies are explored, the methods XiX, PISSARRO and High Phase TPPM are not used. The methods which are under study in this work are TPPM, SPINAL and the frequency-swept versions of them (i.e., SW$_f$-TPPM [72] and SW$_f$-SPINAL [73]). The design of different frequency-swept decoupling schemes, their applications, and the comparative decoupling performances are detailed in Chapters 3 and 4.

2.4 Dipolar Decoupling Related Phenomena

In NMR, real spin systems in a static magnetic field always evolve under internal spin interactions. Dipolar coupling (see Section 1.2.4) is a relatively large internal interaction under which the spins evolve, and decoupling methods help to remove this influence on the system. As mentioned before decoupling involves spin-space averaging of the dipolar interaction. It is, thus, expected that a long-lasting oscillating magnetic field provided by the CW method can average the dipolar interaction quite efficiently. For example, with MAS, one can average completely the CSA interaction. However, commercially available MAS probes cannot spin fast enough to average dipolar couplings, which are up to around 100 kHz. Therefore dipolar decoupling remains the only possible solution for this. But CW averaging is not a sufficient method in this regard as pointed out several times [54–56] even for an isolated two-spin system. This needs a deeper understanding of the interactions involved, especially inclusion of higher order perturbations in the picture.

2.4.1 Interaction between *RF* field and MAS

Isolated I and S spins which are dipolar coupled are considered in a solid system. Let the S spin signal be observed under MAS at frequency of ω_r and I spin irradiation at the Larmor frequency. The *rotory resonance* condition is met when the nutation frequency of the irradiation field B_1^I matches a small multiple of the

MAS frequency:

$$\omega_1^I = -\gamma^I B_1^I = n\omega_r \qquad n = \pm 1, \pm 2, ... \tag{2.1}$$

Under rotary resonance conditions, a recoupling effect is observed [75]. This is termed as *Rotary Resonance Recoupling* or R^3. This leads to S spin line broadening due to the reintroduced $I - S$ dipolar coupling. The dipolar coupling should actually be averaged out under MAS, but the RF irradiation recouples it. The rotation of the spin states by the RF irradiation at the same frequency as the sample rotation causes the spin density operator to evolve much as if the sample were static but chemical shifts were absent [75]. First and second recoupling conditions contribute the most. $n = 3$ and 4 recoupling conditions also exist, but experimentally they are less influential. In systems with very strong dipolar couplings, recoupling of I spin homonuclear interaction occurs at $n = 0.5$. This is called the HORROR (*Homonuclear Rotational Recoupling*) condition [76], which helps heteronuclear decoupling by adding its contribution through *self-decoupling*. Rotor synchronized sequences like PISSARRO and sequences with very high phase angles, namely, XiX (with τ_r dependent pulses) and High Phase TPPM are specially designed to suppress the rotary resonance conditions [62, 66, 70]. But the substitution of CW with a multi-pulse decoupling method under MAS can introduce yet another time dependence, based on the cycle times (τ_c) of the sequence [55, 56]. In general it is advised to avoid *rotary resonance* by choosing suitable RF fields and MAS frequencies.

2.4.2 Second-order recoupling of chemical shielding and dipolar coupling

There is another effect similar to the rotary resonance recoupling, namely the second-order recoupling of chemical shielding and dipolar coupling under spin decoupling [20]. Again two isolated spins I and S are considered, for understanding the observation of S spin under CW irradiation at the Larmor frequency of I spin. Similar to R^3 effect, a recoupling is observed in the rotating frame between the dipolar coupling tensor and the chemical shielding tensor of I spin. This effect gives rise to line splitting and additional line broadening of the S spin resonance. In the limit of strong decoupling, the effect on the resonance frequency of the S spin is described by [20] :

$$\omega(\Omega_D, \Omega_I, \Omega_S) \approx \omega_S(\Omega_S) \pm \left(\frac{\omega_D(\Omega_D)\ \omega_I(\Omega_I)}{\omega_{RF}} \right) \tag{2.2}$$

Here, the Ω_x are the Euler angles $\Omega_x = (\alpha_x, \beta_x, \gamma_x)$ describing the orientation of the respective interactions (D - dipolar, I - chemical shielding of the I spin, S - chemical shielding of the S spin) in the laboratory frame.

In a notation using spherical tensors for all interactions [20], the second-order recoupling can be expressed as the sum of three different terms, which scales as a zeroth-rank (scalar), a second-rank, and a fourth-rank tensor. The second and fourth rank tensors scale like Legendre polynomials of the order two and four respectively (Figure 2.4). Under MAS, the second-order contributions are averaged out, so that only an isotropic part (zeroth-rank) and a scaled fourth-rank term remain. The isotropic part causes a splitting, and the orientation dependence encapsulated by the fourth-rank tensor component broadens this doublet. This situation is similar to the broadening of the central transition of half-integer spin quadrupolar nuclei. Mechanical high-resolution methods applied for quadrupolar nuclei (such as DAS and DOR) can be used here as well to get rid of the broadening caused by the fourth-order term as explained in detail in Chapter 6.

In the context of heteronuclear spin decoupling, it is important to realize that for an isolated $I-S$ spin pair under CW decoupling, the splitting of the S spin line always remains, regardless of the strength of the RF field [20]. In practice, the line splitting caused by the second-order recoupling is not very prominent, as in most solids, strong homonuclear couplings between the abundant I spins exist. The flip-flop terms of the homonuclear dipolar coupling Hamiltonian lead to an additional modulation of the heteronuclear dipolar coupling which results in line-narrowing (also referred to as self-decoupling). But if one wants to remove the splittings caused by the second-order recoupling by RF irradiation alone, symmetric multi-pulse sequences are required. Such sequences are capable to eliminate all odd orders of the average Hamiltonian, so that the second-order

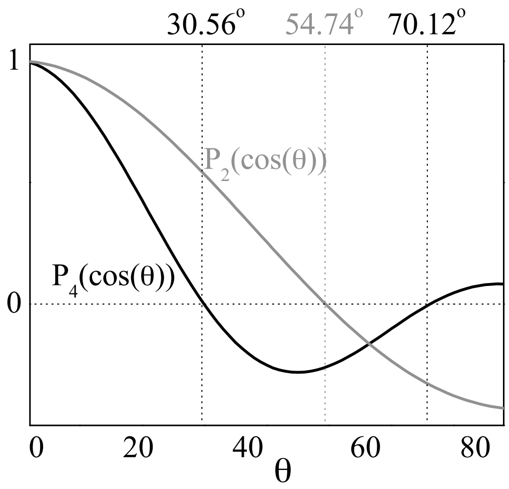

Figure 2.4: The angular dependence behavior of second and fourth rank dipolar-chemical shielding recoupling interactions scaling like Legendre polynomials of the order two (grey) and four (black) respectively.

recoupling is suppressed. The simplest such pulse sequence is TPPM, consisting of pulses with alternating phases $\pm\phi$. This sequence can be viewed as a strong CW decoupling field with an orthogonal phase-alternating field superimposed on it [20]. While the former part ensures the system to be in the strong decoupling limit, the later reduces the second-order recoupling effects. The fact that symmetric multi-pulse sequences (such as TPPM and related sequences) are capable of suppressing the line broadening caused by the second-order effects described above makes their application in solid-state NMR particularly useful, and motivate the on-going research in this field.

2.4.3 Effect of MAS on abundant spin network

With increasing MAS frequencies the line-widths were reported to increase under CW decoupling [54, 55]. This highly complicated phenomenon suggested an invisible role of abundant spin homonuclear networks in the heteronuclear interaction with the rare spin. The high MAS speeds weakens the coupled abundant spin bath, which, in fact, would have helped to have a self-decoupling effect. But fast MAS reduces the rate of this spin diffusion process and yields broad lines. This effect is also well taken care of with efficient decoupling sequences. Including the homonuclear interactions in numerical calculations, without defining the fate of spin-diffusion, can therefore impose difficulties [74].

2.4.4 Off-resonance behavior of decoupling

Analyzing the intensity values of the S spin NMR signal as a function of decoupling-transmitter offset (on the I spin channel), is a useful method to check the effective decoupling range. This method describes how robust a decoupling pulse sequence is towards decoupler offset change. A series of deliberate off-resonance decoupling experiments ranging $\pm\Delta\nu_{RF}$ kHz from the resonance frequency of I should be carried out for this test. The expected decoupling behavior is a parabolic dependence of line width from the offset change [53, 77]. The line width increases parabolically to both positive and negative changes of $\Delta\nu_{RF}$. But the peak heights (or

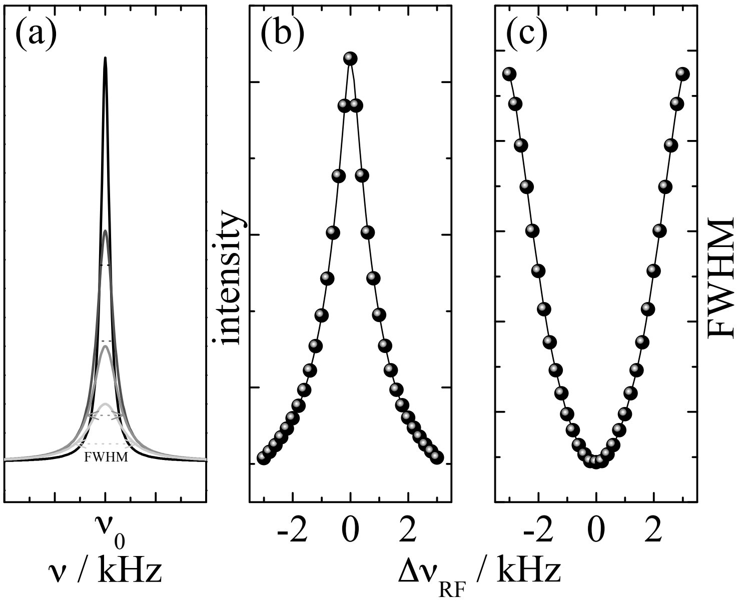

Figure 2.5: A schematic representation of (a) Lorentzian line shape of the S spin NMR signal under TPPM decoupling. The peak height (intensity) decreases and the full-width at half-maximum (FWHM) increases, while the decoupler (I spin) offset ($\Delta\nu_{RF}$) moves away from the *on-resonance* condition. The dependence of the S spin (b) intensity and (c) FWHM on the decoupler offset is also shown.

intensities) behave differently. The intensity of a Lorentzian line can be expressed as:

$$L(\nu) = \frac{2T_2^\star}{1 + 4\pi^2 T_2^{\star 2}(\nu_0 - \nu)^2} \tag{2.3}$$

Here $T_2^\star$ is the inhomogeneous T_2 and ν_0 is the resonance frequency. At half height of the Lorentzian, $L_{FWHM}(\nu) = \frac{1}{2}L(\nu_0)$ and the frequency,

$$\nu_{FWHM} = \nu_0 \pm \frac{1}{2}\,\frac{1}{\pi T_2^\star} \tag{2.4}$$

Therefore the magnitude of full-width at half-maximum (FWHM) for *on-resonance* condition,

$$\Delta\nu_{FWHM} = \frac{1}{\pi T_2^\star} \tag{2.5}$$

For *off-resonance* condition, there is additional broadening caused by the irradiation offset, the dependence of which is parabolic [77].

$$\Delta\nu_{FWHM} = \frac{1}{\pi T_2^\star} + b(\Delta\nu_{RF})^2 \tag{2.6}$$

Here the second term has a constant b defining the curvature of the parabola and the change in RF irradiation frequency offset $\Delta\nu_{RF}$. This expression when substituted in equation 2.3, with $\nu = \nu_{FWHM}$, gives the offset-dependent line intensities $L_{FWHM}(\Delta\nu_{RF})$. Now, if one plots the dependence of maximum line intensity $L(\nu_0) = 2L(\nu_{FWHM})$ on RF offset $\Delta\nu_{RF}$, it has a Lorentzian form.

This offset dependence behavior of decoupling is strongly influenced by the residual I spin chemical shielding anisotropy. For polycrystalline samples under MAS, the condition of $\nu_{RF}^I > \nu_r$ is more favored than $\nu_r > \nu_{RF}^I$. This is because for averaging the off-resonance contributions to the line width, the modulation of I spin operator via ν_{RF}^I is much more effective than that with ν_r [77]. Since these contributions are completely dependent on I spin chemical shielding, they also differ for different nuclei. For example, decoupling ^{19}F has more off-resonance-irradiation dependent line-width factors observed in the S spin signal than that for ^{1}H. This makes ^{19}F decoupling difficult, and Chapter 5 discusses different efficient ^{19}F decoupling methods from the present work.

Chapter 3

Frequency-Swept TPPM

3.1 Introduction

The heteronuclear spin decoupling sequences TPPM and SPINAL definitely outperform the CW method, in decoupling efficiency. But they are quite sensitive to parameters like phase angles, pulse durations and decoupler offsets. A search for a robust sequence by P. K. Madhu and co-workers resulted in the introduction of a new method, *frequency-swept TPPM* (or SW$_f$-TPPM) [72]. The method outperformed both TPPM and SPINAL and showed considerable insensitivity towards the above-mentioned NMR parameters. The robustness towards decoupler offset is quite a necessary criteria for decoupling in solid state NMR. This helps to avoid troubles in finding an exact decoupler frequency in a system with heavily broadened NMR signal of abundant nuclei.

3.2 Frequency Sweep Profiles

In the SW$_f$-TPPM decoupling sequence, incremented pulse durations (τ_p) are used, causing a sweep in the modulation frequency (hence SW$_f$), while the TPPM phase angles ($+\phi$, $-\phi$) remain constant (Fig. 3.1). Within one SW$_f$-TPPM cycle consisting of N pulse pairs, the pulse duration of the nth pulse, τ_p^n (with $n = 0, 1, \ldots, N-1$), is modified by a multiplication factor $\tau_p^n = f^n \tau_p$, with the best duration τ_p being usually close to the value used for TPPM (i. e., close to flip angles in between 160° and 180°). Thus the pulse durations are multiplied with a series of factors which range from values below unity to values above unity in a symmetrical manner. The exact manner of pulse incrementation defines a *sweep profile*, which can be pictured by plotting the multiplication factors for the pulse duration τ_p *versus* the pulse-pair index, as shown in Figure 3.2.

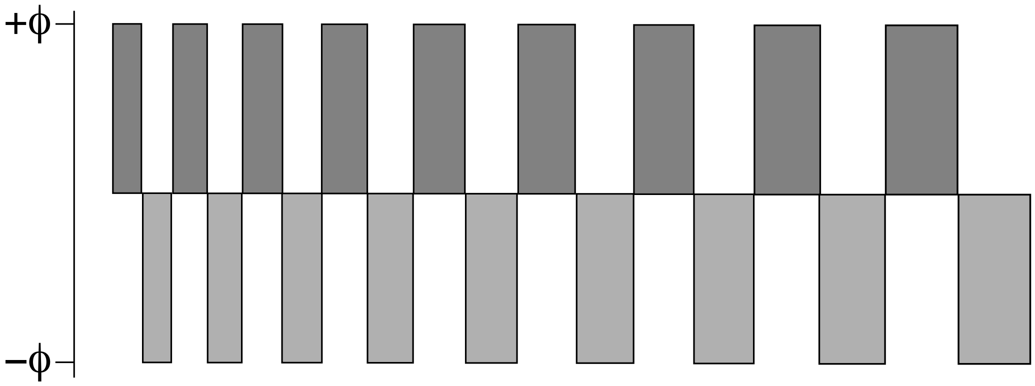

Figure 3.1: The schematic representation of SW$_f$-TPPM decoupling pulse sequence.

3.2.1 Tangent sweep profiles

In some first published reports about the applications of SW$_f$-TPPM, an approximated tangent profile has been utilised for proton decoupling of crystalline tyrosine, and an exact tangent (denoted SW$_f^{tan}$ here) has been used for proton decoupling for acquisition of ^{27}Al spectra of the mineral, gibbsite [79]. Both the SW$_f^{tan}$ and the so-called *inverse* profile have been used for proton decoupling of the liquid crystalline compound MBBA [80]. As shown in Figure 3.2, one can obtain different tangential profiles for constructing different SW$_f^{tan}$-TPPM sequences, for comparison of decoupling efficiencies. The design of such profile involves variation of four parameters, namely, the number of pulse pairs (N), the first multiplying factor (f^0), the final multiplying factor (f^{N-1}), and the tangent cut-off angle (t_{co}). Now, the multiplication factor for the nth pulse pair (f^n) is

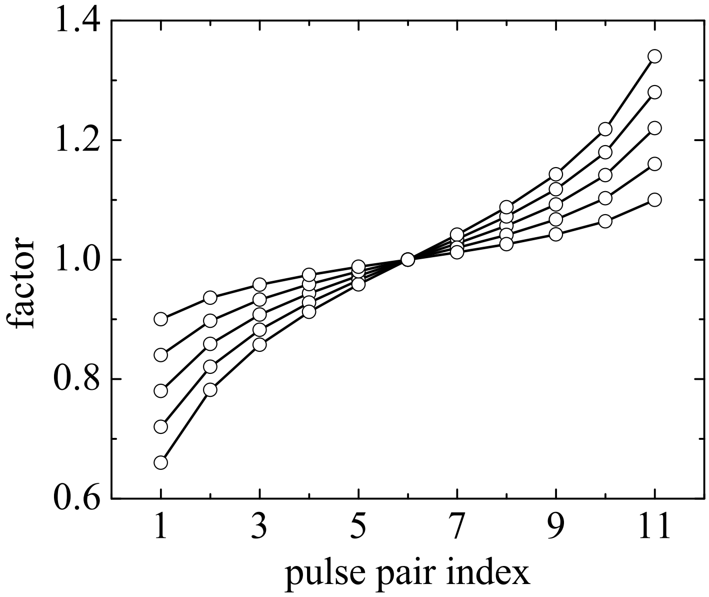

Figure 3.2: The tangential sweep profiles of SW_f^{tan}-TPPM decoupling sequence.

defined as,

$$f^n = f^0 + \frac{d}{2}\left(1 + \frac{tan(x)}{tan(t_{co})}\right) \tag{3.1}$$

There are two derived parameters in this expression, d and x. Here d is defined as the difference between the factors which are used to multiply the first and final pulse-pairs,

$$d = f^{N-1} - f^0 \tag{3.2}$$

and x is defined as,

$$x = t_{co}\left(-1 + \frac{2}{N-1}\, n\right) \tag{3.3}$$

All the four factors (N, f^0, f^{N-1} and t_{co}) which defines a tangential profile may influence the decoupling performance of the sequence, and therefore, they should be optimized. The efficiency of SW_f^{tan}-TPPM was found to be outperforming TPPM and SPINAL when eleven number of pulse pairs were used for a single tangential sweep [72]. This was also proved with numerical simulations using the SPINEVOLUTION program, by doing virtual decoupling experiments on a system of ^{13}C nucleus dipolar coupled with four protons [74].

A tangential sweep with 11 pulse pairs can only be one of the approximations of adiabatic sweep. So, there can be other styles of pulse duration modulation, like the so-called inverse profile [80]. But before starting to use different sweep profiles, one has to consider the relative gain in decoupling performance and the time spent in optimizing different parameter of complex sequences.

3.2.2 Linear Frequency Sweeps

The conceptually easiest way to create a frequency sweep is to multiply the pulse durations with factors which increment linearly. From a theoretical evaluation, it was recently judged that a ”linear sweep ... clearly performs equally well as the tangential sweep...” [74]. This finding was supported by only a few experimental data on crystalline glycine [74]. This section describes the design and experimental applications of a frequency-swept TPPM method with a linear sweep profile (SW$_f^{lin}$-TPPM) [81]. The sweep profiles can be visualized as shown in Figure 3.3, for 11 pulse pairs. The multiplication factor for the nth pulse pair (f^n) in this case is,

$$f^n = f^0 + n\Delta \tag{3.4}$$

where the parameter Δ is,

$$\Delta = \frac{f^{N-1} - f^0}{N-1} \tag{3.5}$$

Such a SW$_f^{lin}$-TPPM profile is defined by only three parameters (N, f^0 and f^{N-1}), and therefore easier to implement and optimize than any other complex sweep profiles [81]. But the important thing is, how strong the decoupling efficiency is dependent on the tangential and linear sweep profiles. To understand this decoupling experiments were done with TPPM, SPINAL, SW$_f^{tan}$-TPPM and SW$_f^{lin}$-TPPM for comparison.

All experiments were performed on a Bruker AVANCE-II 400 spectrometer, using a 4 mm double-resonance MAS probe. ^{13}C-NMR spectra of natural abundance tyrosine hydrochloride (Sigma Aldrich) were acquired using cross-polarisation with a contact time of 2 ms. For each spectrum, 128 transients were accumulated, with a recycle delay of 4 s. The pulse sequences for proton decoupling were implemented using the Bruker convention for defining so-called cpd programmes that are executed on the proton channel during acquisition [81].

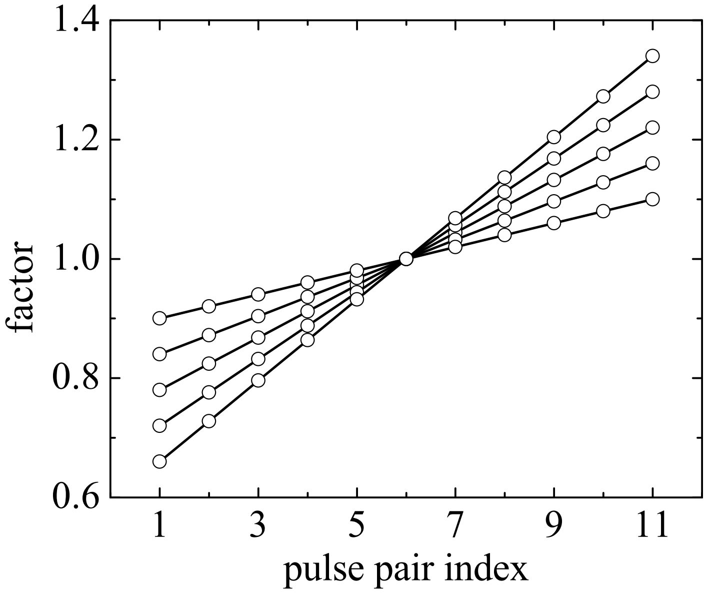

Figure 3.3: The Linear sweep profiles of SW$_f^{lin}$-TPPM decoupling sequence.

Decoupling performance of different pulse sequences was compared monitoring the intensity of the ^{13}CH$_2$ resonance of crystalline tyrosine. Figure 3.4 shows the decoupling efficiency of TPPM, SPINAL, SW$_f^{tan}$-TPPM and SW$_f^{lin}$-TPPM as a function of decoupler frequency offset for a MAS rate of 10 kHz. As explained in Section 2.4.4, the decoupling efficiency drops when moving away from the optimal decoupler frequency to either positive or negative offsets, in a parabolic function for the line width [77] that is reasonably smooth and symmetric around zero offset. For a more efficient evaluation of the decoupling efficiency of a given sweep profile, a figure-of-merit parameter η was defined, for which only the line intensities $I(\nu_{off})$ at 0, 2, 4 and 6 kHz were acquired and added, $\eta = I(0 \text{ kHz}) + I(2 \text{ kHz}) + I(4 \text{ kHz}) + I(6 \text{ kHz})$. Some details may be lost in this summation representation, for instance if the relative performance order of the considered sequences changes for far off-resonance conditions [81].

An example for such behaviour can be seen in Figure 3.4, where TPPM gives better decoupling than any other sequences at far off-resonance (6 kHz). However, the desired characteristic of a decoupling sequence is good aggregate performance over the entire range of frequency offsets. Therefore, η reflects the efficiency of a given sequence reasonably well, as may be seen by comparing the plots in Figures 3.4 and 3.5(a). By acquiring only those spectra necessary to compute η, the parameter space of the decoupling sequences can be searched much faster. In Figure 3.5(a), the decoupling performance of SW_f^{tan}-TPPM and SW_f^{lin}-TPPM is compared by plotting the efficiency parameter η for the different sweep ranges d, with examples of the profiles used displayed in Figures 3.2 and 3.3. It can be seen from Figure 3.5(a) that over the range of different d's used, the linear sweeps slightly outperform the tangential profiles, while both varieties of SW_f-TPPM give better results than the established sequences TPPM and SPINAL-64.

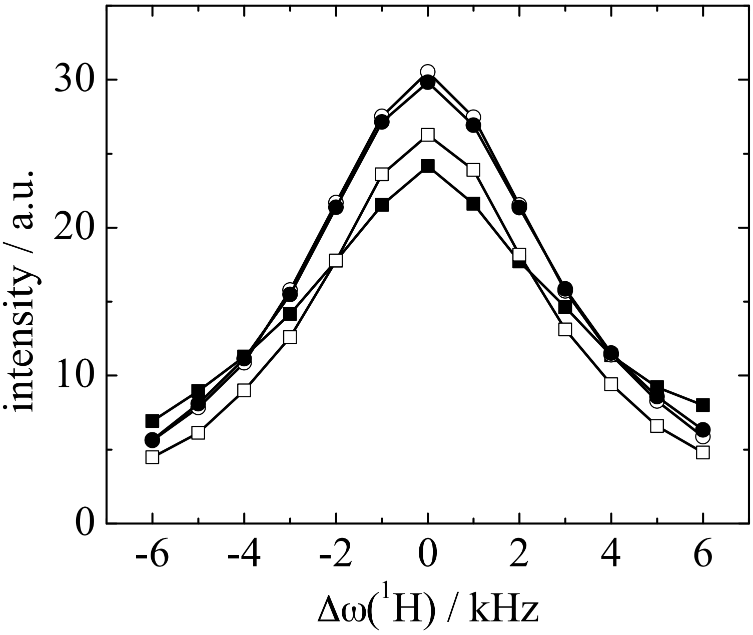

Figure 3.4: Intensities of the $^{13}CH_2$ resonance of crystalline tyrosine as a function of decoupler frequency offset at 10 kHz MAS.The methods compared are (■) TPPM, (□) SPINAL-64, (●) SW_f^{lin}-TPPM and (○) SW_f^{tan}-TPPM decoupling sequences.

Before the data relating to best decoupling performance shown in Figure 3.4 could be recorded, the parameters for the respective sequence had to be optimised. Figure 3.5(b) shows the change of decoupler efficiency when varying the pulse durations, τ_p. It can be seen that the optimal τ_p is different for TPPM (τ_p = 5.75 μs), SPINAL-64 (τ_p = 5.5 μs), and SW$_f$-TPPM (τ_p = 6.0 μs, for both tangential and linear sweeps). When translating these pulse durations into proton flip angles, they all fall between 160° and 175°, with a pulse duration of $\tau_p = 6.2$ μs corresponding to a 180° flip angle. Figure 3.5(b) also documents that the SW$_f$-TPPM sequences show the most robust response towards missetting τ_p, whereas TPPM suffers the fastest loss of performance when moving away from the best τ_p value. Another similar situation exists for varying the phase angle ϕ of the pulses. While the optimal value for ϕ differs between TPPM (ϕ = 6.25°) and the other sequences, (SPINAL-64: ϕ=12.5° plus α = 5°, β = 10°; SW$_f$-TPPM: ϕ=12.5°), TPPM is less robust against variation of the phase angle than SPINAL-64 and the SW$_f$-TPPM sequences. The relative sensitivity of TPPM to missetting τ_p and/or ϕ may be attributed to the absence of a compensation mechanism in this sequence. Unlike SPINAL-64, where supercycles of a basic building block are used, and SW$_f$-TPPM, which covers a range of modulation frequencies, TPPM performs well only for a narrow range of parameter settings [81].

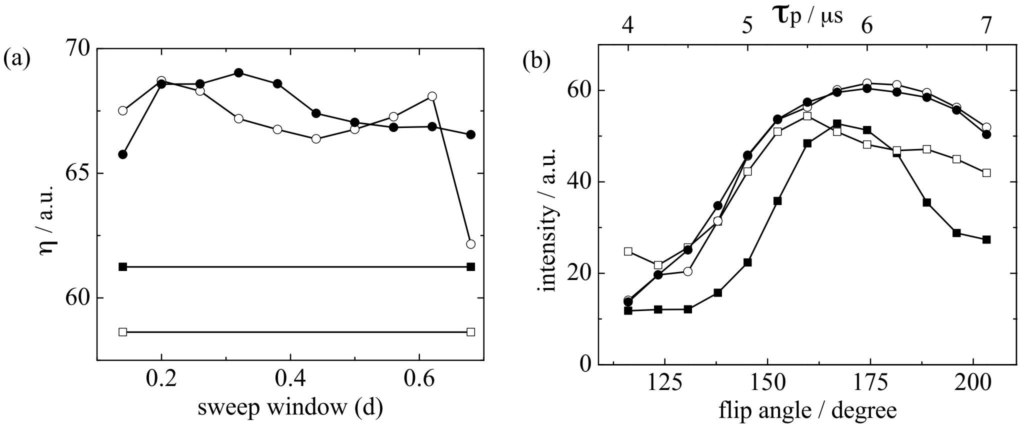

Figure 3.5: (a) Plot of ($^{13}CH_2$ of tyrosine) summed intensities η as a function of sweep ranges d for SW$_f$-TPPM sequences with tangential sweep profile (○) and with linear sweep profile (●). For comparison, the d-independent ηs for TPPM (■) and SPINAL-64 (□) are also shown. (b) Intensities of the $^{13}CH_2$ resonance of tyrosine as a function of pulse duration τ_p offset at 10 kHz MAS at optimal decoupler frequency.

As mentioned before, the SW_f^{tan}-TPPM sequence requires an additional parameter as compared to the linear sweep profiles, namely the cut-off angle for the $tan(x)$ function, expressed as t_{co}. The choice of t_{co} determines the curvature of the sweep profile. From the plot in Figure 3.6(a), it can be seen that the correct setting of this parameter is important for the decoupling efficiency achieved with SW_f^{tan}-TPPM. At a MAS rate of 10 kHz, rate (Figure 3.6(a)), best performance is obtained for $t_{co} = 50°$, which is only a slightly curved profile. For the tyrosine sample, the optimal value for t_{co} was found to be changing with with spinning speed. This shows how vital is the optimisation of the tangent cut-off angle for a good performance of a SW_f^{tan}-TPPM sequence, whereas for the linear sweep profiles used in SW_f^{lin}-TPPM, this additional parameter is not required. This simplifies the optimization of the linear profiles, with no apparent loss of performance. However, it is still important to optimize the sweep range (or *sweep window*) for SW_f-TPPM with both tangential and linear sweep profiles, since the optimal range changes with the MAS frequency, as shown in Figure 3.6(b) [81].

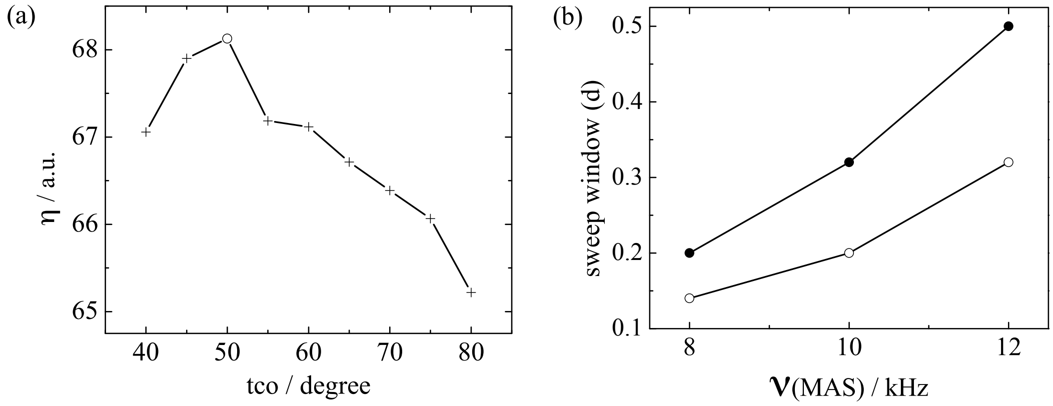

Figure 3.6: (a) Plot of summed intensities η of the $^{13}CH_2$ resonance of tyrosine as a function of the cut-off angle t_{co}, obtained with the SW_f^{tan}-TPPM sequence at 10 kHz MAS rate. Best performance is achieved for $t_{co} = 50°$. (b) Best sweep ranges d for the decoupling sequences SW_f^{tan}-TPPM (○), and SW_f^{lin}-TPPM profile (●), as a function of MAS rate.

In order to verify and compare different decoupling sequences with radio-frequency sweeps, numerical simulations were done using the SPINEVOLUTION program [84]. The model spin system was a ^{13}C, dipolar-coupled with four protons arranged in a glycinyl structural backbone. The results are displayed as the

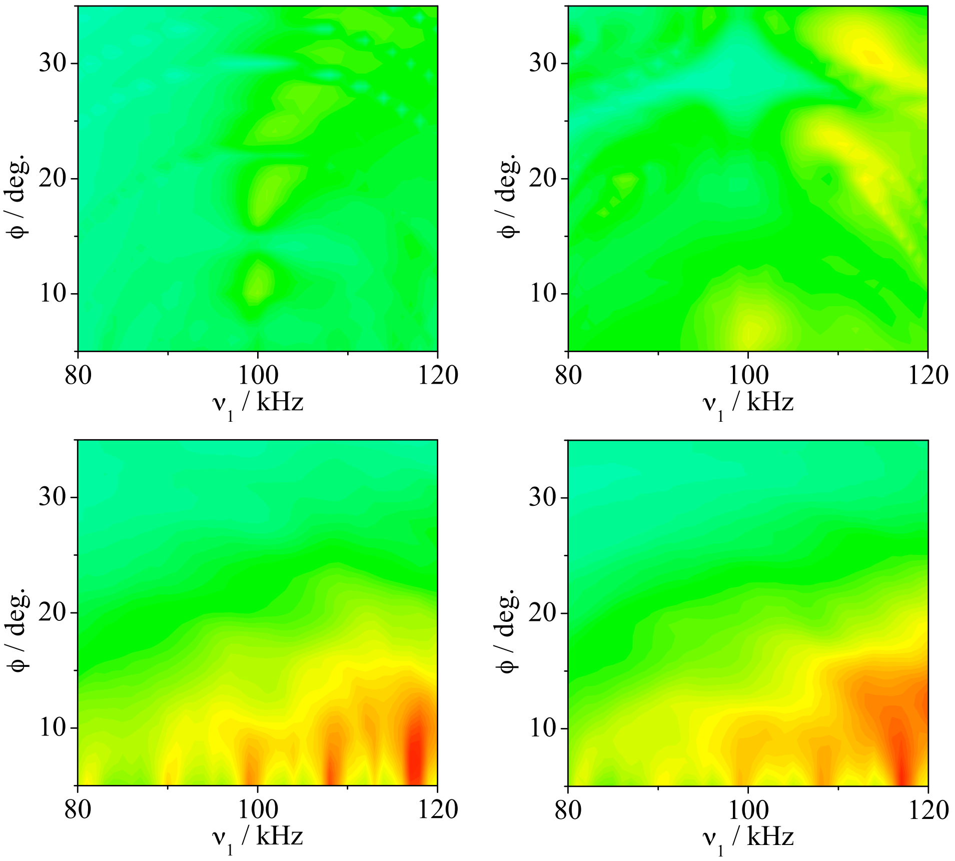

Figure 3.7: SPINEVOLUTION numerical simulations of comparison of ^{1}H decoupling efficiencies of TPPM (top left), SPINAL-64 (top right), SW$_f^{lin}$-TPPM (bottom left) and SW$_f^{tan}$-TPPM (bottom right) in a system of one ^{13}C dipolar-coupled with four ^{1}Hs. Plotted are the ^{13}C signal intensities (increase from green to red) as a function of phase angles (ϕ) of the decoupling sequence and the range of *RF* strengths (ν_1).

absolute intensities of the ^{13}C resonance as a function of the *RF* amplitude (ν_1) and phase angle (ϕ), as shown in Figure 3.7. 5 μs pulse duration was chosen for all the simulations. The sequences with TPPM basic blocks were simulated at a MAS frequency of 9.0909 kHz, while the ones with SPINAL basic blocks were simulated at 8.3333 kHz MAS frequency, in order to speed up computation by avoiding interference effects with the decoupling sequence cycle. All the simulations were done with the H–H homonuclear couplings enabled. The RF amplitude ν_1 was varied from 80 to 120 kHz in step of 1 kHz while the phase angle ϕ was scanned from 5° to 35° in 1° step width. The values for the phase settings were identical for TPPM and SW$_f$-TPPM, with additional phase increments $\alpha = 5°$ and $\beta = 10°$ included for SPINAL and SW$_f$-SPINAL. A line broadening factor of 5 Hz was used for all calculations. From Figure 3.7, it is obvious that both the SW$_f$-TPPM sequences outperform TPPM and SPINAL-64 by a considerable margin over a wide range of phase angles and RF amplitudes. The decoupling performances of SW$_f^{lin}$-TPPM and SW$_f^{tan}$-TPPM are very much comparable.

3.3 Improved efficiency of frequency-swept decoupling

A Floquet analysis to assess the efficiency of decoupling methods has been done by M. Leskes *et al.* [74]. Floquet theory is a powerful method to solve the time-dependent Schrödinger equation governing the evolution of the spin system. The Floquet approach is essentially used to remove the time dependence, by replacing the finite-dimensional, time-dependent Hamiltonian by an infinite-dimensional, time-independent Hamiltonian [82]. Leskes *et al.* [74] utilized bimodal Floquet theory, to be able to deal with the two time dependencies imposed by MAS and RF irradiation. For the effective Hamiltonian thus derived for an isolated spin pair, it was found that it possesses a residual field component along y-direction. This component is conceptually identical with the second-order recoupling (see Section 2.4.2). The effect of the applied multi-pulse sequence must be such as to eliminated the I_y coefficients of the effective Hamiltonian to obtain narrow lines for the S spin. This is termed the *decoupling condition*. The Floquet analysis further showed that for TPPM and SPINAL sequences, the regions in parameter space where the decoupling condition is met are fairly narrow. The advantage of the frequency-swept sequences is to widen the regions where the decoupling condition holds, thus leading to improved, more robust decoupling performance.

A much general case of a rare S spin coupled to N number of abundant (I) spins is considered to study the effects of RF decoupling. The rotating-frame total Hamiltonian of such a case contains terms describing chemical shielding and dipolar coupling interactions, in addition to the RF field. The RF Hamiltonian has Fourier expansion coefficients (ϵ_k) describing the decoupling sequence. From the effective Hamiltonian a transformation is done to bimodal Floquet formalism for the analysis. The Hamiltonian is separated into two parts with respect to the $\alpha(+)$ and $\beta(-)$ eigen-states of the S spin operator. It generates two terms ($\Delta\Omega^{\pm}$) which contain I spin chemical shielding and dipolar interactions. The $\Delta\Omega^{\pm}$ coefficients create a difference between $\hat{\mathscr{H}}^{\pm}_{eff}$ effective Hamiltonians. The $\hat{\mathscr{H}}^{\pm}_{eff}$ contains three terms: (i) $\hat{\mathscr{H}}^{RF}_{eff}$ (which is independent of $\Delta\Omega^{\pm}$), (ii) $\hat{\mathscr{H}}^{(CS-IS)RF}_{eff}$ (which depends on $\Delta\Omega^{\pm}$ only in the case of off-resonant irradiation) and (iii) $\hat{\mathscr{H}}^{(CS-IS)\pm}_{eff}$. The third term includes I spin CSA, $I-S$ coupling and CSA - $(I-S)$ cross terms. They are the true responsible factors for the difference in $\hat{\mathscr{H}}^{\pm}_{eff}$. They have their residual field component (under MAS and on-resonant irradiation) along the y-direction, which is the source of broadening in S spin signal. An efficient decoupling sequence is defined to minimize this difference to make $\hat{\mathscr{H}}^{+}_{eff} \approx \hat{\mathscr{H}}^{-}_{eff}$, by providing suitable ϵ_k factors [74].

An efficient route to achieve the equivalence of $\hat{\mathscr{H}}^{+}_{eff}$ and $\hat{\mathscr{H}}^{-}_{eff}$ is by making the RF Hamiltonian coefficients time-dependent. This is done by adiabatic change of one of the ϵ_k factors which include RF phase, RF amplitude and frequency of modulation. For example, in the case of TPPM, the modulation frequency $\omega_{tppm} = 2\pi/t_{tppm}$, during a certain period τ_c can be swept to obtain a decoupling method of high efficiency. This method is the previously described frequency-swept TPPM (or SW$_f$-TPPM) [72]. Since the decoupling is done under MAS, the efficiency of it depends on possible interactions of RF field (ν_{RF}) with rotation frequency (ν_r) and modulation frequency (ν_c) [72, 74].

3.4 Frequency Sweep Direction

Usually, a RF sweep starts from a high frequency and continues to a low frequency (in other words, from short pulse pairs, sequentially to long pulse pairs) is used in any of the above mentioned cases (Fig. 3.1). This section investigates the effect of sweep direction in the decoupling performance of SW$_f$-TPPM by experiments, numerical simulations and theoretical Floquet analysis. Throughout this section,

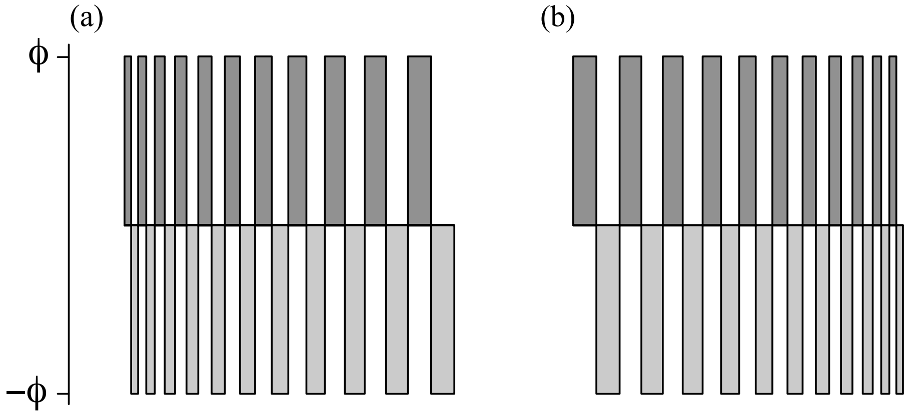

Figure 3.8: The SW$_f$-TPPM decoupling sequence with (a) forward (SW$_f$-for-TPPM) and (b) reverse (SW$_f$-rev-TPPM) sweep profiles.

a *RF* sweep from high frequency to low frequency is designated as a *forward sweep* and the *RF* sweep from a low frequency to a high frequency as a *reverse sweep* [83].

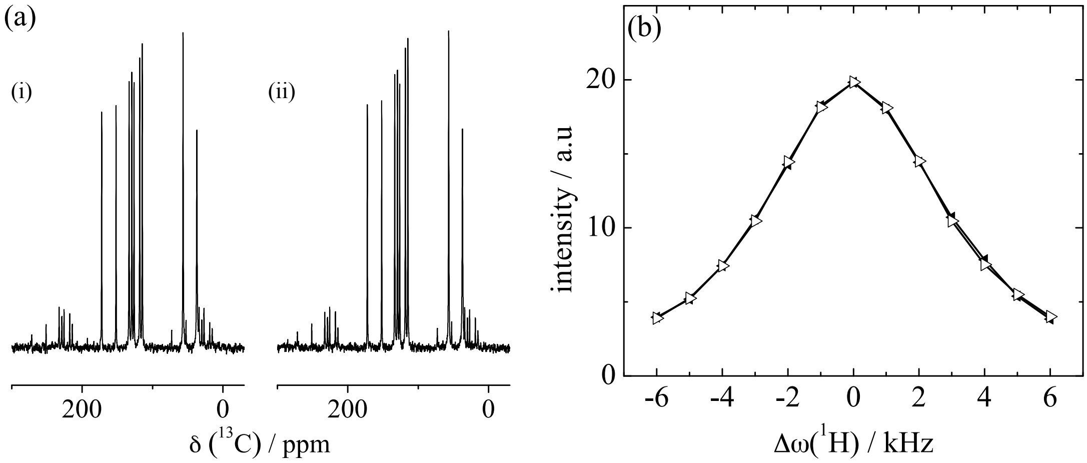

Figure 3.9: (a) Comparison ^{13}C CPMAS spectra of tyrosine acquired with (i) SW$_f$-for-TPPM and (ii) SW$_f$-rev-TPPM decoupling sequences with linear sweep profiles (b) Decoupler offset dependence of SW$_f$-for-TPPM (▷) and SW$_f$-rev-TPPM (◀) decoupling sequences as a function of ^{13}CH$_2$ signal intensities of tyrosine.

The ^{1}H→^{13}C CPMAS spectra of tyrosine, at 10 kHz MAS rate, were acquired on a Bruker AVANCE-II 400 spectrometer with forward and reverse swept SW$_f$-TPPM ^{1}H decoupling. Figure 3.9(a) shows the comparison of such two spectra, which have, for all practical purposes, negligible differences in their respective peak heights and line-widths. The ^{13}C signal intensities of the methylene carbon of tyrosine against the corresponding decoupler (^{1}H) offset is shown in Fig. 3.9(b). It is obvious from Fig. 3.9(b) that the decoupling performance of the sequences with forward and reverse sweeps is equal for the system. These facts suggest that the decoupling efficiency of a frequency swept sequence in solid-state is insensitive to the change in the direction of the sweep [83]. The decoupling performance equivalence is observed in such cases, provided the sequence has an inversion symmetry with respect to the phase angle modulation, so that a perfect reversal of the sequence is possible. The basic pulse-pair block of TPPM is phase-symmetric and therefore, SW$_f$-TPPM pulse duration modulation direction can easily be reversed [83].

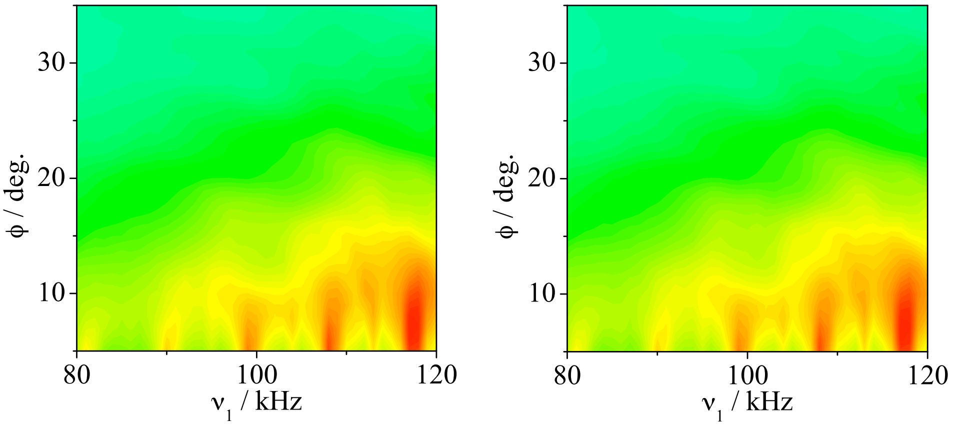

Figure 3.10: Spinevolution numerical simulations of comparison of ^{1}H decoupling efficiencies of SW$_f$-for-TPPM (left) and SW$_f$-rev-TPPM (right) in a system of one ^{13}C dipolar-coupled with four ^{1}Hs. Plotted are the ^{13}C signal intensities as a function of phase angles (ϕ) of the decoupling sequence and the range of *RF* strengths (ν_1).

The equal decoupling performance of the forward and reverse swept TPPM sequences were again confirmed by numerical simulations using Spinevolution program [84]. Again a spin system of one ^{13}C dipolar-coupled with four ^{1}Hs is assumed. The SW$_f$-for-TPPM and SW$_f$-rev-TPPM with linear sweep profiles were checked for their comparative decoupling efficiencies at a MAS frequency of 9.0909 kHz. All the simulations were done with the H–H homonuclear couplings enabled. From Figure 3.10, it is seen that, there is no practical difference between the two methods in the large 2D landscape constructed with phase angles (ϕ) and RF amplitudes (ν_1).

3.4.1 Floquet analysis

A Floquet theoretical treatment for the investigation on the dependence of decoupling efficiency on the sweep direction has been carried out in collaboration with the research group of P. K. Madhu [83]. Most of this treatment describing the efficiency of frequency-sweep has been discussed in Ref. [74] and a short description of it can be found in Section 3.3. For checking the efficiencies of the forward and reverse sweeps, the SW$_f$-TPPM sequence considered is a cyclic one, and the cycle time is τ_c. Therefore, under MAS, there are two time dependencies imposed on the system namely the rotor period (τ_r) and the cycle time (τ_c). Average Hamiltonian theory cannot deal with these two incommensurate time dependencies simultaneously. Bimodal Floquet theory [82] is used to derive the effective Hamiltonian for the system under two time dependencies simultaneously. The SW$_f$-TPPM sequence has a constant amplitude (along y-direction) and modulated phase and pulse duration (along $\pm xz$-plane) irradiation components in the rotating frame. The constant-amplitude component (which is very close to the actual RF amplitude) is chosen to be a constant q times the cycle frequency ν_c. A transformation to the bimodal Floquet space is done by two-step *van Vleck* transformation. As explained in Section 3.3, the resulting effective Hamiltonian has three terms $\hat{\mathscr{H}}_{eff}^{RF}$, $\hat{\mathscr{H}}_{eff}^{(CS-IS)RF}$ and $\hat{\mathscr{H}}_{eff}^{(CS-IS)\pm}$. These three terms can be expressed as [83],

$$\hat{\mathscr{H}}_{eff}^{RF} = \sum_{p} \nu_1 \epsilon_{p,0} I_p - \frac{\nu_1^2}{2} \sum_{p,p',k\neq 0} \frac{\epsilon_{p,k}\epsilon_{p',-k}}{k\nu_c} [I_p, I_{p'}] \tag{3.6}$$

$$\hat{\mathscr{H}}_{eff}^{(CS-IS)RF} = -\frac{1}{2} \sum_{a} \frac{\Delta\nu_a^2}{q\nu_c} I_y - \sum_{a,p,p',k=\pm q} \Delta\nu_a \nu_1 \frac{d_{p,k}\epsilon_{p',-k}}{k\nu_c} [I_p, I_{p'}] \tag{3.7}$$

$$\hat{\mathscr{H}}_{eff}^{(CS-IS)\pm} = -\frac{1}{2}\sum_{a,n\neq 0} \Delta\Omega^{\pm}_{n,a}\Omega^{\pm}_{-n,a}\frac{q\nu_c}{n^2\nu_r^2 - q^2\nu_c^2} I_y \tag{3.8}$$

The third term which contains the I_y component contributes to the line-broadening in the S spin spectrum. While an efficient constant-amplitude component of the decoupling sequence removes the effects from dipolar broadening, the modulating phase and pulse durations reduces the effect from the third term in Eqn. 3.8. Therefore, it is a combination of the y and xz component, which plays a significant role in the efficiency of the decoupling method. A decoupling pulse sequence for such a purpose is defined by the ϵ_k coefficients for the Floquet analysis to assess the decoupling conditions.

The terms which contain the ϵ_k coefficients does not suggest the nature or direction of modulations in pulse duration, but one can calculate the good decoupling conditions from the above-mentioned expressions for different frequency sweeps. If one plots the areas of good decoupling calculated from the Floquet analysis for SW$_f$-TPPM sequences forward and reverse sweeps, their locations are identical [83]. Also, these areas of good decoupling conditions are in very good agreement with the results of numerical simulations, which are shown in a 2D landscape constructed by the RF strengths (ν_1) and phase angles (ϕ) as in Figure 3.10. This shows that the efficiency of SW$_f$-TPPM sequence is independent of the direction of the frequency-sweep [83].

Chapter 4

Frequency-Swept SPINAL

4.1 Introduction

The first heteronuclear dipolar decoupling sequence with frequency sweep introduced was SW$_f$-TPPM, and it was shown to outperform both TPPM and SPINAL by a modest, but consistent margin [72, 78–81]. In addition, an improved robustness to the decoupling parameters like the frequency offsets, pulse durations and phase angles was shown in a variety of systems. Recently, sequences which simultaneously change both phase and pulse durations, SW$_{fp}$-TPPM, have been introduced [78, 85], offering another small improvement in the decoupling efficiency. But here one has to define a second sweep profile for the pulse phases, making the number of parameters to be optimized quite large. A viable alternative is to use a frequency sweep on an already phase-incremented sequence, like SPINAL. In this chapter, an attempt is made to answer the question whether the decoupling performance of the SPINAL sequence may also be improved by incorporating a frequency sweep into it. A systematic exploration of different sweep variants for the so-called SW$_f$-SPINAL [73] sequence by both simulations and experiments is presented. It is found that introducing a sweep generally improves the decoupling performance, irrespective of the sweep type, as evidenced by the experiments in a rigid organic solid system (L-tyrosine) and in a liquid crystalline system (4-*n*-pentyl-4'-cyanobiphenyl or 5CB). The same improvement is found by supporting numerical simulations using the SPINEVOLUTION [84] program.

4.2 Design of Sequences

SW$_f$-TPPM sequences share their basic building block of a pulse pair with alternating phases with TPPM. In most of the demonstrated cases of SW$_f$-TPPM a sequence with 11 pulse pairs was found to have best decoupling performance. The condition for good decoupling may be achieved by adiabatic sweeps in RF field strength (ν_1) or the phase difference (2ϕ) of TPPM blocks. While the SPINAL sequence exploited the modulation of phase difference of TPPM blocks, the SW$_f$-TPPM method took advantage of sweeping the modulation frequency of TPPM basic units. Also, this made both of them less sensitive to NMR parameter changes [74]. This suggests that a combination of the phase difference modulation (as in SPINAL), with a sweep in the pulse durations (as in SW$_f$-TPPM), may be helpful to find a better decoupling sequence. To test whether a frequency sweep improves the decoupling efficiency of SPINAL, several sweep variants were checked, $\underrightarrow{Q}$, $\underrightarrow{Q\bar{Q}}$ etc., where Q is the basic SPINAL unit containing 8 pulses (i.e., 4 pulse pairs; see Section 2.3.3), and $\underrightarrow{XX..}$ indicates the extension of the sweep. The progression of the sequence is schematically shown in Figure 4.1. The RF sweep was implemented by multiplying the SPINAL flip angles with several incremented factors which determine a tangential or a linear profile, from a smaller number less than unity to a bigger number greater than unity in a symmetrical fashion. The resulting sequence in the case of

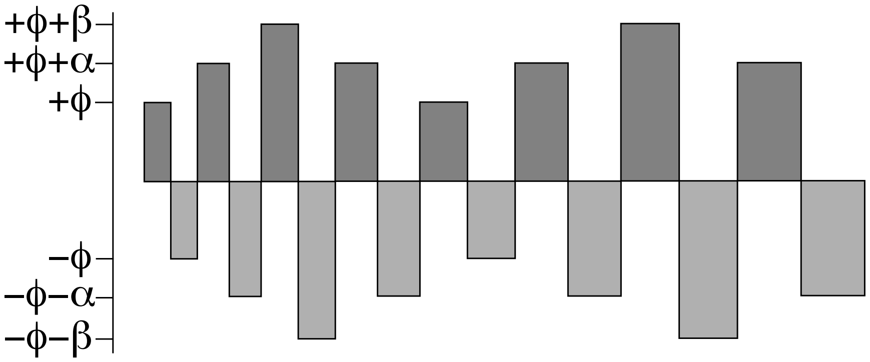

Figure 4.1: The schematic representation of SW$_f$-SPINAL decoupling pulse sequence.

SPINAL-64 may thus have four different forms. The SW$_f$-SPINAL-64 sequence with *RF* sweep over 64 pulses (32 pulse pairs) is represented as $\underrightarrow{Q\bar{Q}\bar{Q}Q\bar{Q}QQ\bar{Q}}$ and it is termed SW$_f$(64)-SPINAL-64. Thus SW$_f$(32)-SPINAL-64 has the form $\underrightarrow{Q\bar{Q}\bar{Q}Q}\underrightarrow{\bar{Q}QQ\bar{Q}}$ and the other two sweep variants are $\underrightarrow{Q\bar{Q}}\underrightarrow{\bar{Q}Q}\underrightarrow{\bar{Q}Q}\underrightarrow{Q\bar{Q}}$ (SW$_f$(16)-SPINAL-64) and $\underrightarrow{Q}\,\underrightarrow{\bar{Q}}\,\underrightarrow{\bar{Q}}\,\underrightarrow{Q}\,\underrightarrow{\bar{Q}}\,\underrightarrow{Q}\,\underrightarrow{Q}\,\underrightarrow{\bar{Q}}$ (SW$_f$(08)-SPINAL-64). Similarly, different block-sweep variants of SW$_f$-SPINAL-32 (16 pulse pairs) and SW$_f$-SPINAL-16 (8 pulse pairs) have been designed. The sequence with 16 pulse pairs, $\underrightarrow{Q\bar{Q}\bar{Q}Q}$ (SW$_f$(32)-SPINAL-32), was found to be the best performing, by both experiments and numerical simulations. It may be noted that the 16 pulse pairs employed in SW$_f$(32)-SPINAL-32 are close to the number of pulse pairs found best for SW$_f$-TPPM, creating a similar cycle time τ_c. Good decoupling performance was also achieved experimentally with the $\underrightarrow{\bar{Q}QQ\bar{Q}}$ inverse sequence, even though numerical simulations did show the $\underrightarrow{Q\bar{Q}\bar{Q}Q}$ sequence to be superior. The SW$_f$-SPINAL sequences with 64, 32, 16 and 8 pulses, all perform better than the original SPINAL-64. This clearly demonstrates that also the SPINAL sequence with its complex phase pattern benefits from the introduction of a sweep [73].

4.3 Applications

The efficiency of the SW$_f$-SPINAL decoupling sequences was checked for rigid solids and liquid crystal experimentally. The ^{13}C Cross Polarization Magic Angle Spinning (CPMAS) spectra of natural abundance tyrosine hydrochloride (Sigma Aldrich) were acquired on a Bruker AVANCE-II 400 spectrometer, at a Larmor frequency of $\nu_0(^{13}\mathrm{C})= 100.58$ MHz, using a 4 mm MAS triple channel probe at different spinning frequencies (8, 10, 12 and 14 kHz), with a contact time of 2 ms. Using a recycle delay of 4 s, 128 transients were accumulated for each spectrum. The ^{13}C CP experiments on the liquid crystalline system 5CB (Sigma Aldrich) were done on the same spectrometer with a 7 mm double resonance static probe with a cross-polarization time of 5 ms. A recycle delay of 10 s was used at a temperature of 28° C, to maintain a low duty cycle, to avoid deleterious effects on ^{13}C spectra caused by *RF* heating [86]. The tested decoupling sequences were implemented using the standard Bruker CPD format. The decoupling profile parameters were optimized for the different sequences, in the same way as described in Chapter 3. The optimization of sweep profiles for SW$_f$-SPINAL is done in a similar way to that of SW$_f$-TPPM [78, 81]. The sweep profiles with sixteen different sweep widths (and hence different slopes) were tested for both the linearly and tangentially varied SW$_f$-SPINAL sequences to find the best performance. In addition, for the tangent profiles, the tangent cut-off angle was optimized for each set of measurements, since this angle determines the curvature of the sweep profile. The tangent cut-off angle appeared to be close to 60° in most of the cases, similar to SW$_f$-TPPM [81], in both the samples. In all the cases, the linear version performed as good as or sometimes even better than the tangent ones. For comparisons in this section, we present the linear versions only. In all the above-mentioned cases a small sweep window was favorable with SW$_f$-SPINAL sequences. Since the SW$_f^{lin}$(32)-SPINAL-32 decoupling method was found to be the most efficient, among the SW$_f$-SPINAL group, its performance will be compared to SW$_f$-TPPM and SPINAL-64 in the case of rigid solids and liquid crystals in more detail.

4.3.1 Rigid Solids

L-tyrosine hydrochloride is a suitable standard system as a rigid solid for comparative studies of the SW$_f$-SPINAL sequence, as it has been used in the demonstration of both SPINAL-64 and SW$_f$-TPPM in the original works [58, 72]. In Figure 4.2(a), the experimental decoupling efficiency of SW$_f$-SPINAL sequences with a total sequence length of 64, 32, 16 and 8 pulses and a single forward sweep comprising all pulses are compared for off-resonance robustness. It can be seen that the performance of all these sequences is very similar, except for the SW$_f$(32)-SPINAL-32 sequence, which shows improved characteristics. The effects of shortening the extent of the frequency sweeps within the SW$_f$-SPINAL sequence were also explored. As can be seen from Figure 4.2(b), the decoupling performance deteriorates when going from SW$_f$(64)- to SW$_f$(32)-, SW$_f$(16)- and SW$_f$(08)-SPINAL-64. A similar deterioration effect was observed when shortening the sweeps within the SW$_f$-SPINAL-32 and SW$_f$-SPINAL-16 sequences.

The decoupling efficiency of the new SW$_f$-SPINAL sequence is compared to previously reported methods in Figure 4.3. Using L-tyrosine as a model compound

Table 1. NMR parameters governing decoupling optimized from ^{13}C CPMAS experiments done on L-tyrosine hydrochloride. Listed are the pulse durations (τ_p), phase angle (ϕ), number of pulse-pairs (N), the sweep window (W) and the tangent cut-off angle (θ). A decoupling RF field strength of 81 kHz was used in each experiment.

MAS	Parameter	SW$_f^{lin}$-TPPM	SW$_f^{tan}$-TPPM	SW$_f^{lin}$-SPINAL	SW$_f^{tan}$-SPINAL
8 kHz	τ_p/μs	6.00	6.00	5.75	5.75
	ϕ	±7.5°	±7.5°	±6.25°	±6.25°
	N	11	11	16	16
	W	0.60-1.40	0.54-1.46	0.93-1.07	0.93-1.07
	θ	–	50°	–	50°
10 kHz	τ_p/μs	5.25	5.25	5.50	5.50
	ϕ	±7.5°	±7.5°	±6.25°	±6.25°
	N	11	11	16	16
	W	0.69-1.31	0.60-1.40	0.90-1.10	0.90-1.10
	θ	–	60°	–	60°
12 kHz	τ_p/μs	5.50	5.50	5.75	5.75
	ϕ	±7.5°	±7.5°	±6.25°	±6.25°
	N	11	11	16	16
	W	0.66-1.34	0.57-1.43	0.69-1.31	0.60-1.40
	θ	–	60°	–	55°
14 kHz	τ_p/μs	5.25	5.25	5.50	5.50
	ϕ	±7.5°	±7.5°	±6.25°	±6.25°
	N	11	11	16	16
	W	0.63-1.37	0.60-1.40	0.93-1.07	0.90-1.10
	θ	–	55°	–	65°

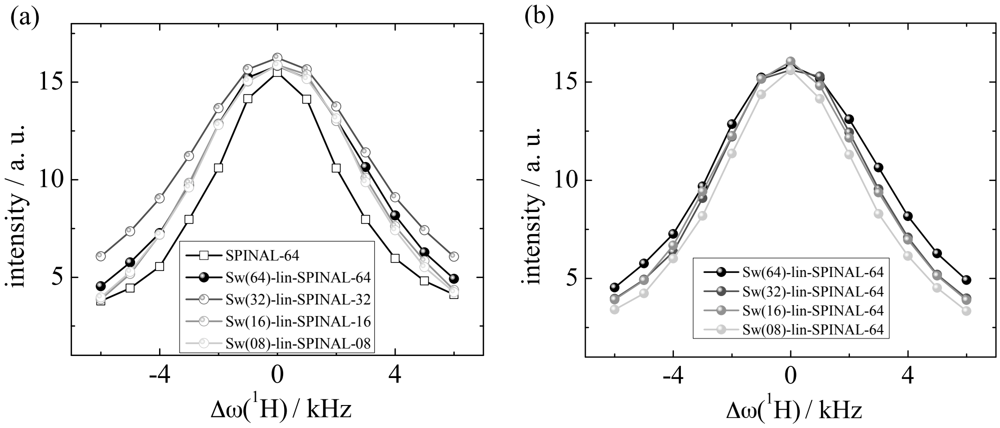

Figure 4.2: ^{1}H off-resonance effects for the ^{13}C resonance from the methylene group of L-tyrosine hydrochloride molecule obtained with several SW$_f$-SPINAL decoupling methods with (a) different SPINAL basic units and (b) with different SPINAL-64 sweep units obtained from its ^{13}C CPMAS spectrum at 10 kHz MAS frequency.

(Fig. 4.3(a)), the intensity of the CH$_2$ resonance in the ^{13}C CPMAS spectrum (Fig. 4.3(b)) is analyzed for application of different decoupling sequences. Five different decoupling methods are compared in Figure 4.3(c) and 4.3(d), namely SPINAL-64, SW$_f^{lin}$(32)-SPINAL-32, SW$_f^{tan}$(32)-SPINAL-32, SW$_f^{lin}$-TPPM and SW$_f^{tan}$-TPPM, tested at four different spinning speeds. The NMR parameters which determined the decoupling profiles for all different MAS frequencies used are listed in Table 1. The absolute intensities of the CH$_2$ resonance is plotted as a function of the decoupler frequency offset up to ±6 kHz in Figure 4.3(c). The performance of SW$_f$-TPPM with decoupling was always found best at 'on-resonance' conditions, even though sometimes by a very narrow margin. Nevertheless, the SW$_f$-SPINAL methods perform equally well at 8 kHz, the lowest spinning speed employed, even at zero-offset and at far-offsets, as shown in Figure 4.3(c). Over the entire offset range, SW$_f$-SPINAL was always found to be more efficient than SPINAL-64 or TPPM. (Due to its performance being well below that of SPINAL-64, the TPPM results have not been plotted in Fig. 4.3.) Both the linear and the tangent versions of SW$_f$-SPINAL were equally good in decoupling efficiency. But the 'on-resonance' performance of SW$_f$-SPINAL drops with the increase of MAS

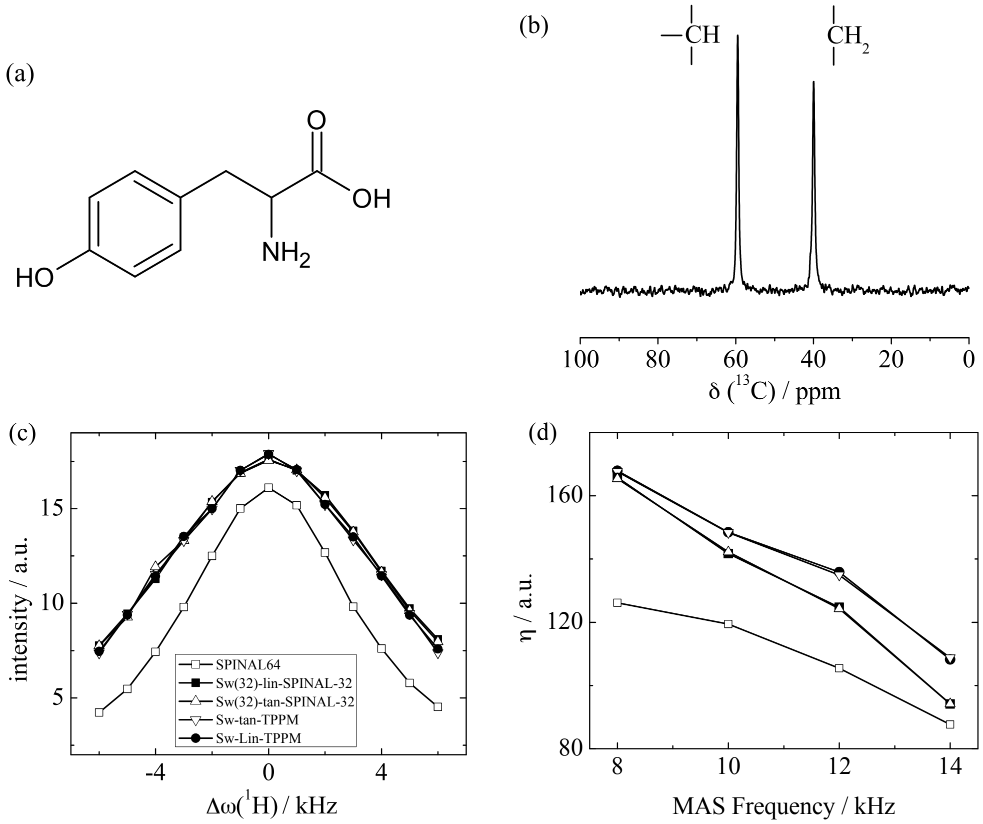

Figure 4.3: (a) The L-tyrosine hydrochloride molecule and (b) its ^{13}C CPMAS spectrum of the aliphatic region. The ^{1}H off-resonance effects were studied for all the ^{13}C resonances for a range of MAS spinning frequencies and that of (c) the methylene carbon at 8 kHz MAS is shown along with (d) the MAS frequency dependence of the ^{13}C signal intensity. A figure-of-merit parameter η is introduced here, with $\eta = I_{0kHz} + I_{2kHz} + I_{4kHz} + I_{6kHz}$, where I_{xkHz} is the absolute intensity of the CH$_2$ signal at x kHz ^{1}H offset.

frequency, as can be seen from Figure 4.3(d), when compared to SW$_f$-TPPM, but not beyond that of SPINAL-64 [73]. A good robust decoupling condition is achieved, usually, with a radio-frequency sweep, if the cycle time τ_c is shorter than the rotor period τ_r [78]. This is what makes the SW$_f$-TPPM sequences with 11 pulse pairs comparably inefficient at high MAS frequencies [78]. In the case of SW$_f$-SPINAL, the decoupling performance falls much more drastically, as the 16 pulse pairs constitute a larger τ_c than that of SW$_f$-TPPM.

4.3.2 Liquid Crystals

Highly efficient dipolar decoupling is also an important requirement in ^{13}C NMR studies of oriented media like membrane proteins and liquid crystalline systems [87, 88]. The demands for decoupling differ from those needed for rigid crystalline solids, as in the LC phase the dipolar interactions are scaled down by anisotropic thermal motions of the molecules. When 4-n-pentyl-4'-cyanobiphenyl (5CB) used as a model compound in the original SPINAL-64 publication [58], one of the main drawbacks shown was the severe sensitivity to the decoupler offset, especially in the aliphatic signals of the molecule [58]. In Figure 4.4(b), from the ^{13}C spectrum of the aliphatic region of 5CB, ^{1}H decoupled with SW$_f^{lin}$(32)-SPINAL-32, it can be seen clearly that all the five signals possess almost comparable intensities. This proves the high robustness of the frequency-swept SPINAL method towards ^{1}H offsets. In order to check the performance of different decoupling sequences in detail, deliberate ^{1}H offset changes were made in the range of ±6 kHz. Different spin systems in the aliphatic region responded to it in different ways. As shown in Figure 4.4(c), the expected Lorentzian curve [77] for the offset dependence was only obtained for the most rigid α-carbon, attached to the biphenyl moiety. From the rigid part to the more mobile part, i.e., from α-carbon to the δ-carbon, there is a decrease in sensitivity towards ^{1}H offset changes, attributable to the increasing mobility of the C-atoms in the chain. Thus the flattening of the offset dependence curve has its maximum with the δ-carbon, which therefore is less informative with respect to the decoupling performance, than the behavior of the signals belonging to the γ-carbon as shown in Figure 4.4(d). In comparison, the phenyl carbon intensities and the methyl group are not much affected with different parameter offsets and we therefore restrict the discussion to the aliphatic methylene groups [73].

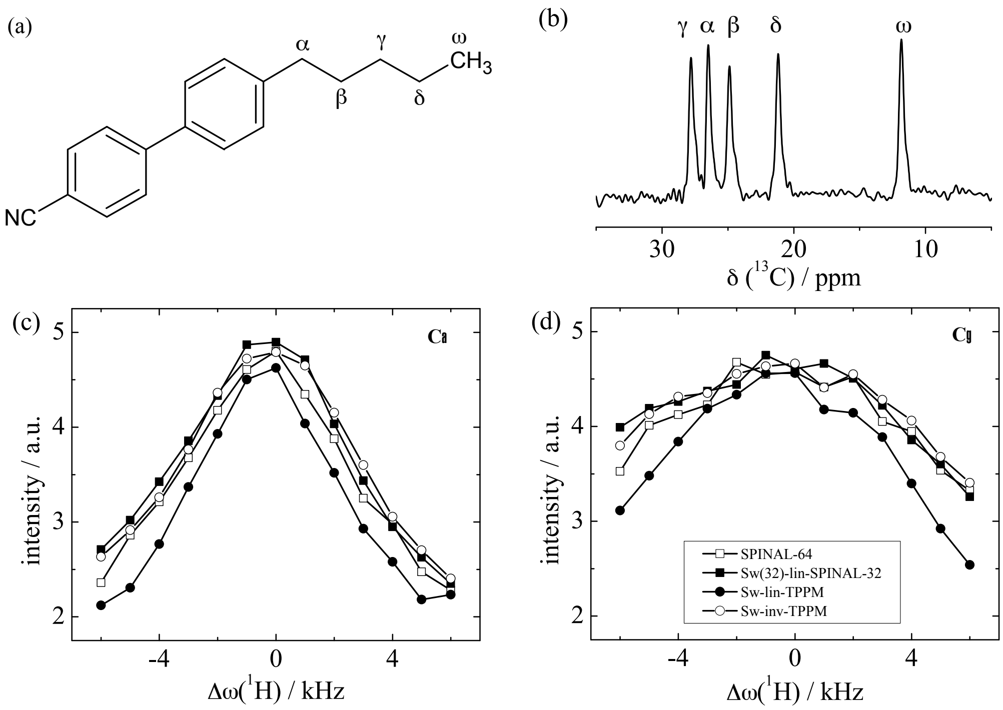

Figure 4.4: (a) The 4-n-pentyl-4'-cyanobiphenyl (5CB) molecule and (b) its ^{13}C static CP spectrum of the aliphatic region. The ^{1}H off-resonance effects were studied for all the ^{13}C resonances and those of (c) α-carbon and (d) γ-carbon are shown.

The parameters governing different decoupling sequences had to be optimized, before starting comparing the relative performance of them. The original TPPM sequence [57], even with the best optimized pulse duration τ_p (10.5 μs) and phase angle ϕ (7.5°) was the least efficient in decoupling and has been kept out from the comparison plots. The parameters for all decoupling methods, which are compared in Figure 4.4(c) and 4.4(d), are listed in Table 2. A low power decoupling of RF field strength of 42 kHz was used in each experiment, since RF heating of the liquid crystal sample needs to be avoided [86]. The sample temperature was thus held constant at 28° C, in the nematic phase, while the crystalline phase was well below 24.0° C and the isotropic phase existed only above 35.3° C.

Table 2. NMR parameters governing decoupling optimized from ^{13}C static CP experiments done on 4-n-pentyl-4'-cyanobiphenyl (5CB). Listed are the pulse durations (τ_p), phase angle (ϕ), number of pulse-pairs (N) and the sweep window (W). A decoupling RF field strength of 42 kHz was used in each experiment.

Parameter	SW$_f^{lin}$-TPPM	SW$_f^{inv}$-TPPM	SW$_f^{lin}$-SPINAL
τ_p/μs	11.5	11.5	11.0
ϕ	±7.5°	±7.5°	±12.5°
N	11	11	16
W	0.81 − 1.19	0.67 − 2.00	0.90 − 1.10

SW$_f$-SPINAL proved to be superior to the original SPINAL-64 sequence with different 5CB aliphatic signals at 'on-resonance' and 'off-resonance' conditions, as can be seen from Figure 4.4(c) and 4.4(d). The linear as well as the tangential versions were not exactly equally efficient, the linear profile being shown in the figures as it was performing slightly better. The decoupling efficiency of SW$_f$-TPPM, especially with tangent sweep profile was found to be worse than the other methods. The performance of linearly swept SW$_f$-TPPM is shown in Figures 4.4(c) and 4.4(d) and the comparatively low decoupling efficiency of it is obvious here. However, the sweep profile of SW$_f$-TPPM may be adapted to give better decoupling for liquid crystalline systems. It has been demonstrated by Madhu and coworkers that the so-called *inverse* sweeping profile (SW$_f^{inv}$-TPPM) [80] leads to efficient decoupling for the MBBA liquid crystal. Similarly for 5CB, the SW$_f^{inv}$-TPPM sequence gives very good decoupling performance, like SW$_f$-SPINAL. Both these new sequences clearly outperform the original SPINAL-64 decoupling, especially at far offsets [73]. The experimental results show that SW$_f$-SPINAL is one of the best sequences currently available for spin decoupling in oriented media (like liquid crystals and biological membranes).

4.4 Numerical Simulations

For testing the decoupling performance for a rigid organic solid numerically, the different SW$_f$-SPINAL and SW$_f$-TPPM sequences were tested with SPINEVOLUTION [84] simulations. The model spin system was a ^{13}C, dipolar-coupled with four protons arranged in a glycinyl structural backbone. The results are displayed as the absolute intensities of the ^{13}C resonance as a function of the *RF* amplitude (ν_1) and phase angle (ϕ). 5μs pulse duration was chosen for all the simulations. The sequences with TPPM basic blocks were simulated at a MAS frequency of 9.0909 kHz, while the ones with SPINAL basic blocks were simulated at 8.3333 kHz MAS frequency, in order to speed up computation by avoiding interference effects with the decoupling sequence cycle. The *RF* amplitude ν_1 was varied from 80 to 120 kHz in steps of 1 kHz while the phase angle ϕ was scanned from

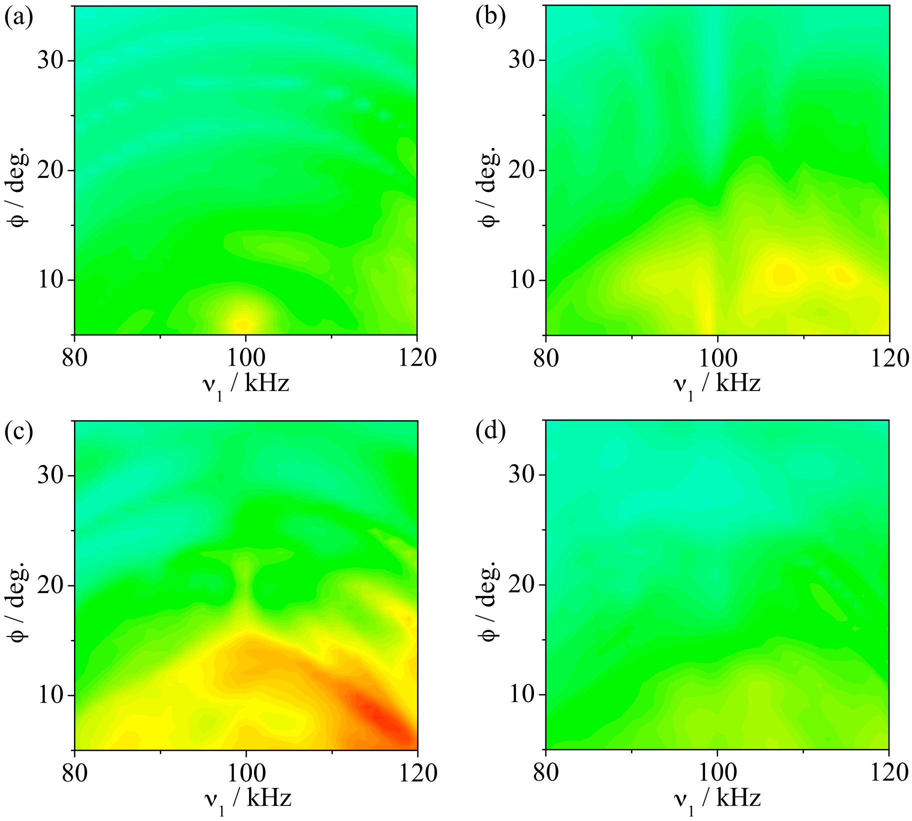

Figure 4.5: The results of SPINEVOLUTION [84] simulations (a) SW$_f^{lin}$(08)-SPINAL-08 (b) SW$_f^{lin}$(16)-SPINAL-16 (c) SW$_f^{lin}$(32)-SPINAL-32 and (d) SW$_f^{lin}$(64)-SPINAL-64, being plotted as the absolute intensity of the ^{13}C resonance as a function of *RF* strength ν_1 and the phase angle ϕ. A four-proton system dipolar-coupled with ^{13}C was assumed for the simulations, and a MAS frequency of 8.3333 kHz was used.

5° to 35° in 1° step width. The values for the phase settings were identical for SW$_f$-TPPM, with additional phase increments $\alpha = 5°$ and $\beta = 10°$ included for SW$_f$-SPINAL. A line broadening factor of 5 Hz was used for all calculations.

The different SW$_f$-SPINAL variants were checked numerically to find the most efficient sequence. Increasing the number of sweep-blocks within the SW$_f$-SPINAL-64 sequence leads however to a performance drop. The same effect happens with the SW$_f$-SPINAL-32 and SW$_f$-SPINAL-16 sequences. Therefore, in the Figure 4.5, only the efficient four SW$_f$-SPINAL sequences are shown, namely SW$_f^{lin}$(08)-SPINAL-08, SW$_f^{lin}$(16)-SPINAL-16, SW$_f^{lin}$(32)-SPINAL-32 and SW$_f^{lin}$(64)-SPINAL-64. It is thus found that the linearly-swept sequence with 16 pulse pairs, $\underrightarrow{Q\bar{Q}\bar{Q}Q}$ (SW$_f^{lin}$(32)-SPINAL-32), to be the best performing overall, by numerical simulations (Figure 4.5(c)).

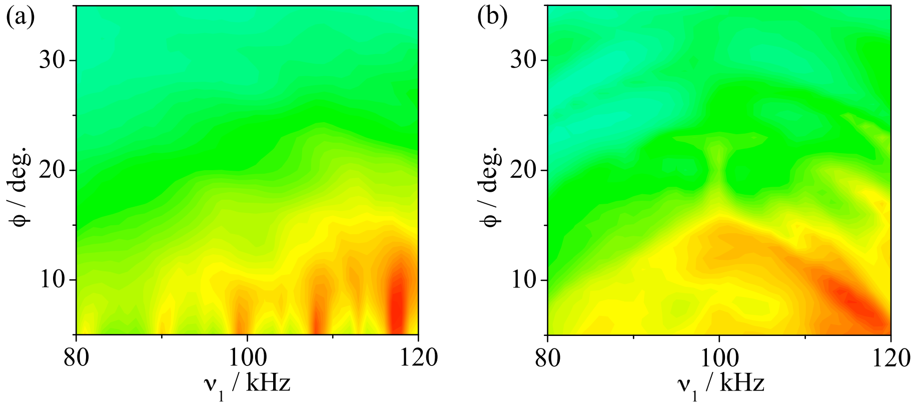

Figure 4.6: The results of SPINEVOLUTION [84] simulations of (a) SW$_f^{lin}$-TPPM and (b) SW$_f^{lin}$(32)-SPINAL-32, being plotted as the absolute intensity of the ^{13}C resonance as a function of RF strength ν_1 and the phase angle ϕ. A four-proton system dipolar-coupled with ^{13}C was assumed for the simulations, where a MAS frequency of 8.3333 kHz was used for SW$_f$-SPINAL and 9.0909 kHz for SW$_f$-TPPM.

In the plots shown in Figure 4.6(a), and 4.6(b), efficient decoupling is present in the areas of high intensity. In the case of SW$_f$-TPPM, a vertical band of high intensity which corresponds to the first condition of decoupling is clearly seen and this periodically repeats (Figure 4.6(a)). The periodic positions of these bands are influenced by the cycle time and the MAS frequency. In between the repeating periodic bands, there are areas of low intensity, at a particular combination of *RF* field strength and phase angle, which are the corresponding inefficient decoupling conditions. In the case of SW$_f$-SPINAL, repeating bands are hardly visible, but a spread of moderately good decoupling condition is seen, especially in the low power region, without the appearance of the periodic troughs. As shown in Figure 3.7, the SPINAL-64 sequence is found to have a very small area of good decoupling condition in comparison with SW$_f$-TPPM, which will be difficult to find by optimization. Doubling the MAS frequency for simulations gave similar results with low intensities, as τ_r is halved when the cycle time τ_c remains constant. Thus also in numerical simulations, the implementation of *RF* sweep in the SPINAL sequence is observed to be having an advantageous effect on decoupling efficiency and robustness [73].

Chapter 5

^{19}F Decoupling

5.1 Introduction

The necessity for efficient decoupling of ^{19}F occurs frequently in solid-state NMR, as fluorine is present in many important materials like polymers, ion conductors, minerals and ceramics. Consequently, a large number of examples may be found in the literature where a rare spin has been observed under ^{19}F decoupling [89–109]. Whereas in many cases, only CW decoupling has been used [89–100], there is also evidence of application of multi-pulse techniques. In analogy to the results obtained for ^{1}H, it was attempted to improve spectral resolution by decoupling ^{19}F using TPPM [101–105], SPINAL [106, 107] and also XiX [108, 109]. But there were no reports on a systematic comparison of the respective performances of different ^{19}F-decoupling techniques. In this chapter, we discuss a systematic comparison of ^{19}F-decoupling efficiencies of different composite pulse decoupling sequences performed in rigid perfluoro-organic systems, with special emphasis given to the new frequency-swept sequences [110].

^{19}F-decoupling in solid-state is considered to be a non-trivial exercise, when compared to ^{1}H-decoupling. The reason of ^{19}F-decoupling being difficult arises from additional shielding effects of *s*- and *p*-electrons in fluorine. These effects basically broaden the *dispersion of isotropic chemical shifts* ($d\delta_{iso}$) and *chemical shift anisotropy* (CSA) of ^{19}F to a large extent leading to large line broadening of the ^{19}F (abundant spin) NMR signal. For a sample with a spread of isotropic chemical shifts for the abundant nuclei, *on-resonance* conditions cannot be met simultaneously. In principle, the chemical shift anisotropy (CSA) may be averaged out by MAS, if the spinning speed exceeds the magnitude of the CSA interaction. For ^{1}H, both $d\delta_{iso}$ and $\Delta\delta$ (the parameter which gauges CSA; see Section 1.2.3) are comparatively small, namely up to tens of *ppm*. The situation is different for the nucleus ^{19}F, which is otherwise - in terms of NMR response - very similar to ^{1}H: ^{19}F possesses spin $I = 1/2$, a natural abundance of 100%, and a gyromagnetic ratio close to that of ^{1}H. But even when placed in a similar chemical environment, the chemical shift effects experienced by ^{19}F are much larger than those of ^{1}H, due to a larger electron cloud. As may be seen from Table 1, the dispersion of ^{19}F isotropic shifts $d\delta_{iso}$ tends to be much larger than that of protons, whereas the magnitude of $\Delta\delta$ of ^{19}F may reach hundreds of *ppm*. Under MAS conditions, $d\delta_{iso}$ will be not affected at all, whereas for slow to moderate spinning speeds, $\Delta\delta$ will not be averaged completely. The cross-term between CSA and heteronuclear dipolar interaction (see Section 2.4.2) is also larger for ^{19}F as compared to ^{1}H. This adds to the challenge of performing efficient spin decoupling for ^{19}F nuclei, and raises the question of how spin decoupling techniques, usually designed and tested for ^{1}H decoupling, perform when applied to ^{19}F.

This chapter describes ^{19}F decoupling efficiencies of different decoupling methods which have been discussed in previous chapters 3 and 4. TPPM, SPINAL, SW$_f$-TPPM and SW$_f$-SPINAL are the methods which are being compared, in decoupling experiments conducted on potassium nonafluoro-1-butanesulfonate (NFBS-K) and sodium pentafluoropropionate (PFP-Na). These model compounds may be classified as rigid organic solids on the NMR time scale. Also, the rare spin ^{13}C is observed in the presence of ^{19}F only. Another experimentally important situation is the simultaneous presence of ^{1}H and ^{19}F. For isolated (or very dilute) HXF pairs, offset-robust decoupling on ^{1}H only may be sufficient for good resolution [111]. For systems that are abundant in both ^{1}H and ^{19}F, however, triple resonance experiments need to be performed in order to decouple both nuclides [112–119]. ^{19}F decoupling on polymers were also not investigated in this work, as these are conceptually different from rigid organic solids, and are known to respond differently to *RF* decoupling [131]. SPINEVOLUTION [84] numerical simulations were done to evaluate the performance of the various ^{19}F

Table 3. The isotropic chemical shift (δ_{iso}=$\frac{1}{3}$[δ_{11}+δ_{22}+δ_{33}]) and the chemical shift anisotropy CSA ($\Delta\delta$=δ_{33}−δ_{iso}) at the condition, $|\delta_{33}-\delta_{iso}| \geq |\delta_{22}-\delta_{iso}| \geq |\delta_{11}-\delta_{iso}|$) values of ^{1}H and ^{19}F nuclei in similar chemical environments. The acquisition temperatures (T) and the corresponding references from which the data have been taken are also listed.

^{1}H				^{19}F			
Compound	δ_{iso} / ppm	$\Delta\delta$ / ppm	Ref.	Compound	δ_{iso} / ppm	$\Delta\delta$ / ppm	Ref.
$CHCl_3$	24	8.6	[120][a]	$CFCl_3$	190	51	[121][a]
NH_3	31.2	15.61	[122, 123]	NF_3	74.9	390.0	[124, 125][b]
C_6H_6	7	-5.3	[126]	C_6F_6	0.33	149.5	[127]
TBB[c]	-	-6.95	[128]	TFTBB[d]	81.0	-112.0	[128]
DFBP[e]	-6.5, -7.5	5.0, 2.0	[129]		-52.5	51.77	[129]
DCFP[f]	7.04	4.45	[130]		-127.02	87.86	[130]

a – determined from solution in liquid-crystalline media.

b – determined from molecules trapped in clatherates.

c – 1,3,5-tribromobenzene

d – 1,3,5-trifluorotribromobenzene

e – 4,4’-difluorobiphenyl

f – 2,6-dichloro 4-fluorophenol

decoupling schemes. Both in experiment and in simulation, the frequency-swept sequences always outperformed TPPM and SPINAL by a consistent margin, with an enhanced robustness towards parameter changes [110].

5.1.1 Experimental details

Potassium nonafluoro-1-butanesulfonate (NFBS-K, Sigma Aldrich) and sodium pentafluoropropionate (PFP-Na, Acros Organics) were purchased and used without further purification. The ^{19}F spectrum of NFBS-K in D_2O solution was recorded on a Bruker AVANCE-II 400 spectrometer. It showed multiplet structures centered at 81.42 ppm for the CF_3 group (δ-carbon), and for the CF_2 groups at 115.17 (α), 122.40 (γ), and 126.52 ppm(β). The $^{19}\text{F}\rightarrow{}^{13}\text{C}$ Cross Polarization Magic Angle Spinning (CPMAS) spectra of NFBS-K and PFP-Na were acquired on a Bruker AVANCE-II 400 spectrometer, at a ^{13}C Larmor frequency of 100.58 MHz and a ^{19}F Larmor frequency of 376.13 MHz, using a 2.5 mm double channel MAS probe at different spinning frequencies (10, 15, and 20 kHz). A CP contact time of 5 ms was used for both model compounds with a recycle delay of 5 s for PFP-Na and 7 s for NFBS-K, with 128 transients collected for each spectrum. All decoupling sequences used were coded in the standard Bruker CPD format. The parameters governing the decoupling sequences were optimized by sequentially changing pulse durations, phase angles and sweep profiles while searching for the maximum intensity of the ^{13}C signal. Optimization procedure of the sequences is explained in Sections 3.2.2 and 4.3. Since the linear and the tangential sweep profiles produced similar decoupling efficiency, only results from the linear profiles are shown in the comparison plots. All the experiments were done at a decoupling field strength of 120 kHz.

The performance of the various decoupling schemes was also investigated by Spinevolution [84] numerical simulations. The spin system under analysis for simulations was a ^{13}C nucleus dipolar-coupled with four ^{19}F nuclei, arranged in a glycinyl backbone structure. All the calculations were run with the ^{19}F–^{19}F homonuclear dipolar interaction enabled and with a range of ^{19}F chemical shielding anisotropies. A line broadening factor of 5 Hz was used for all calculations. MAS frequencies for the simulations of sequences with TPPM and SPINAL basic blocks, were chosen to be 8.0808 kHz and 8.3333 kHz. This helped to avoid interference effects of the cycle time of the decoupling sequence. A matrix of RF strength ν_1 and phase angle ϕ was scanned for each simulation, where ν_1 varies from 80 to 120 kHz in steps of 1 kHz, and ϕ changed from 0° to 30° in 1° step width. The values for the phase settings were identical for TPPM and SW$_f$-TPPM, but for SPINAL and SW$_f$-SPINAL phase increments of $\alpha = 5°$ and $\beta = 10°$ were included.

For ^{19}F decoupling of PFP-Na, the best performing phase angles (ϕ) for TPPM, SW$_f$-TPPM and SW$_f$-SPINAL were found to be 12.5°, but 15° for SPINAL-64. In the case of NFBS-K, the TPPM phase angle was optimized to be 7.5° and for SPINAL-64, SW$_f$-TPPM and SW$_f$-SPINAL, it was 12.5°. For SW$_f$-SPINAL, the sequence SW$_f^{lin}$(32)-SPINAL-32 [73], with a single linear sweep over 32 SPINAL pulses from 0.90 to 1.10 was found to be superior in decoupling of NFBS-K, whereas SW$_f^{lin}$(64)-SPINAL-64 with the identical sweep window (0.90-1.10) proved best for decoupling of PFP-Na. The best sweep for SW$_f$-TPPM was found to be from 0.78 to 1.22 in the case of PFP-Na and from 0.69 to 1.31 for NFBS-K, all with linear sweep profiles. In all the cases, the flip angles (pulse durations) were optimized experimentally.

5.2 Decoupling in Rigid Solids

PFP-Na (Figure 5.1, top row) and NFBS-K (Figure 5.1, bottom row) were used to study the decoupling performance of different decoupling methods. In particular, NFBS-K, with four fluorinated carbon groups, and an isotropic ^{19}F shift dispersion of $d\delta_{iso} \approx 45$ ppm appears to be a good candidate for testing decoupling efficiency. As shown in Figure 5.1, the frequency-swept TPPM and SPINAL sequences outperform the non-swept sequences by a considerable margin for both samples. PFP-Na shows three resolved carbon resonances, the most de-shielded one being the carbonyl carbon. Since the effect of decoupling on the carbonyl signal intensities is weak, only the difluoromethylene (CF$_2$) and trifluoromethyl (CF$_3$) carbon signals of PFP-Na are evaluated in the ^{19}F-decoupled ^{13}C CPMAS spectrum. NFBS-K has four different carbon resonances with the α-carbon (115.3 ppm) being the most shielded once, since it is closest to the sulfonate group. Following are the carbon signals of the CF_3 (δ-carbon, 112.5 ppm) and remaining CF_2's (β at 112.5 ppm and γ at 107.1 ppm). The quality of ^{19}F decoupling can be judged from the intensity and the separation of the carbon lines in Figure 5.1, with SW$_f$-TPPM and SW$_f$-SPINAL delivering best intensities and concomitant resolution [110].

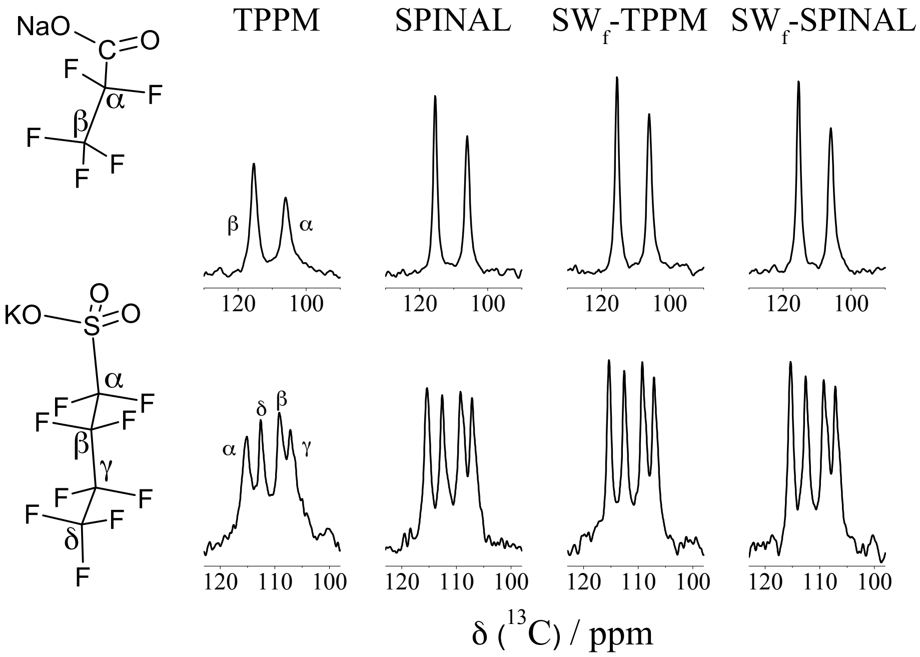

Figure 5.1: ^{19}F decoupled ^{13}C CPMAS spectra of (top row) CF_2 and CF_3 groups of sodium pentafluoropropionate (PFP-Na) and (bottom row) potassium nonafluoro-1-butanesulfonate (NFBS-K). Decoupling performance of TPPM, SPINAL, SW$_f$-TPPM and SW$_f$-SPINAL are compared for both model compounds. All the spectra were collected at an MAS frequency of 10 kHz, with the decoupler frequency being *on-resonance*.

The ^{19}F *off-resonance* effects on decoupling performance are shown in Figure 5.2. Here, the decoupler frequency was deliberately moved away from the position judged to best represent *on-resonance*. (A good criterion for *on-resonance* condition is to take the maximum of the intensity curve displayed by ^{13}C on changing the ^{19}F frequency [77].) The *off-resonance* effects were more prominent in NFBS-K than in PFP-Na, and therefore the former is used here-onwards for the discussion. The comparison of decoupling efficiencies of the various methods was done through the analysis of ^{13}C intensities of the CF_2 and CF_3 resonances of NFBS-K. In Figure 5.2, the response of the different carbon atoms in NFBS-K to changing the ^{19}F frequency offset by ±12 kHz is shown. Plotted are the data for the three CF_2 carbons (α, β and γ) and the CF_3 carbon (δ), acquired at 10 kHz MAS frequency. It can be seen from Figure 5.2 that small offset changes do

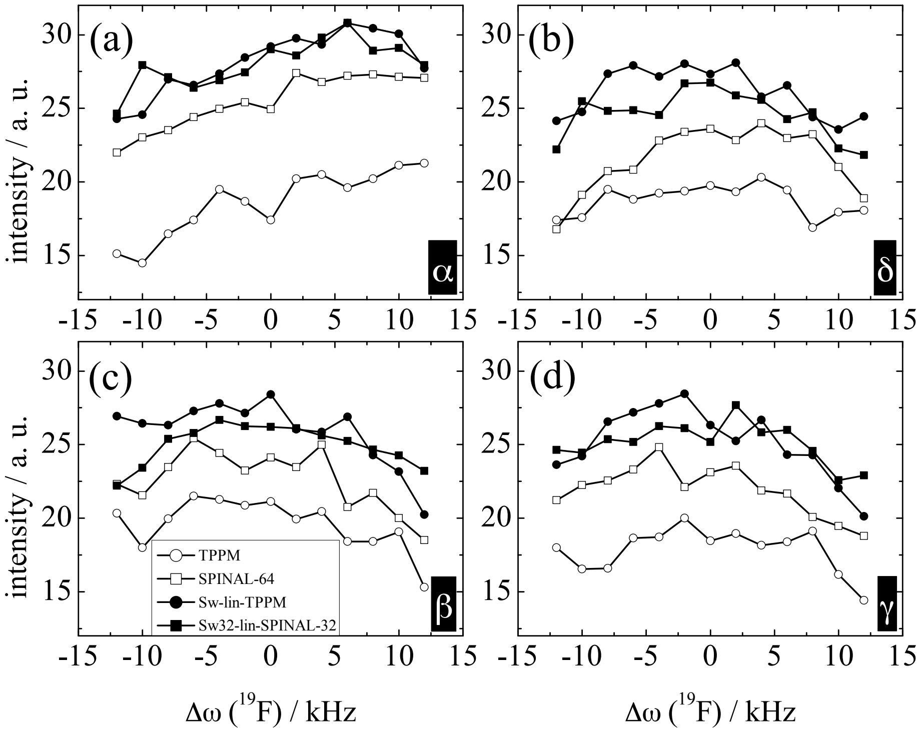

Figure 5.2: The ^{19}F *off-resonance* effects are shown for the ^{13}C CPMAS spectra of NFBS-K for the signals from (a) α, (b) δ, (c) β and (d) γ-carbons. Decoupling performance of TPPM, SPINAL, SW_f-TPPM and SW_f-SPINAL are compared based on the ^{19}F offset dependence at a MAS frequency of 10 kHz.

not have much effect, probably due to the large ^{19}F shielding anisotropy and the presence of homonuclear couplings. For all data, the frequency-swept sequences outperform SPINAL and TPPM by a consistent margin [110].

The dependence of decoupling efficiency as a function of MAS frequency was also explored. The results are shown in Figure 5.3 for all four ^{13}C signals of NFBS-K under *on-resonance* conditions. Here, the full-widths at half-maximum of the ^{13}C lines are plotted, instead of the intensities used in all other plots.

This was done to exclude possible variations of cross-polarization efficiency with changed MAS, which would affect the intensities. The parameters of the decoupling sequences were optimized at 10 kHz MAS and then kept unchanged for the higher MAS frequencies. It can be seen from Figure 5.3 that SW$_f$-TPPM and SW$_f$-SPINAL sequences outperform TPPM and SPINAL over all the spinning frequencies analyzed, for the (a) α, (b) δ, (c) β and (d) γ-carbons [110]. The relation between MAS frequency and decoupling efficiency will be discussed in more detail below, in the context of numerical simulation results.

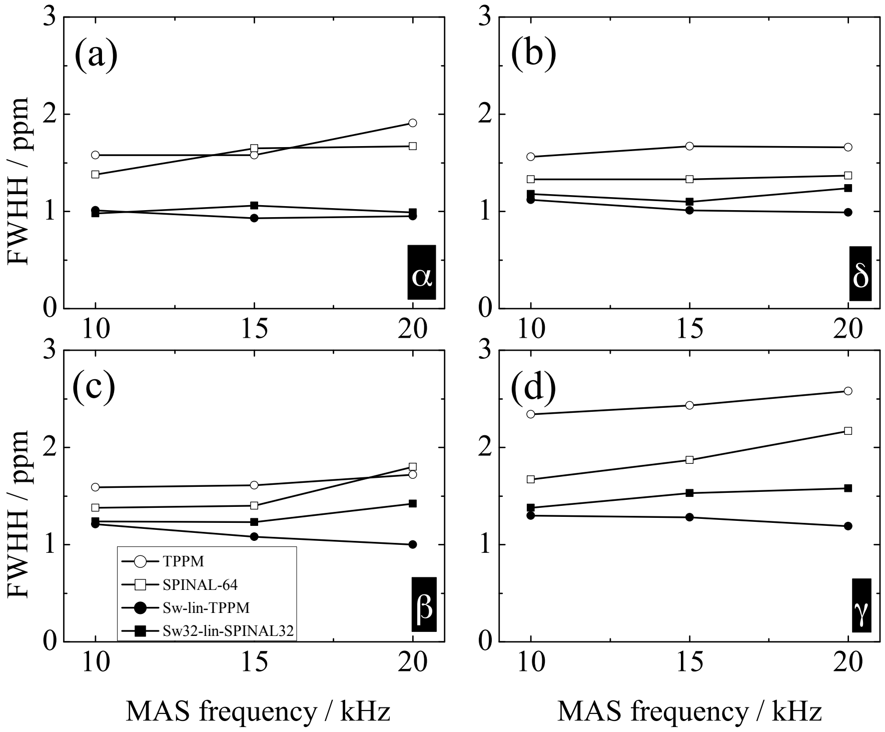

Figure 5.3: The decoupling performance at different MAS frequencies are compared here by plotting the full-width at half-maximum (FWHM) of the ^{13}C CP-MAS signals from (a) α, (b) δ, (c) β and (d) γ-carbons of NFBS-K for different decoupling sequences, namely TPPM, SPINAL, SW$_f$-TPPM and SW$_f$-SPINAL at 10, 15 and 20 kHz MAS. Here, in contrast to intensity plots, lower values (i.e., narrower lines) indicate better decoupling.

5.3 Numerical Simulations

The line intensities resulting from the experimentally best-performing SW$_f$-SPINAL and SW$_f$-TPPM decoupling sequences were also evaluated by numerical simulations with the SPINEVOLUTION [84] program. The 2D landscapes shown in Figure 5.4 portray the absolute intensity of the ^{13}C signal, from a system of a carbon-13 nucleus dipolar-coupled with four ^{19}F nuclei. For the fluorines, a CSA ($\Delta\delta$) of 16 kHz and a dispersion of ^{19}F chemical shifts ($d\delta_{iso}$) of 30 kHz were

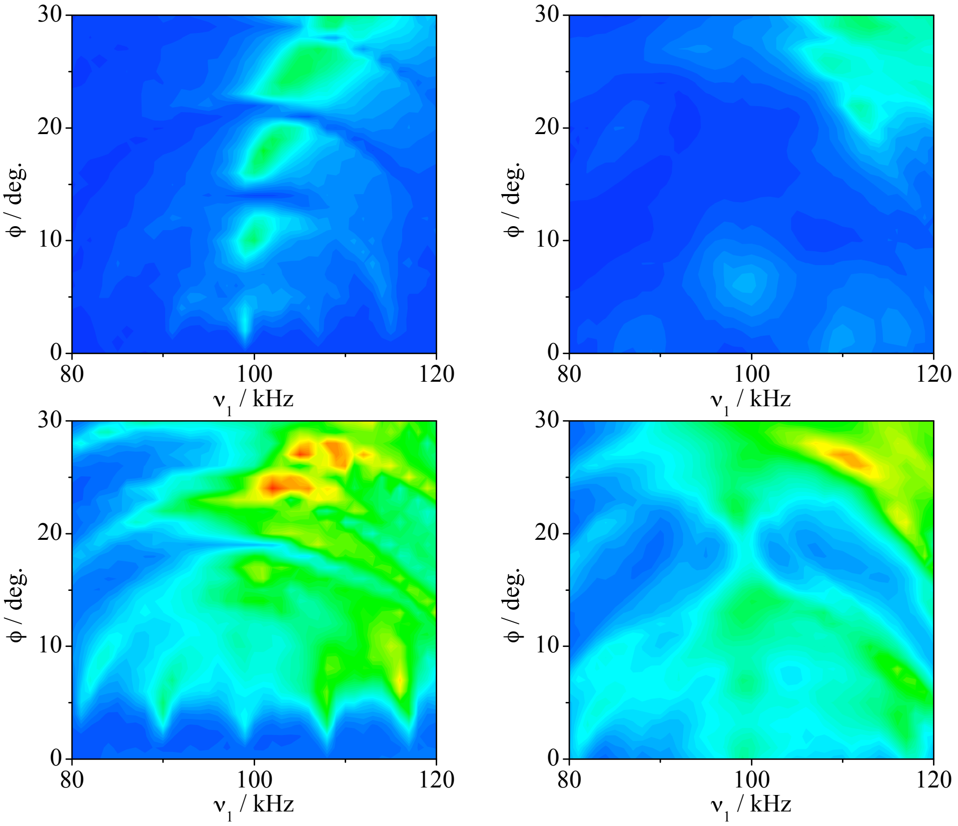

Figure 5.4: The 2D representation of SPINEVOLUTION [84] simulations of TPPM (top left), SW$_f^{lin}$-TPPM (bottom left): (both with 8.0808 kHz MAS); and SPINAL-64 (top right), SW$_f^{lin}$-SPINAL(bottom right): (both with 8.3333 kHz MAS) being plotted as the absolute intensity of the ^{13}C resonance as a function of RF strength (ν_1) and the phase angle (ϕ). A structural unit of 4 fluorines (^{19}F, with $\Delta\delta$ = 16 kHz) dipolar-coupled with a ^{13}C ($\Delta\delta$ = 0 kHz) was used for the calculations.

assumed. The ^{13}C signal intensity is shown as a function of the *RF* strength (ν_1) applied and the phase angles (ϕ) used. In Figure 5.4(bottom left), it may be seen that the SW$_f$-TPPM sequence produces a series of vertical high-intensity bands which represent the areas where the so-called *decoupling condition* is met (see Section 3.3). The location of these bands in the 2D landscape is determined by the

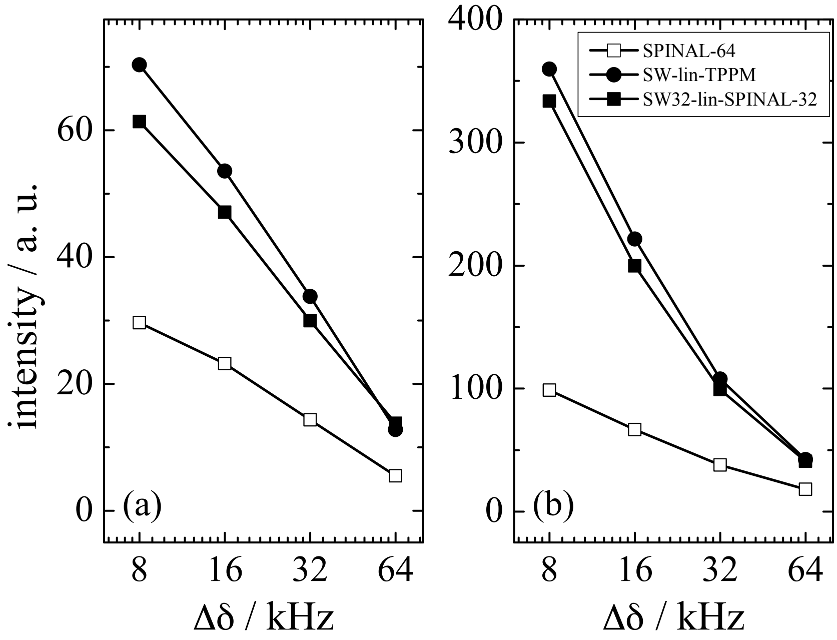

Figure 5.5: SPINEVOLUTION [84] simulations showing the decoupling performance of (i) SPINAL-64, (ii) SW$_f^{lin}$-SPINAL and (iii) SW$_f^{lin}$-TPPM sequences plotted as a function of (a) the highest intensity values in the 2D plot and (b) the collapsed (summed) intensities of the 2D landscapes, normalized by the matrix size. The decoupling performance was calculated for different chemical shielding anisotropies, $\Delta\delta$ = 8, 16, 32, and 64 kHz.

ratio of sequence cycle time and rotor period. For SW$_f$-SPINAL, a large spread of moderately good decoupling conditions is visible (Figure 5.4(bottom right)), albeit without the pronounced band structure observed for SW$_f$-TPPM. For the sake of comparison, numerical simulations of TPPM (Figure 5.4(top left)) and SPINAL-64 (Figure 5.4(top right)) on the same system are also presented, which exhibit only comparatively small areas of good decoupling efficiency. Thus, also in numerical simulations, the frequency-swept sequences are found to be better performing and more robust than both SPINAL and TPPM [110].

As explained above, the main difference between decoupling protons or fluorines as abundant spins is the fact that both the chemical shift anisotropy, $\Delta\delta$, and the isotropic dispersion, $d\delta_{iso}$, of ^{19}F is much larger. As in numerical simulations, these parameters may be changed at will, we explored the effect of increasing $\Delta\delta$ for ^{19}F on the decoupling efficiency. In order to do so, full 2D landscapes (such as shown in Figure 5.4) were calculated for the investigated decoupling sequences, with the chemical shift anisotropy $\Delta\delta$ of the ^{19}F being varied between 8 and 64 kHz. (By defining the $\Delta\delta$ in kHz, the results are rendered

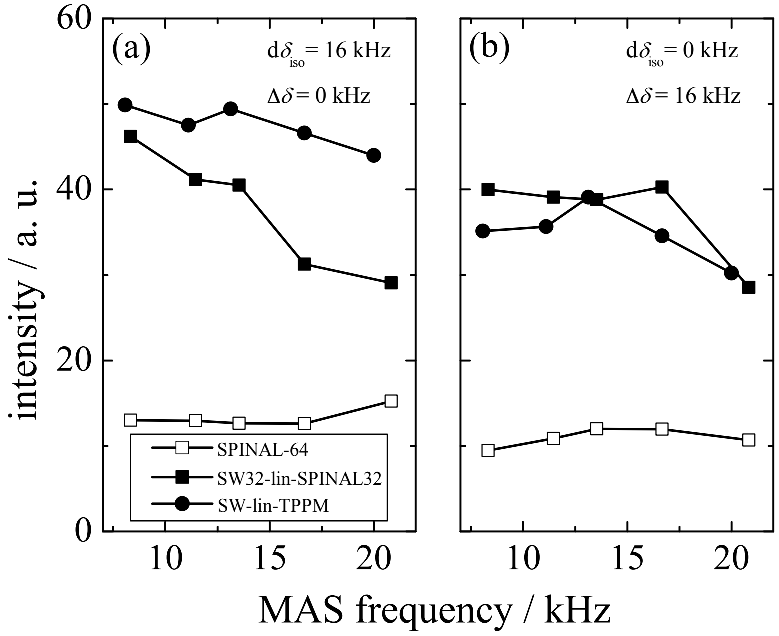

Figure 5.6: SPINEVOLUTION [84] simulations showing the decoupling performance of SPINAL-64, SW$_f^{lin}$-SPINAL and SW$_f^{lin}$-TPPM sequences plotted as a function of the collapsed (summed) intensities of the 2D landscapes of phase angles (ϕ) and *RF* strengths (ν_1) normalized by the matrix size. The ^{19}F parameters for the four fluorine in the structural units were: (a) $\Delta\delta = 0$ kHz; $d\delta_{iso} = 16$ kHz (with $\delta_{iso} = -8, -8, +8, +8$ kHz) and (b) $\Delta\delta = 16$ kHz; $d\delta_{iso} = 0$ kHz (with $\delta_{iso} = 0, 0, 0, 0$ kHz). The exact MAS frequencies used were 8.0808, 11.1111, 13.1313, 16.6666 and 20.0000 kHz for SW$_f^{lin}$-TPPM simulations, while for SPINAL-64 and SW$_f^{lin}$-SPINAL those were 8.3333, 11.4583, 13.5415, 16.6666 and 20.8333 kHz , to avoid interference effects of τ_c and τ_r.

independent of the applied magnetic field.) To handle the information of the 2D plots in a concise manner, we plotted both the maximum intensity found over the 2D grid, as well as the normalized overall intensity summed over the entire grid. These quantities were then plotted over the varying $\Delta\delta$, as depicted in Figure 5.5. The resulting dependence for both approaches looks very similar (5.5(a) and 5.5(b)), showing that the effect on maximum and overall intensity are almost identical. Comparing the different sequences, SW$_f$-TPPM performs best in ^{19}F decoupling, slightly outperforming SW$_f$-SPINAL, with both being well ahead in performance to SPINAL-64. With increasing $\Delta\delta$, the relative differences between the decoupling sequences diminish. The classification of sequences by performance, however, remains the same and is very much identical to that observed in the case of proton decoupling [73]. So although large ^{19}F chemical shift anisotropy tends to have a deleterious effect on the decoupling efficiency, the frequency-swept methods are always superior to the non-swept multi-pulse decoupling sequences [110].

Similar to the isotropic shift dispersion, which is entirely unaffected by MAS, the deleterious effect of the second-order recoupling of ^{19}F shift anisotropy and ^{13}C-^{19}F dipolar interaction on the line-width should not disappear even at faster MAS. This is evident from Figure 5.6, where the influence of $\Delta\delta$ and $d\delta_{iso}$ on the decoupling efficiency was investigated. For an assumed chemical shift anisotropy of $\Delta\delta = 16$ kHz, no beneficial effects of MAS can be observed even at 20 kHz spinning (cf. Figure 5.6(b)). This again points to the fact that the main effect of the chemical shift anisotropy on the residual ^{13}C line-width is via the second-order cross term [20, 21, 55, 74].

5.4 ^{19}F Decoupling: Reversal of sweep direction

As explained in Section 3.4, there is no influence of the sweep direction in the decoupling (here, ^{19}F) performance of the SW$_f$-TPPM sequence [83]. Figure 5.7(a) and 5.7(b) show the ^{19}F-decoupled ^{13}C spectra of NBFS-K at $\nu_r = 10$ kHz and $\nu_1 = 80$ kHz. The intensity obtained is the same irrespective of the direction of the linear sweep on the 11 pairs of pulses of SW$_f$-TPPM [83]. Figure 5.8 shows the offset-dependence of the β- and γ-^{13}C peaks of NBFS-K. The offset has been varied on the ^{19}F channel whilst the intensity of the ^{13}C peaks are monitored. The intensity obtained is independent of the direction of the sweep as both forward and reverse SW$_f$-TPPM deliver the same performance. For most implementations of SW$_f$-TPPM, the building block consists of an odd number of pulse pairs (usually 11) [72]. Therefore, reversal of the frequency sweep is easily accomplished by an exact inversion of the sequence around the centre pulse pair. Matters are more complex for decoupling sequences where both pulse duration and phase angle are altered within the building block like SW$_f$-SPINAL [73]. The addition of small phase angle increments in SPINAL is not done in a fully cyclic manner. This means that the basic building block (Q) starts and ends with different phase angles, making a symmetric inversion within Q impossible. Furthermore, the Q blocks are assembled into super-cycles of the type $Q\bar{Q}\bar{Q}Q\bar{Q}QQ\bar{Q}$, so sweeps may be defined in different extensions over the Q blocks. Consequently, the behaviour of the SW$_f$-SPINAL [73] sequence upon change of sweep direction is more complex. Experimentally and numerically, it is found that by inverting the pulse

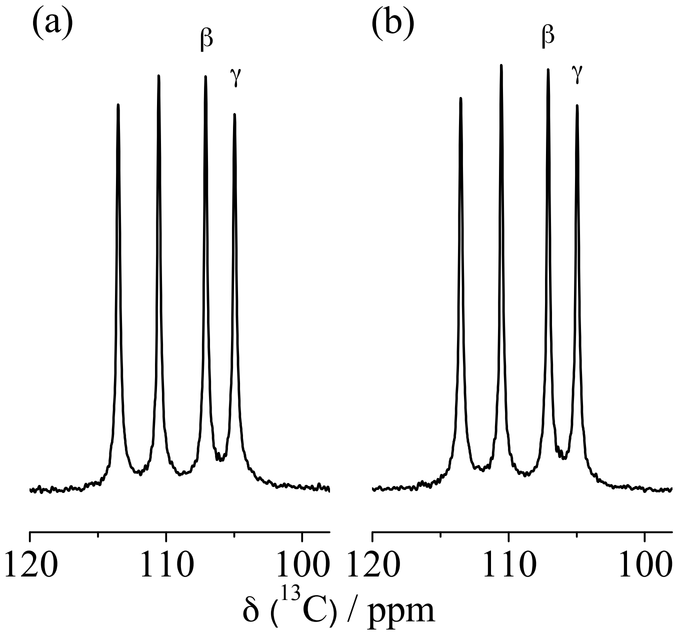

Figure 5.7: Spectral comparison of the ^{13}C resonances of the compound NBFS-K obtained by decoupling the ^{19}F abundant spins at ν_r = 10 kHz and ν_1 = 80 kHz, with (a) SW$_f$-for-TPPM and (b) SW$_f$-rev-TPPM methods.

duration increment only (i.e., keeping the phase change pattern as in the forward sweep), the performance tends to deteriorate. However, numerical simulations indicate that also for the fully inverted sequence, performance differences between forward and reverse sweeps may occur [83]. A similar complex behavior is expected for the super-cycled version of SW$_f$-TPPM, which was recently suggested for efficient spin decoupling in liquid crystalline systems [132].

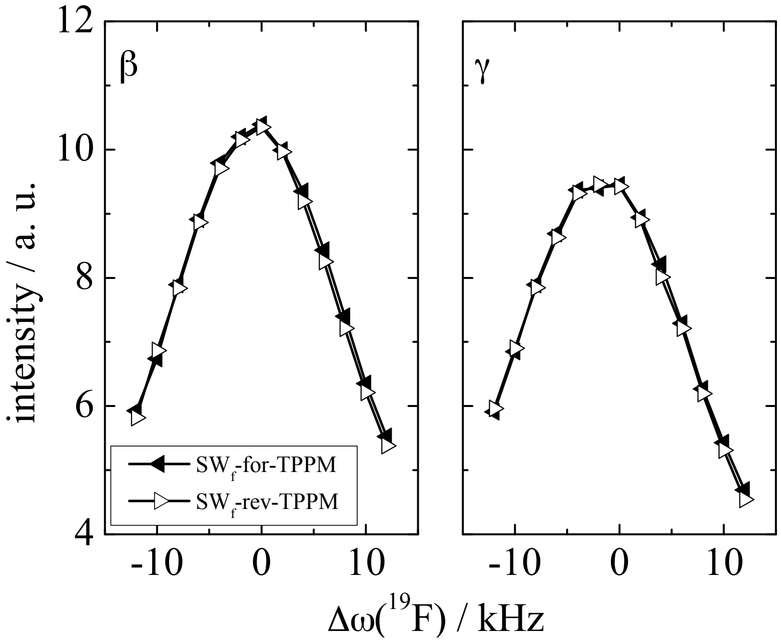

Figure 5.8: Offset dependence of the β (left) and γ(right) - ^{13}C resonances NBFS-K for forward (filled triangles) and reverse sweeps (hollow triangles) on SW$_f$-TPPM. The offset on the protons was varied in the range of ±10 kHz. The MAS frequency was kept at 10 kHz and the decoupling *RF* amplitude employed was 80 kHz.

Chapter 6

Decoupling while Observing Quadrupolar Nuclei

6.1 NMR of Quadrupolar Nuclei

Nuclei with spin number $I > \frac{1}{2}$ are called quadrupolar nuclei, and they constitute more than 73% of all NMR active nuclei [133–135]. These nuclei have a non-spherical distribution of the nuclear charge, which leads to the nucleus possessing a electric quadrupolar moment eQ (e is the elementary charge, and Q is a quantity with dimension $length^2$). This is usually measured in the unit barn ($1b = 10^{-28}m^2$). The eQ is an unique nuclear property and does not depend on chemical surroundings. The electric charge distribution around the nucleus may also have an asymmetry. The electric field gradients (EFG) thus produced interacts with the quadrupolar moment of the nucleus, and it is known as the *quadrupolar interaction*. The EFG generated by the electronic surrounding of the quadrupolar nucleus is described by a second rank tensor, which can be diagonalized to its PAS. The orientation dependence of this spherical tensor is defined by the Euler angles. The principal diagonal components of the EFG tensor can be represented, by convention, as $V_{XX} \leq V_{YY} \leq V_{ZZ}$. The largest tensor component is defined as $V_{ZZ} = eq$. The EFG tensor is traceless like the dipolar interaction tensor, and it is averaged completely by molecular motion in isotropic liquids [133–135].

In solid-state, the nuclear quadrupolar interaction usually dominates other internal spin interactions. The magnitude of quadrupolar interaction can be expressed either by (i) nuclear quadrupolar coupling constant (in MHz),

$$C_Q = \frac{eQ.V_{ZZ}}{h} \tag{6.1}$$

or (ii) the quadrupolar frequency (in MHz),

$$\nu_Q = \frac{3C_Q}{2I(2I-1)} \tag{6.2}$$

These magnitudes are characteristic values describing the symmetry of the electronic surrounding of the quadrupolar nucleus. In a perfect spherically symmetric lattice in solids, the EFG's cancel each other, resulting in zero quadrupolar coupling. But as soon as the systems changes from the spherical symmetry, the magnitude of C_Q increases. Another parameter η is defined as the asymmetry parameter of the quadrupolar interaction,

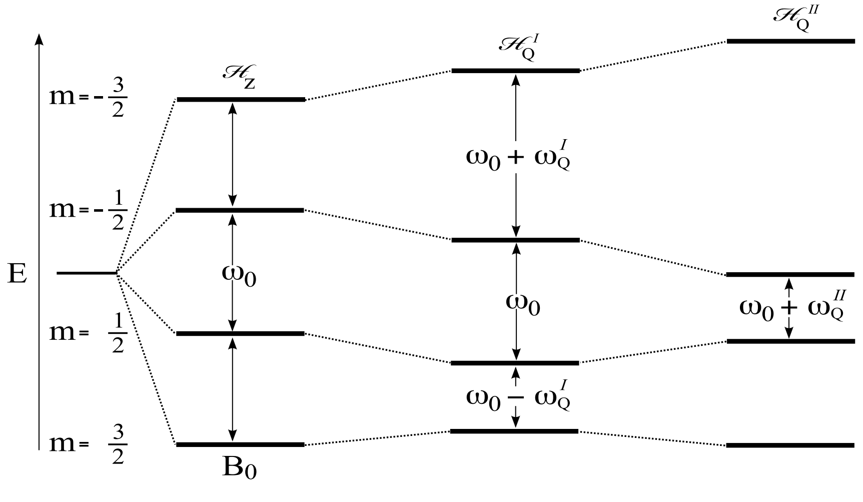
m=-3/2
m=-1/2
E
m= 1/2
m= 3/2
$\mathscr{H}_Z$
$\mathscr{H}_Q^I$
$\mathscr{H}_Q^{II}$
$\omega_0 + \omega_Q^I$
ω_0
ω_0
$\omega_0 - \omega_Q^I$
$\omega_0 + \omega_Q^{II}$
B_0

Figure 6.1: A schematic representation of the effects introduced by the Zeeman ($\hat{\mathscr{H}}_Z$) and the first ($\hat{\mathscr{H}}_Q^I$) and second ($\hat{\mathscr{H}}_Q^{II}$) order quadrupolar interactions on the energy levels of a nucleus with spin $I = \frac{3}{2}$.

$$\eta = \frac{V_{XX} - V_{YY}}{V_{ZZ}} \tag{6.3}$$

By convention, $0 \leq \eta \leq 1$, and η shows the deviation of the EFG from the condition of axial symmetry (i. e., $\eta = 0$). The following section discusses the quadrupolar interaction in half-integer-spin, $I > \frac{n}{2}$ systems, where $n = 3, 5, 7..$ etc.

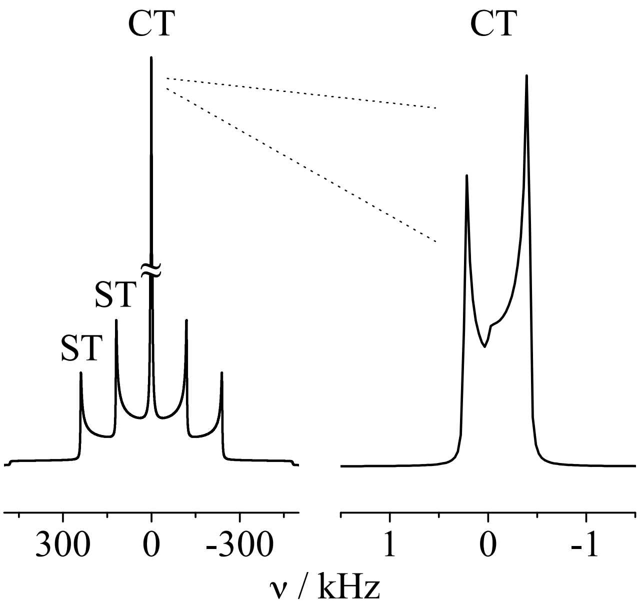

Figure 6.2: Simulated static first-order broadened powder line-shape of a nucleus with spin $I = \frac{5}{2}$, showing (left) central transition (CT) and satellite transitions (ST), and (right) a static powder line-shape of the CT alone. $C_Q = 1.6$ MHz, $\delta_{iso} = 0.00$ ppm and $\eta = 0.00$.

The quadrupolar interaction being very large compared to other internal spin interactions, additional NMR interaction energy is taken into account by quadrupolar Hamiltonians of first and second order (Figure 6.1). The first order contribution shifts the $m \rightarrow m+1$ transition by a frequency, $\nu_{m,m+1}$, which depends on the relative orientation of the tensor V to the external magnetic field, described by the Euler angles α and β [133–135]:

$$\nu_{m,m+1} = \frac{3C_Q}{2I(2I-1)}\left(\frac{3cos^2\beta - 1}{2} + \frac{\eta}{2}sin^2\beta cos2\alpha\right)\left(m + \frac{1}{2}\right) \tag{6.4}$$

The resonance of the central transition (CT) with $m = -\frac{1}{2}$ remains unaffected by this shift, and is therefore, easier to observe satellite transitions (ST). But the second order contribution of the quadrupolar interaction shifts the CT signal,

$$\nu_{-\frac{1}{2},+\frac{1}{2}} = \frac{-9C_Q^2}{6\nu_0[2I(2I-1)]^2}\left[I(I+1)-\frac{3}{4}\right](Acos^4\beta + Bcos^2\beta + C) \tag{6.5}$$

with ν_0 being the Larmor frequency of the nucleus. The coeffients A, B, and C enclose the dependencies on α and β and are listed in Ref. [134]. Because of the spatial dependence of $\nu_{-\frac{1}{2},+\frac{1}{2}}$ the CT resonances of quadrupolar nuclei in polycrystalline samples appear broadened. To a certain extent, this broadening remains even under magic-angle spinning (MAS) conditions, as MAS averages out only contributions that scale with $\cos^2\beta$, but not $\cos^4\beta$ (scales like the fourth order Legendre polynomial, as shown in Figure 2.4). In practice, solid-state NMR characterization of materials containing quadrupolar nuclei is often restricted to observing the position and shape of such broadened CT peaks, either under static or MAS conditions. If the singular characteristic second-order shape of the CT

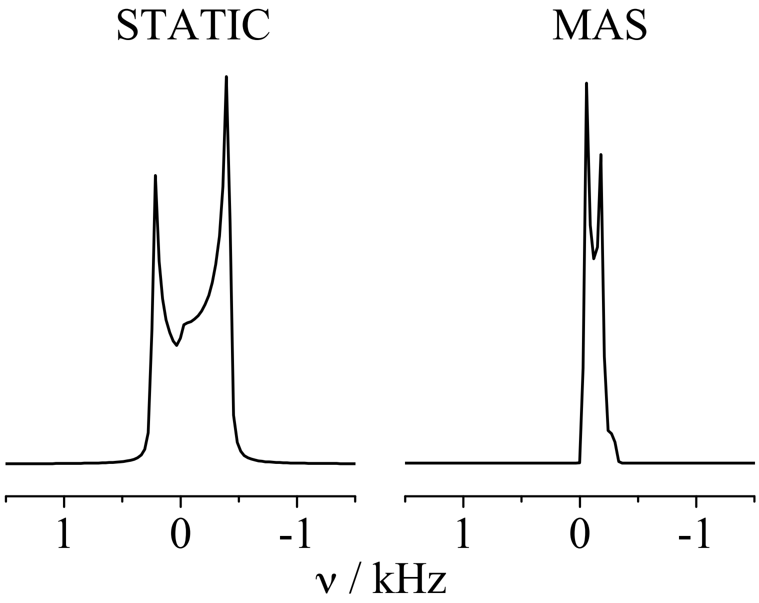

Figure 6.3: Simulated static first-order broadened powder line-shape of a nucleus with spin $I = \frac{5}{2}$, showing (left) central transition (CT), and (right) a MAS powder line-shape of the CT. $C_Q = 1.6$ MHz, $\delta_{iso} = 0.00$ ppm and $\eta = 0.00$.

resonance can be observed, the NMR interaction parameters may be determined from one-dimensional spectra [134–136], and may be correlated to structure and properties of the compounds under investigation. If multiple sites of the observed nucleus are present, however, the second-order shapes will often overlap in the spectrum, making spectral deconvolution difficult. One method to reduce this effect is to apply very high static magnetic fields, which can scale down the influence of the quadrupolar second order effects. The following section describes a few examples of such overlapping ^{27}Al second-order quadrupolar lines, and their de-convolutions, mostly with the help of density functional theory (DFT) calculations and/or supporting measurements.

6.2 Solid-state NMR of ^{27}Al

This section describes three different cases of mixed ^{27}Al crystallographic environments, two of them showing well-defined second order line-shapes, and the third showing distributions in quadrupolar and chemical shift parameters. In all cases, the acquired ^{27}Al-NMR spectra were analysed using the DMFIT [136] program.

6.2.1 Aluminium carbide

The first case is of aluminium carbide (Al_4C_3), which has two aluminium sites Al1 and Al2, as shown by x-ray diffraction data [137]. For acquisition of reasonably well-defined ^{27}Al NMR spectra, a comparatively strong magnetic field of $B_0 = 17.6$ T needed to be employed, because of the large quadrupolar coupling of $C_Q(^{27}\mathrm{Al}) \approx 16$ MHz [138]. Large quadrupolar couplings for ^{27}Al were observed before for carbon-coordinated aluminium [139]. The ^{27}Al NMR spectra of Al_4C_3 under both static and MAS conditions were deconvoluted into two spectral components. The spectral fit allowed for determination of the quadrupolar coupling constants of both ^{27}Al species, with one displaying a tendency of having a slightly smaller C_Q. The C_Q's obtained from the deconvolution of MAS NMR spectrum are 15.58 (Al1) and 15.83 (Al2) MHz, whereas, those from the static NMR spectrum are 15.46 (Al1) and 16.10(Al2) MHz, for the two overlapping ^{27}Al sites. The deconvolution method [136] also helped to find out the isotropic chemical shift

(δ_{iso}) values of two ^{27}Al sites. They are 120.1 (Al1) and 111.2 (Al2) ppm for the MAS spectrum and 136.8 (Al1) and 106.3 (Al2) ppm for the static spectrum. By carrying out DFT calculations of the EFG tensor V at the ^{27}Al sites using the Wien2k software [140], the smaller C_Q site was assigned to be the crystallographic Al1 species. The EFG tensor V was calculated with the atomic coordinates taken from the X-ray structure and later with the optimized lattice parameters and atomic positions using the Wien2k code. Applying the PBE generalised gradient approximation [141], a k grid of 110 points was used for integration over the irreducible part of the Brillouin zone. The APW+lo basis was chosen added by local orbitals for $L = 0$ on carbon. The radii of the atomic spheres were 2.1 bohr (Al) and 1.3 bohr (C). The number of plane waves was determined by the cut-off $R_{mt}K_{max} = 7.0$. The minimal energy with respect to the structural parameters was found by varying the lattice parameters a and c followed by an optimisation of the internal parameters (forces $< 0.5 mRy/bohr$) [138].

6.2.2 Strontium aluminate

A similar situation of overlapping ^{27}Al multiple sites are found in the second case, namely, strontium aluminate ($SrAl_{12}O_{19}$) [142]. A low magnetic field ^{27}Al NMR study reported a total of five different aluminium sites in $SrAl_{12}O_{19}$, namely an AlO_4, an AlO_5 and three AlO_6 environments [143]. This was contested by another study showing that the AlO_5 site is indeed the distorted AlO_4 site, with a very large quadrupolar coupling [144]. But acquiring ^{27}Al spectra at three magnetic fields (at 7.05, 16.4 and 17.6 T) unambiguously showed the simultaneous presence of the AlO_4 and AlO_5 sites in $SrAl_{12}O_{19}$ [142].

6.2.3 Aluminium oxide deposited spider-silk

The third case is of aluminium sites in alumina (Al_2O_3) deposited on spider-silk fibers, with the help of vapor phase infiltration techniques [145]. The extraordinary increase of toughness of such a fiber was attributed to the infiltrated alumina species into the bulk of the spider-silk, and the possible interactions with the bio-material [145]. ^{27}Al MAS NMR was helpful in this case to differentiate the contributions from the alumina present in the surface and bulk of spider-silk.

The two samples investigated (at 17.6 T magnetic field) are Al_2O_3 atomic-layer-deposited (ALD) para-film and dragline silk fibers of an *Araneus* spider. The Al_2O_3 cannot infiltrate to the bulk of the para-film material. The ^{27}Al MAS (at 20 kHz) NMR spectrum of the para-film sample showed three contributions from AlO_4, AlO_5 and AlO_6 sites, but with distribution of quadrupolar and chemical shift parameters. Since there was only a very small thickness of Al_2O_3 on the surface, distributions of NMR parameters were expected. The DMFIT [136] program assumes a Gaussian distribution of the chemical shift [147, 148], so that line fitting delivers a value for the isotropic chemical shift, δ_{iso}, plus the width of the distribution. For the quadrupolar coupling, a Czjzek distribution [146, 148] is used in a simplified form [136, 147], which results in an average quadrupolar coupling parameter. In the case of the spider-silk sample, in addition to the three peaks of AlO_4, AlO_5 and AlO_6 sites, there is a second octahedral alumina species with the δ_{iso} equal to -4.9 ppm. Significantly, a negative value of δ_{iso} has also been observed for ^{27}Al in the presence of organic ligands [149], which may indicate the vicinity of organic material for the second AlO_6 species. Moreover, by integration of the relative line intensities of the contribution of all species, it can be seen that only 9% of the observed aluminum is located in such surroundings. All these data are consistent with the situation of aluminum infiltrated into the spider silk bulk and/or interacting with the surface of the protein [145].

6.2.4 Need of a high-resolution method

The three cases described above are special, in the sense that, even if there are overlapping second-order CT lines, one could use different supporting methods to separate the contributions. But the unawareness of the X-ray crystal structure, presence of large quadrupolar couplings, and distribution of NMR parameters can produce complications understanding NMR line-shapes. A number of experimental approaches have been suggested to resolve overlapping CT lines. The techniques like DOR (double rotation) [150] and DAS (dynamic angle spinning) [151] are used for averaging out the effects of the second-order interaction term but the experiments require specialised probes that are not readily available. Since L. Frydman and J. S. Harwood introduced the MQMAS (Multiple-Quantum Magic-

Angle Spinning) [152–155] technique, which can be run using most solid-state MAS NMR probes, it has become the most frequently used high-resolution technique for the study of quadrupolar nuclei.

6.3 Solid-state NMR of ^{45}Sc

This section focuses on ^{45}Sc solid-state NMR studies of an inorganic compound, scandium sulphate pentahydrate and the following subsection introduces the high-resolution method employed, MQMAS [152–155].

6.3.1 Multiple-Quantum Magic-Angle Spinning

Multiple-Quantum Magic-Angle Spinning (MQMAS) [152–155] is a two dimensional MAS NMR technique applied for high-resolution in NMR spectra of half-integer spin quadrupolar nuclei. The method produces a resolved isotropic spectrum in an indirect dimension, correlated to the direct MAS dimension. This is the result of simultaneous manipulation of spin and spatial contributions of the quadrupolar Hamiltonian. Since the technique is always carried out in combination with MAS, the line-broadening contributions from CSA and second rank tensor elements of the quadrupolar interaction can be completely removed by spatial averaging. Then the remaining spin part of the quadrupolar Hamiltonian is manipulated by different RF pulses. These simultaneous averaging techniques remove the fourth rank (second-order) quadrupolar interaction completely. The spin space averaging is realized by the formation of an echo by correlating the frequencies of symmetric multiple-quantum coherences (MQC) and single-quantum coherences (SQC) in polycrystalline samples. The echo formation is analogous to taking mirror images of the second-order broadened CT line-shapes and their averaging, similar to spatial averaging with DAS [151]. In a 2D MQMAS experiment, the coherences are allowed to evolve during times t_1 and t_2 in F_1 and F_2 dimensions. At certain combinations of t_1 and t_2, the fourth rank quadrupolar interaction vanishes. Now, by choosing proper coherence orders (p), one can remove the anisotropies to induce an isotropic echo. On Fourier-transformation of the time domain data, in the 2D spectrum, the isotropic peaks with high-resolution

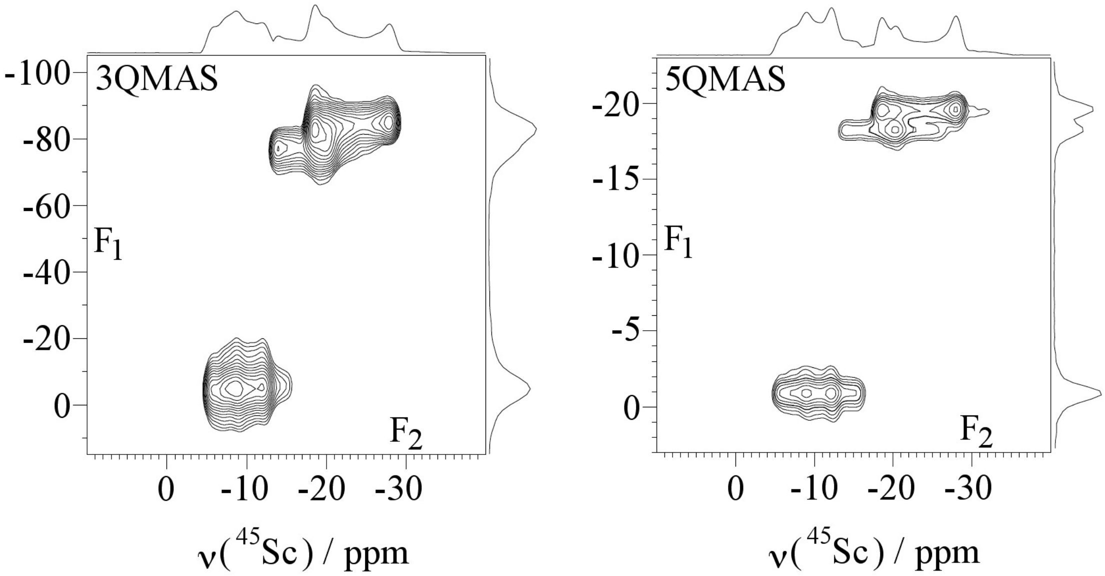

Figure 6.4: 2D ^{45}Sc-3QMAS (left) and 5QMAS (right) spectra of scandium sulphate pentahydrate powder at $B_0 = 9.4$ T and 12 kHz MAS. The 5QMAS spectrum shows high-resolution in the indirect (F_1) dimension.

(with chemical shift information) are retained [152–155] as shown in Figure 6.4.

The simplest MQMAS pulse sequence consisted of two pulses [153]. The first pulse excites all MQ coherences and the desired coherence is filtered out by a suitable phase cycling. Then the MQ coherence evolves during a time t_1, which is followed by a MQC-to-SQC conversion pulse. The t_1 increment is then applied and the two pulse scheme is then repeated to form a 2D landscape. But on FT the 2D spectrum is tilted. A shearing transformation is necessary to view the spectrum with horizontal ridges, the projection of which to the F_1 dimension gives the isotropic spectrum. The split-t_1 method, introduced by Brown *et al.* [156, 157] consists of three pulses: an excitation pulse, a conversion pulse and a soft π pulse to shift the echo. The t_1 time should be adjusted to the MQC evolution. The duration t_2 is equal to a constant (k) multiplied by t_1, and the value of k depends on the spin quantum number I and the coherence order p. By properly combining the MQ and the SQ evolution times (as certain multiples of the t_1 time) in the t_1 time domain, the method gets rid of the movement of the echo. With the ridges lying parallel to the F_2 axis, one does not need a shearing transformation to get the isotropic projections. All the 2D MQMAS experiment results presented in this chapter are recorded with the split-t_1-whole-echo method [156, 157].

Although a large resolution gain is achieved, the acquisition of MQMAS spectra of quadrupolar nuclei with half-integer spin is often hampered by inherently low sensitivity, due to the low efficiency of excitation and conversion of multiple-quantum coherences. As shown by extensive tabulations of MQMAS studies in a review [155], the most widespread application of MQMAS is in the form of the three-quantum (3Q) experiment. The 3QMAS experiment can be performed on all nuclei with half-integer spin $I \geq \frac{3}{2}$, and may be acquired with a reasonable signal-to-noise ratio. For spin-$\frac{7}{2}$ nuclei, also the 7Q or 5Q coherence pathway may be chosen for acquisition of MQMAS spectra, however the sensitivity is sharply declining for the higher coherence orders. For nuclei with spin $I = \frac{7}{2}$, like ^{45}Sc or ^{139}La, the ratio of the respective 3Q : 5Q : 7Q signal intensities has been estimated to be $6\frac{2}{3} : 2\frac{2}{3} : 1$ [158]. Nevertheless the acquisition of 5Q or 7Q spectra is of interest, as it has been shown in several instances that higher coherence orders may yield a substantial improvement in resolution in the F_1 (isotropic) dimension of the MQMAS spectrum [159, 160]. This is also shown in Figure 6.4 that, from 3QMAS to 5QMAS, there is a large improvement in resolution.

6.3.2 MQMAS Sensitivity enhancement

Because of the poor signal-to-noise ratio of MQMAS spectroscopy, numerous efforts have been devoted to achieving better sensitivity. The majority of enhancement schemes developed so far has been aimed at improving the efficiency of the MQ→1Q conversion process. Instead of employing a hard radio-frequency (RF) pulse P_H^{con}, a number of schemes replacing it has been suggested for more efficient conversion. These pulse schemes include double frequency sweeps (DFS) [161, 162], rotationally induced adiabatic coherence transfer (RIACT) [163], hyperbolic secant pulses (HS) [164], fast-amplitude modulation (FAM) [165–167], and frequency-swept FAM (SW-FAM) [168]. The FAM method approximates an amplitude modulation of appropriate frequency by a series of pulse pairs, with each of the pairs consisting of two pulses with a 180° phase shift between them. The simplest FAM pulse train (known as FAM-I) is formed by a block of pulse pairs of uniform duration τ_p, separated by constant interpulse delays τ_w, which are usually of duration τ_p as well. With x and $\bar{x}$ representing the phases of the pulses, the basic building block of a FAM-I sequence may be written as $[\tau_p(x)$ - τ_w - $\tau_p(\bar{x})$-$\tau_w]_N$, with the basic block repeated N times. A FAM-II pulse train, on the other hand, consists of a short series of pulses with decreasing duration, and may be written [τ_p^1(x) - τ_w - $\tau_p^2(\bar{x})$ - τ_w ...]. with the durations $\tau_p^1 > \tau_p^2 >$... shortening. The enhancement on applying FAM-II sequence instead of a hard pulse (as shown in Figure 6.5(a)), for MQ→1Q conversion, can be seen in Figure 6.5(b) from the 5Q-filtered ^{45}Sc MAS NMR spectrum of scandium sulphate pentahydrate (ScSPH) [169]. The utilisation of enhancement techniques for improving excitation efficiency has received less attention. A FAM-I pulse train following the hard excitation pulse [170], further increases the sensitivity, as shown in Figure 6.5(c). For the 5Q filtered spectra obtained with the three different methods

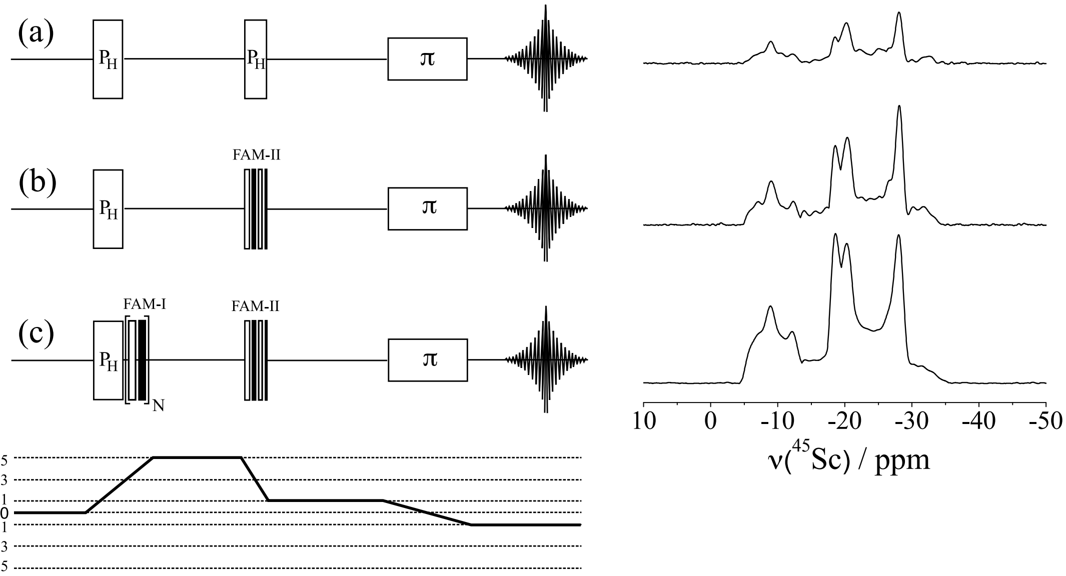

Figure 6.5: Diagrammatic representation of the 5QMAS split-t_1 pulse sequences with different 5Q coherence excitation and conversion parts. (a) Use of hard *RF* pulses, $P_H^{exc} - P_H^{con}$; (b) use of FAM-II coherence conversion, P_H^{exc}-FAM-II; (c) additional use of a FAM-I pulse train for improved 5Q excitation, [P_H^{exc}-FAM-I]–FAM-II. Below, the schematic coherence pathway of the 5QMAS experiment is given. The 5Q-filtered ^{45}Sc-NMR spectra of scandium sulphate pentahydrate (ScSPH) obtained with the pulse schemes (a)–(c) are shown on the right.

shown in Figure 6.5(a), (b) and (c), the intensity ratio increases as 2 : 3 : 6 respectively [169]. In short, the signal enhancement methods discussed here allow the partial retrieval of the signal intensity that is lost when going to a higher coherence order.

6.3.3 Solid-state NMR and DFT calculations

From the single-crystal X-ray data [180] of ScSPH, it is known that one scandium is residing in a general position, designated as Sc(1), while the other two, Sc(2) and Sc(3), are occupying special positions, namely inversion centres. A full ^{45}Sc-5QMAS spectrum (see Fig. 6.6) of ScSPH was collected using the [P_H^{exc}-FAM-I]–FAM-II enhancement scheme and SW$_f^{lin}$-TPPM proton decoupling (discussed in details in Section 6.4.1). The three scandium sites are sufficiently resolved in the F_1 dimension to be able to unequivocally assign the corresponding F_2 traces as shown in Figure 6.6. These traces were fitted with the DMFIT program [136], to obtain the isotropic chemical shift δ_{iso}, the quadrupole coupling constant C_Q, and the asymmetry parameter η, which are in good agreement with the val-

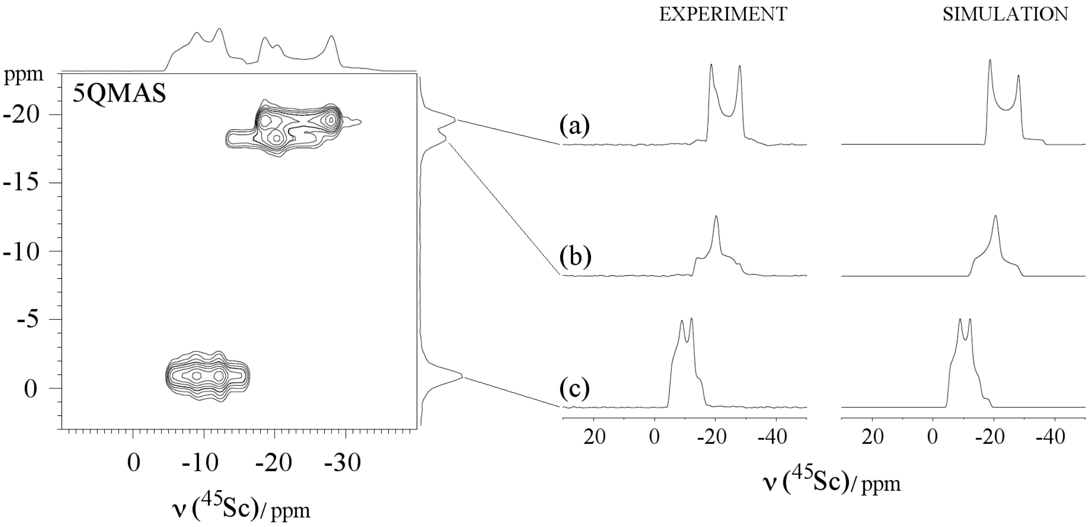

Figure 6.6: 2D ^{45}Sc 5QMAS (left) spectrum of scandium sulphate pentahydrate powder at B_0 = 9.4 T and 12 kHz MAS and the F_2 traces and DMFIT [136] simulations (right) of the three ^{45}Sc crystallographic sites.

ues obtained by DFT calculations. The DFT calculations allowed assignment of the ^{45}Sc resonances to the scandium sites in the crystallographic unit cell. These assignments were in agreement with the qualitative response observed when comparing decoupled to non-decoupled spectra [169] and with the calculated dipolar couplings between ^{45}Sc and ^{1}H from the X-ray crystal structure [180].

Table 4. ^{45}Sc-NMR parameters (quadrupole coupling constant C_Q, asymmetry parameter η, isotropic chemical shift, δ_{iso}, and isotropic shielding, σ_{iso}) extracted from NMR experiments and obtained from DFT calculations for Sc-SPH using the GIPAW [171], PAW [172] and APW + lo [140, 173] methods. The computed isotropic shielding values are arbitrarily shifted so that the highest value is equal to zero. Listed are the calculation results obtained from X-ray and energy-optimised (Opt.) crystal structures.

Site			Sc(1)	Sc(2)	Sc(3)
			(c)	(a)	(b)
C_Q (MHz)	Measured		4.55	5.60	4.50
	Computed	X-ray PAW	-6.64	-14.36	10.59
		Opt. PAW	-4.64	-5.35	5.54
		Opt. APW + lo	-5.53	-5.43	6.00
η	Measured		0.50	0.06	1.00
	Computed	X-ray PAW	0.98	0.23	0.53
		Opt. PAW	0.72	0.10	0.68
		Opt. APW + lo	0.71	0.23	0.54
δ_{iso} (ppm)	Measured		-4.7	-15.5	-12.9
$-\sigma_{iso}$ (ppm)	Computed	Opt. GIPAW	0.0	-19.3	-8.5

The GIPAW (Gauge-Including Projector Augmented Wave) method [171] has been used for calculation of the chemical shift, whereas the quadrupolar parameters have been computed using both the PAW (Projector Augmented Wave) [172] and the APW + lo (Augmented Plane Wave + local orbital) [140, 173] approaches. From the calculated chemical shift and quadrupolar coupling values, given in Table 4, the ^{45}Sc site assignment is done. The (a), (b) and (c) ^{45}Sc species resolved in the 5QMAS spectrum (see Fig. 6.6) were assigned to Sc(2), Sc(3) and Sc(1) crystallographic sites respectively.

6.4 Spin Decoupling during MQ Evolution

It has long been understood that application of heteronuclear dipolar decoupling sequences may aid the quality of solid-state NMR spectra acquired from quadrupolar nuclei [79, 176–178]. In the following two subsections of this chapter, ^{1}H and ^{19}F decoupling of quadrupolar nuclei, during a multiple-quantum evolution in MQMAS experiments are discussed. Whereas the MAS spectrum of the observed quadrupolar nuclei may only marginally be affected by the application of heteronuclear decoupling, the MQ-filtered signals are very sensitive to it, as the de-phasing (during the p-quantum coherence evolution period) caused by the dipolar interaction between the coupled nuclei is p-fold magnified. Theoretical descriptions of this effect under MAS were put forward by Duer [174] and Friedrich *et al.* [175] using spherical tensor notation. For a static case, the p-fold de-phasing can also be understood in a straightforward manner by evaluating the influence of the dipolar interaction on the energy levels of the half-integer spin nucleus, as shown in the Appendix A.

6.4.1 Proton decoupling

The use of multi-pulse sequences may strongly improve the quality of decoupling for quadrupolar nuclei [177]. In a recent work, P. K. Madhu and co-workers have shown the further improvement in decoupling efficiency using SW$_f$-TPPM method for decoupling ^{1}H during 3Q- and 5Q-evolution of ^{27}Al in the mineral gibbsite [79]. SW$_f$-TPPM with a tangential sweep profile outperformed the conventional CW, TPPM and SPINAL-64 methods by consistent margins [79]. This section discusses the ^{1}H decoupling performances of TPPM, SPINAL-64, SW$_f^{lin}$-TPPM and SW$_f^{tan}$-TPPM methods by comparing the ^{45}Sc 5QMAS signals of scandium sulphate pentahydrate (henceforward abbreviated to ScSPH) [169]. Because of the presence of water protons, ScSPH constitutes a good sample to explore the effects of heteronuclear decoupling on MQMAS spectra.

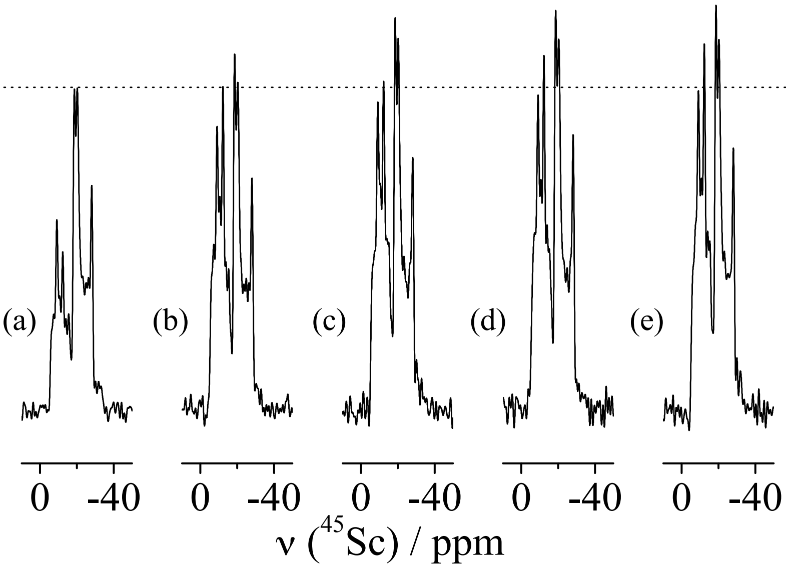

Figure 6.7: 5Q-filtered ^{45}Sc NMR spectra (F_2 dimension) of ScSPH acquired (a) without ^{1}H decoupling and with (b) TPPM, (c) SPINAL-64, (d) SW$_f^{tan}$-TPPM and (e) SW$_f^{lin}$-TPPM ^{1}H decoupling methods at 12 kHz MAS.

^{45}Sc 5QMAS spectra of ScSPH were acquired on a Bruker AVANCE-II 400 spectrometer, at a Larmor frequency of $\nu_0(^{45}\text{Sc}) = 97.214$ MHz, using a 4 mm MAS probe. All spectra were referenced to a dilute ScCl$_3$ solution at 0 ppm. For the 5QMAS spectra acquisition, a split-t$_1$-whole echo sequence [156, 157] was used. The isotropic (F_1) dimension of the MQMAS experiments have been labeled according to the convention which scales the evolution period by $(1 + k)$ [179], with k depending on the observed spin and coherence order. In the case of ^{45}Sc with $I = \frac{7}{2}$, the scaling factor $(1 + k)$ is $\frac{20}{9}$ for 5QMAS, with the k value $\frac{11}{9}$ [179].

The parameters governing decoupling performance were optimized for different sequences. While the phase angle (ϕ) used for TPPM (6.25°) and SPINAL-64 (12.5°) are different, those used for SW$_f^{tan}$-TPPM and SW$_f^{lin}$-TPPM are the same (7.5°). The phase increments α and β in SPINAL-64 were 5° and 10°, respectively. In the case of SW$_f^{tan}$-TPPM, the best tangent cut-off angle was found to be 60°, and the optimised sweep widths of both SW$_f^{tan}$-TPPM and SW$_f^{lin}$-TPPM were 0.80 and 0.92 with sweep windows of 0.60–1.40 and 0.54–1.46 (11 pulse pairs

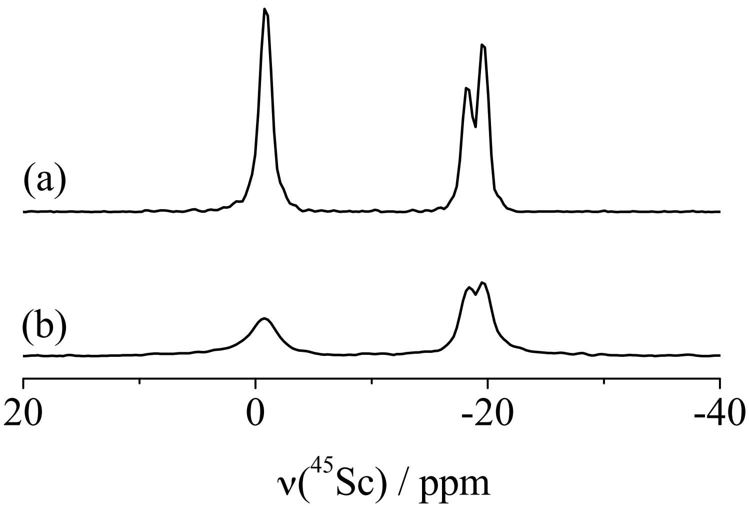

Figure 6.8: The F_1 (isotropic) projections of ^{45}Sc 5QMAS spectra of ScSPH at 12 kHz MAS acquired (a) with SW$_f^{lin}$-TPPM ^{1}H decoupling and (b) without ^{1}H decoupling.

each), respectively [169].

In ScSPH, the heteronuclear (Sc–H) dipolar couplings (max. $\approx$ 2500 Hz) are much larger than the homonuclear Sc–Sc couplings (max. $\approx$ 50 Hz), as per the distances calculated from the XRD structure [180]. Therefore, the Sc–H dipolar couplings should easily be averaged out by the applied MAS of 12 kHz. This is indeed the case for acquisition of single-quantum ^{45}Sc-MAS spectra, which remain entirely unaffected by irradiation of the proton channel. However, the situation is different for MQMAS: quantum coherences of order p are more sensitive to dipolar couplings, because of the p-fold dephasing of the signal during the p-quantum coherence evolution period (see Appendix) [174, 175]. This also means that a 5QMAS spectrum benefits more from the application of decoupling than a 3QMAS experiment [169].

In Figure 6.7, the ^{45}Sc 5Q-filtered spectra of ScSPH obtained with the decoupling techniques TPPM, SPINAL-64, SW$_f^{tan}$-TPPM, and SW$_f^{lin}$-TPPM are shown, and compared to the spectrum acquired without decoupling [169]. The effect of proton decoupling on the 5Q-filtered spectra is clearly observed, quite in contrast to the single-quantum MAS spectra of ScSPH. As can be seen from

Figure 6.7, the SW$_f^{lin}$-TPPM sequence [81] performs best for the ScSPH sample. Acquisition of MQ-filtered spectra with short evolution delay may thus be used for finding and optimising the best decoupling scheme. The actual improvement, however, becomes apparent only when comparing the isotropic (F_1) projections of the full 2D 5QMAS experiment, as shown in Figure 6.8. The application of efficient heteronuclear decoupling leads to a dramatic intensity increase with a concomitant improvement in resolution. Another aspect reflecting on the importance of high quality heteronuclear decoupling is the fact that, according to the crystallographic data [180], the three ^{45}Sc resonances observed in the F_1 dimension of the 5QMAS spectrum should be of equal intensity. Even with the most efficient proton decoupling, the F_1 projection shown in Figure 6.8(a) still does not exhibit equality of intensities [169]. However, the respective ratios are better than what may be found in previously recorded 5QMAS spectra of ScSPH [159, 181].

6.4.2 Fluorine decoupling

In solid-state NMR studies of minerals and ion conductors, quadrupolar nuclei like ^{7}Li, ^{23}Na or ^{133}Cs are frequently situated in close proximity to fluorine [182–185], so that application of ^{19}F decoupling is beneficial for spectral resolution. It is known that ^{19}F-decoupling is more challenging than proton decoupling because fluorine possesses a much larger chemical shielding anisotropy (CSA) and a wider dispersion of isotropic chemical shifts. For a spin-$\frac{1}{2}$ nucleus (^{13}C) in a rigid organic solid, it is shown in Chapter 5, that the large chemical shift interaction of ^{19}F does indeed compromise the decoupling performance of multi-pulse sequences [110]. Here, the decoupling efficiency of various multi-pulse decoupling sequences (TPPM, SPINAL-64, SW$_f$-TPPM and SW$_f$-SPINAL) are compared by acquiring ^{19}F-decoupled ^{23}Na NMR spectra of cryolite (Na_3AlF_6) [186].

The ^{23}Na NMR spectra of Na_3AlF_6 were acquired on Bruker AVANCE-III 400 spectrometer, at a Larmor frequency of $\nu_0(^{23}\text{Na}) = 105.843$ MHz, using a 4 mm MAS probe at spinning frequencies of 10–12 kHz. The ^{23}Na NMR chemical shifts were referenced to a dilute aqueous sodium chloride (NaCl) solution, with the ^{23}Na signal at 0 ppm. For the acquisition of full 3QMAS spectra (Figure 6.10), a split-t_1-whole echo sequence [156, 157] with a 48-step phase cycle was used. (For

^{23}Na with $I = \frac{3}{2}$, a 48-step cycle was sufficient to obtain an artefact-free spectrum, although the recommended phase cycle for a split-t_1-whole echo 3QMAS contains 96 steps [155].) Three hundred and sixty transients were recorded for each t_1 increment of 25 μs, with 128 increments in the F_1 dimension. The classical two-pulse scheme (see Section 6.3.1) for 3Q excitation and conversion, $P_H^{exc} - P_H^{con}$, was used with a short 3Q evolution delay of $t_1 = 3$ μs to optimize the respective pulse durations, with the best values being $P_H^{exc} = 3.0$ μs and $P_H^{con} = 1.5$ μs with a RF nutation frequency of 111 kHz. The selective split-t_1-echo pulse was 20 μs with a nutation frequency of 28 kHz. The isotropic (F_1) dimension of the MQMAS experiments have been labeled according to the convention which scales the evolution period by $(1+k)$. For a 3QMAS experiment of ^{23}Na ($I = \frac{3}{2}$) nucleus, the F_1 scaling factor is $\frac{16}{9}$, with the k value being 7/9 [179].

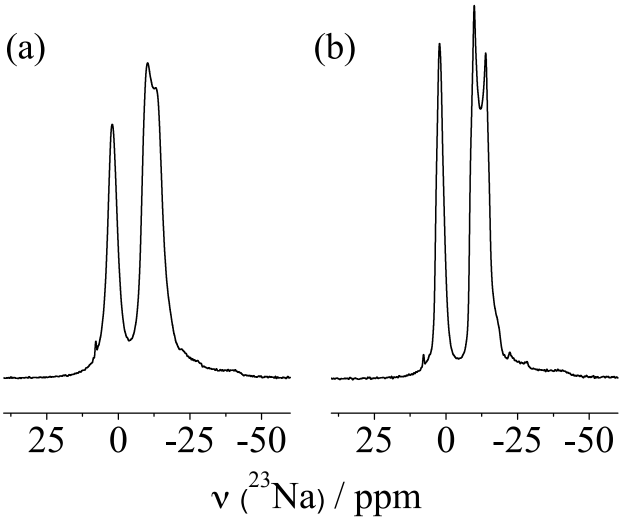

Figure 6.9: The ^{23}Na MAS NMR spectrum of cryolite (a) without and (b) with ^{19}F decoupling at 9.4 T magnetic field and 12 kHz MAS frequency. The decoupling method employed was SW$_f$-SPINAL.

The ^{19}F decoupling for ^{23}Na MAS NMR (Figure 6.9) and 3QMAS (Figure 6.10) experiments was done at a Larmor frequency of $\nu_0(^{19}\text{F}) = 376.433$ MHz, with an RF strength of $\nu_1 \approx 50$ kHz. The 3QMAS two-pulse sequence described above was also used to assess the effect of various decoupling schemes by recording ^{23}Na 3Q-filtered spectra. This means looking only at the first t_1 slice of a full

3QMAS, to be able to compare decoupling efficiency quickly. This may be used to optimize the parameters governing the decoupling sequences, such as pulse durations, phase angles and sweep profiles by searching for the maximum intensity of the 3Q-filtered ^{23}Na signal. In Figure 6.11, the change of decoupling efficiency in dependence of the phase angle ϕ is plotted for the TPPM sequence [186]. It can be seen that the trend of intensities observed from the 3Q-filtered MAS spectra (F_2 traces) is very similar to that obtained from recording and comparing the F_1 traces of full 3QMAS spectra. Care needs to be taken that the F_2 traces shown in Figure 6.11(a) possess a sufficient signal-to-noise ratio to evaluate the influence of parameter change, which in practice means acquisition of more transients than one would use for a single slice in the full 3QMAS. For Figure 6.11(a), 2400 transients with a recycle delay of 2 s were acquired. This is however still much faster than the 360×128 transients required to obtain the F_1 slices shown in Figure 6.11(b).

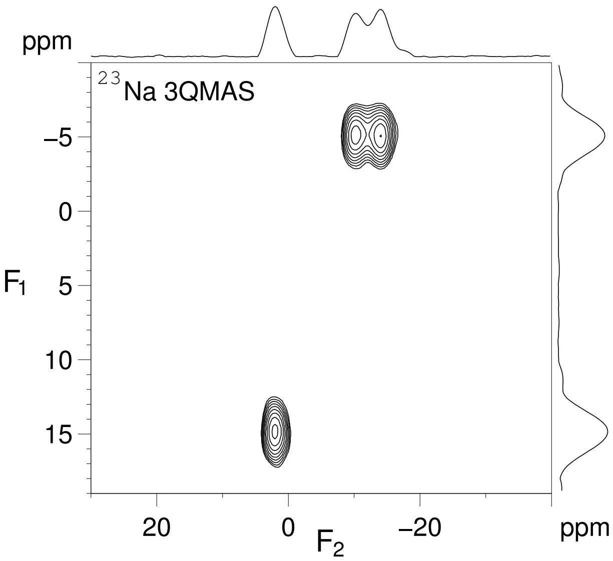

Figure 6.10: The ^{23}Na 3QMAS NMR spectrum of cryolite with ^{19}F decoupling at 9.4 T magnetic fieeld and 10 kHz MAS frequency. The decoupling method employed was SW$_f$-TPPM.

Using a combination of 3Q-filtered F_2 slices and acquisition of full 3QMAS spectra to compare F_1 slices, the following parameters were found to perform best for the respective sequences (pulse durations were identical for all sequences with $\tau_p = 8\ \mu$s):

- TPPM: phase angle $\phi = 7.5°$
- SPINAL-64: phase angle $\phi = 7.5°$, phase increments $\alpha = 5°$, $\beta = 10°$
- SW$_f$-TPPM: phase angle $\phi = 17.5°$; 11 pulse pairs with a sweep window from 0.78 to 1.22, using a linear sweep profile [26].
- SW$_f$-SPINAL: phase angle $\phi = 12.5°$; sweep over 16 pulse pairs (hence SW$_f$(32)-SPINAL-32 [27]), with a linear sweep from 0.90 to 1.10.

In Figure 6.9, the ^{23}Na NMR spectrum of cryolite (Na_3AlF_6) at 12 kHz MAS rate is shown with and without application of ^{19}F decoupling. The small impurity signals appearing in the ^{23}Na NMR spectra are likely due to small amounts of different sodium fluoro-aluminate species [187]. As can be seen from Figure 6.9(b),

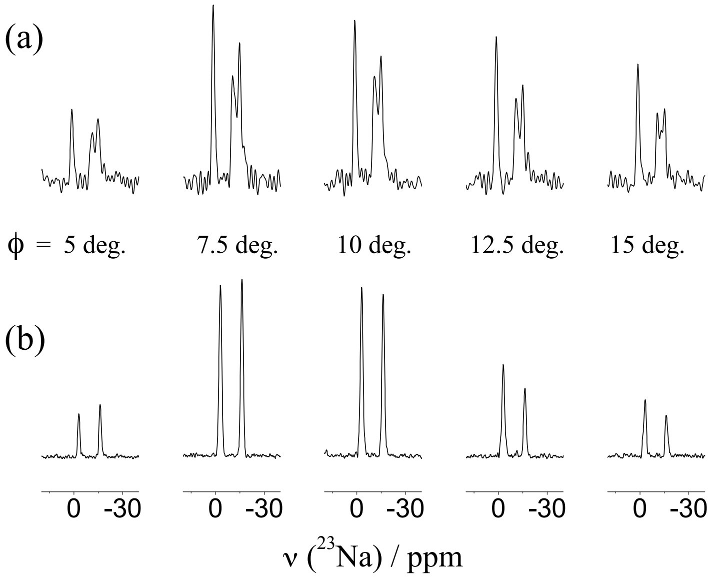

Figure 6.11: Comparison of ^{19}F decoupling efficiency of TPPM using the indicated phase angles ϕ at 10 kHz MAS frequency. (a) ^{23}Na 3Q-filtered spectra (F_2 traces), using a 3Q evolution time of $t_1 = 10\mu$s, with 2400 transients acquired. (b) ^{23}Na isotropic (F_1) projections of full 3QMAS spectra (360×128 transients acquired).

the ^{19}F decoupled spectrum (at a comparatively small decoupling field strength of $\nu_1 \approx 50$ kHz) exhibits better resolution than the non-decoupled one. From the atomic coordinates determined by single crystal XRD [188], the largest Na–F dipolar coupling present in cryolite is about 2.7 kHz. However, even at 12 kHz MAS the effects of dipolar coupling do not vanish completely, as cross-terms between dipolar, ^{23}Na and ^{19}F chemical shift interaction may cause broadening. Application of ^{19}F decoupling is instrumental in this case to reduce the effects of the cross-terms and to observe ^{23}Na in good resolution. A number of studies on polycrystalline cryolite using ^{23}Na MAS and 3QMAS NMR have been reported [189–192], but ^{19}F decoupling seems to have been applied in inconsistent fashion. MQMAS spectra may especially benefit from decoupling, because of the p-fold magnification of de-phasing, as shown in Appendix A. The full ^{23}Na 3QMAS spectrum of cryolite at 10 kHz MAS is shown in Figure 6.10, which has been recorded under SW$_f$-TPPM decoupling for both 3Q evolution delay and signal acquisition. The two crystallographically different ^{23}Na sites are observed to be well resolved in the isotropic (F_1) dimension of the 3QMAS spectrum, and

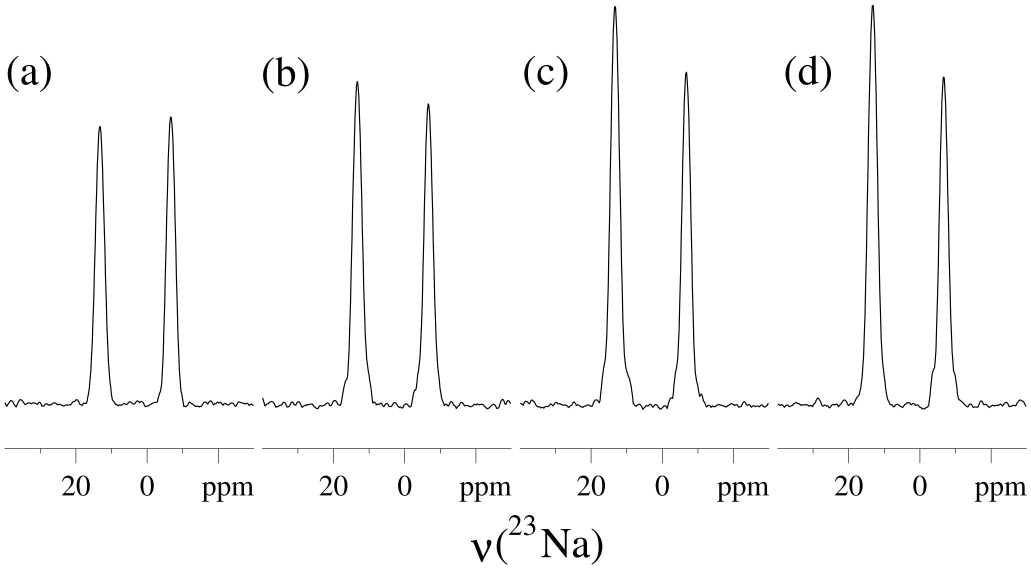

Figure 6.12: Comparison of ^{23}Na 3QMAS isotropic (F_1) projections of cryolite with (a) TPPM, (b) SPINAL-64, (c) SW$_f$-TPPM, (d) SW$_f$(32)-SPINAL-32 methods at MAS frequency of 10 kHz in a 9.4 T magnetic field.

are approaching the expected 1:1 intensity ratio.

The quality of the achieved decoupling differs substantially for the investigated sequences TPPM, SPINAL, SW$_f$-TPPM and SW$_f$-SPINAL [186]. This can be seen in Figure 6.12, where the F_1 traces of full 3QMAS spectra acquired with the respective decoupling schemes are compared. The adjustable parameters of these sequences have been optimized by acquiring a t_1 slice with a short evolution delay. In the comparison shown in Figure 6.12, SW$_f$-TPPM and SW$_f$-SPINAL are found to be performing much better than TPPM and SPINAL. The differences in decoupling efficiency between frequency-swept and non-swept sequences are larger than those observed for ^{19}F decoupling of spin-1/2 systems [110]. This could be attributed to 3-fold de-phasing experienced by the 3Q coherences during the 3Q evolution period. When acquiring one t_1 only with short evolution delay, the relative differences are much smaller, as can be seen from the comparison in Figure 6.11. The F_1 traces of full 3QMAS spectra display much stronger differences as they also include longer t_1 evolution times during which de-phasing occurs. This appears to amplify the efficiency edge held by the frequency-swept schemes over the non-swept ones. In summary, for systems with ^{19}F coupled to quadrupolar nuclei with half-integer spin, the frequency-swept sequences are the decoupling methods of choice [186].

Chapter 7

Conclusions

This thesis describes development and applications of heteronuclear spin decoupling methods in solid-state NMR. Spin decoupling is a very important tool in solid-state NMR to yield high-resolution. To understand the process of decoupling, a basic knowledge of the NMR phenomena is necessary. The Introduction (Chapter 1) of this thesis describes the basic principles of NMR, and the NMR interactions. Most of the anisotropic NMR interactions can be averaged by the mechanical motion of magic-angle spinning (MAS). The heteronuclear dipolar coupling frequently contributes to NMR line-widths in solid samples. This is the situation when one wants to observe a rare spin (S) nucleus which is dipolar coupled to an abundant spin (I) nucleus. Heteronuclear decoupling helps in this case, by spin-space-averaging of the dipolar interaction with radio-frequency (RF) irradiation.

Chapter 2 discusses different heteronuclear decoupling methods, their design and the factors affecting the efficiency of them. This chapter also discusses the different contributions to residual line width in solid-state NMR. Spin decoupling becomes highly necessary, when there is second-order recoupling interaction between the I spin chemical shielding tensor and the $I - S$ heteronuclear dipolar coupling, which cannot be averaged by MAS alone. The second-order term being the main line-broadening factor under CW decoupling, it is necessary to have symmetric multi-pulse sequences, which can provide two effective fields simultaneously to ensure a strong decoupling limit and avoid recoupling effects. The popular multi-pulse decoupling methods thus introduced were Two-Pulse Phase

Modulation (TPPM) and Small Phase Incremental ALteration (SPINAL). Also, the chapter discusses off-resonance behavior of spin decoupling. Although there was large improvement in the decoupling efficiency with TPPM and SPINAL, the insensitivity to NMR parameter changes (like the frequency offset, pulse duration, pulse phase, RF strength etc.) did not improve largely.

The third chapter (Chapter 3) describes the recently introduced frequency-swept SW$_f$-TPPM method, which shows much improved decoupling efficiency as well as robustness towards NMR parameter changes. In all investigated spin systems, SW$_f$-TPPM outperformed TPPM and SPINAL by consistent margins in decoupling efficiency. The method of frequency-sweep and the design of the pulse sequences are described in detail in this chapter. The manner of incrementing the multiplying factors on the train of TPPM pulse pairs describes the sweep profile. A tangential sweep profile was used when the SW$_f$-TPPM sequence was introduced. This chapter discusses the fact that the decoupling performance of a SW$_f$-TPPM sequence with a linear sweep profile is equivalent or even better than that with the tangential profiles, in the light of experimental evidences supported by numerical calculations. All the experiments were based on proton decoupling efficiencies. Furthermore, the independence of sweep direction in the performance of ^{1}H decoupling in the case of SW$_f$-TPPM methods is proven experimentally and with the help of numerical simulations. A Floquet theoretical approach to understand the improved efficiency of frequency-swept spin decoupling is also presented in this chapter.

A new heteronuclear decoupling scheme named SW$_f$-SPINAL is introduced in Chapter 4. The idea of frequency sweep used in SW$_f$-TPPM method is adapted to the SPINAL sequence here. This improved the spin decoupling performance of the sequence considerably, irrespective of the type of sweep. Many sweep variants of SW$_f$-SPINAL (with linear sweep profile) method were designed and tested, for rigid organic solids and for liquid crystals. The best performing sequence was SW$_f$(32)-SPINAL-32, which has a single frequency sweep over 32 pulse pairs of SPINAL-32 sequence. The SW$_f$-SPINAL is one of the best sequences now available for spin decoupling in oriented media like liquid crystals and biological membranes. Here also, all the decoupling experiments and simulations were based on the proton decoupling efficiencies of the sequences.

^{19}F decoupling efficiencies of decoupling sequences are compared, with a special emphasis given to the frequency swept methods, in Chapter 5. ^{19}F decoupling is considered to be more challenging than ^{1}H decoupling, because of large ^{19}F chemical shielding effects. For ^{19}F, SW$_f$-TPPM and SW$_f$-SPINAL sequences outperformed the conventional non-swept TPPM and SPINAL sequences in decoupler efficiency and robustness towards NMR parameter changes. This is evidenced from the ^{19}F decoupling experiments done in perfluoro-organic solids, and with the help of numerical simulations. Again, the SW$_f$(32)-SPINAL-32 sequence with a linear sweep is found to best performing among the SW$_f$-SPINAL sequences, with a 11-pulse SW$_f$-TPPM sequence with a linear sweep delivering the best observed decoupling overall. The independence of frequency sweep direction is also found in the case of ^{19}F decoupling with SW$_f$-TPPM method.

A conceptually different spin system of a half-integer spin quadrupolar nucleus dipolar-coupled to a spin-half nucleus is considered in Chapter 6 to study the effects of decoupling the quadrupolar nucleus. The effects of ^{1}H decoupling were checked with a powder sample of scandium sulphate pentahydrate (ScSPH), for acquisition of the ^{45}Sc signal. Polycrystalline cryolite (Na_3AlF_6) was used as the model compound to study the effects of ^{19}F decoupling while observing ^{23}Na. In both cases, the MAS NMR did not show much improvement under spin decoupling. But the high resolution technique multiple-quantum magic-angle spinning (MQMAS) benefitted considerably from heteronuclear spin decoupling. This is so since MQ coherence of order p will undergo p-fold de-phasing during the MQ evolution period, thus magnifying the effect of dipolar couplings on the spectrum. Both SW$_f$-SPINAL and SW$_f$-TPPM were highly efficient in ^{1}H and ^{19}F decoupling of MQMAS spectra. This is evidenced by the experimental results of ^{1}H decoupling of ^{45}Sc 3QMAS and 5QMAS experiments on ScSPH and ^{19}F decoupling of ^{23}Na 3QMAS of cryolite.

In summary, this thesis describes advanced heteronuclear spin decoupling methods, which are highly efficient and robust, and are able to replace the widely applied TPPM and SPINAL methods. Moreover, the methods suggested in this thesis are experimentally proven to perform efficiently in a variety of chemical systems, like rigid organic solids, liquid crystals, inorganic salts, solids containing quadrupolar nuclei etc. These experimental observations are supported by extensive numerical simulations, which also gave clear evidence of the superiority of the SW_f-TPPM and SW_f-SPINAL methods over the conventional, previously suggested TPPM and SPINAL schemes.

Besides the method-oriented studies of decoupling sequences, we have also determined the NMR parameters (chemical shift and quadrupolar interaction) of some inorganic compounds, namely scandium sulphate pentahydrate (ScSPH, $Sc_2(SO_4)_3.5H_2O$), aluminium carbide (Al_4C_3), strontium aluminate ($SrAl_{12}O_{19}$) and aluminium oxide in an organic matrix (Al_2O_3 in spider silk). For both ScSPH and Al_4C_3, DFT calculations based on the reported X-ray structures of these compounds were also performed. Comparison of DFT results to NMR experimental data for ^{27}Al and ^{45}Sc allowed the assignment of the NMR resonances to the structural sites.

Appendix

Spin Decoupling during MQ Evolution

A system of a nucleus with spin $I = \frac{3}{2}$ (such as ^{11}B or ^{23}Na) dipolar coupled with a nucleus with spin $I = \frac{1}{2}$ (such as ^{1}H or ^{19}F) is considered. The spin states of these nuclei are given by the magnetic quantum numbers m_I and m_S, which are coded in the following way:

$$\begin{aligned} m_I &= +\frac{3}{2} =: |\gamma\rangle \\ m_I &= +\frac{1}{2} =: |\alpha\rangle \qquad m_S = +\frac{1}{2} =: |\alpha\rangle \\ m_I &= -\frac{1}{2} =: |\beta\rangle \qquad m_S = -\frac{1}{2} =: |\beta\rangle \\ m_I &= -\frac{3}{2} =: |\delta\rangle \end{aligned} \tag{1}$$

The state function for the two nuclei is given by:

$$\begin{aligned} \Psi_{I,S} &= \sum_{m_I=-\frac{3}{2}}^{m_I=+\frac{3}{2}} \sum_{m_I=-\frac{1}{2}}^{m_I=+\frac{1}{2}} c_{m_I,m_S} |m_I m_S\rangle \\ &= \sum_{m_I=-\frac{3}{2}}^{m_I=+\frac{3}{2}} \left(c_{m_I,\beta}|m_I\beta\rangle + c_{m_I,\alpha}|m_I\alpha\rangle\right) \end{aligned} \tag{2}$$

In a strong external magnetic field, the principal interaction is described by the Zeeman Hamiltonian:

$$\hat{\mathscr{H}}_{IS}^{Z} = \omega_0^I \hat{I}_{Iz} + \omega_0^S \hat{I}_{Sz} \tag{3}$$

with ω_0^I and ω_0^S being the Larmor frequencies of spin I and S respectively. The energy levels of the Zeeman interaction are given by the diagonal elements of the matrix representation of $\hat{\mathscr{H}}_{IS}^{Z}$ i.e., $\langle m_I m_S|\hat{\mathscr{H}}_{IS}^{Z}|m_I m_S\rangle$. The eigenvalue equations of $\hat{I}_{Sz}$ and $\hat{I}_{Iz}$ are:

$$\hat{I}_{Sz}|\alpha\rangle = +\frac{1}{2}|\alpha\rangle \quad \hat{I}_{Sz}|\beta\rangle = -\frac{1}{2}|\beta\rangle \tag{4}$$

$$\begin{aligned} \hat{I}_{Iz}|\alpha\rangle = +\frac{1}{2}|\alpha\rangle \quad \hat{I}_{Iz}|\beta\rangle = -\frac{1}{2}|\beta\rangle \\ \hat{I}_{Iz}|\gamma\rangle = +\frac{3}{2}|\gamma\rangle \quad \hat{I}_{Iz}|\delta\rangle = -\frac{3}{2}|\delta\rangle \end{aligned} \tag{5}$$

For a spin state $|m_I m_S\rangle$ the Zeeman energy is therefore given by:

$$\langle m_I m_S|\hat{\mathscr{H}}^Z_{IS}|m_I m_S\rangle = m_I\omega^I_0 + m_S\omega^S_0 \tag{6}$$

The energy level sequence resulting from only the Zeeman interaction is shown

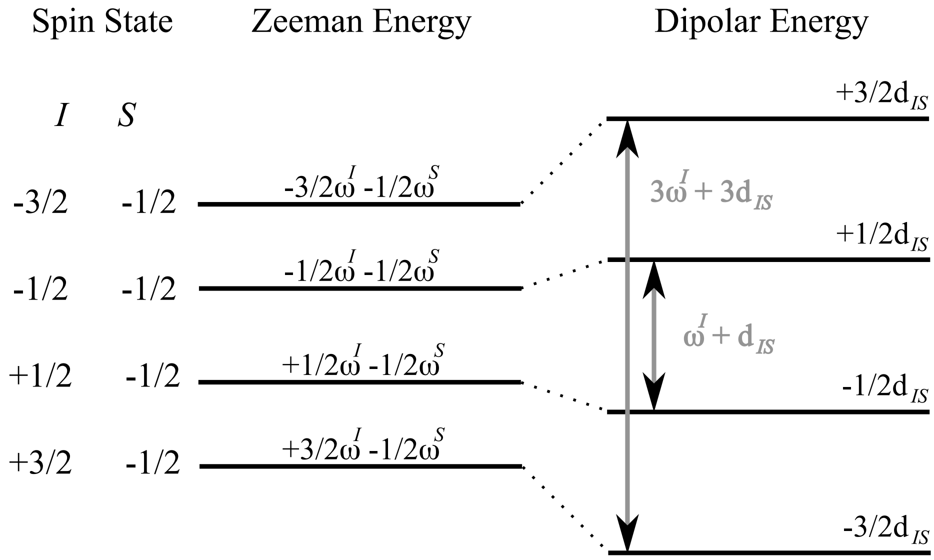
Spin State
Zeeman Energy
Dipolar Energy
I
S
-3/2
-1/2
-1/2
-1/2
+1/2
-1/2
+3/2
-1/2
-3/2ω^I -1/2ω^S
-1/2ω^I -1/2ω^S
+1/2ω^I -1/2ω^S
+3/2ω^I -1/2ω^S
+3/2d_IS
+1/2d_IS
-1/2d_IS
-3/2d_IS
3ω^I + 3d_IS
ω^I + d_IS

Figure 1: (Appendix): Schematic representation of the energy levels of two dipolar coupled spins $I = \frac{3}{2}$ and $I = \frac{1}{2}$, showing the modification of the energy levels by the dipolar interaction (only the branch with $m_S = -\frac{1}{2}$). The triple-quantum transition is affected three times as much as the single-quantum transition by the secular dipole–dipole coupling d_{IS}. For clarity, effect of the quadrupolar interaction is omitted in this graphics.

on the left-hand side of Figure 1. If dipolar interaction is present in the system, it will modify the Zeeman energy levels. In the secular (high-field) approximation, the dipolar interaction between the two nuclei I and S is described by the heteronuclear dipolar Hamiltonian:

$$\hat{\mathscr{H}}_{IS}^{D} = d_{IS} 2\hat{I}_{Iz}\hat{I}_{Sz} \tag{7}$$

Here, d_{IS} is the orientation-dependent secular dipole–dipole coupling [5]. It depends on the angle θ_{IS} between the vector connecting the two spins and the external magnetic field, the gyro-magnetic ratios γ_i of the involved nuclei, and the distance r_{IS} between the spins. In units of Hertz, d_{IS} is given by:

$$d_{IS} = -\frac{\mu_0}{8\pi^2}\frac{\gamma^I\gamma^S\hbar}{r_{IS}^3}\frac{(3cos^2\theta_{IS} - 1)}{2} \tag{8}$$

The dipolar interaction modifies the energy levels of the system by

$$\langle m_I m_S|\hat{\mathscr{H}}_{IS}^{Z}|m_I m_S\rangle = d_{IS} 2 m_I m_S \tag{9}$$

These modifications of the Zeeman levels are displayed schematically in Figure 1. It may also be seen from Figure 1 that for a one-quantum transition of spin I (such as the central transition of ^{23}Na), the energy level difference is changed by the dipolar interaction by d_{IS}, whereas the triple-quantum transition changes by $3d_{IS}$. More general, for a p quantum transition, the resonance frequency of spin I is given by:

$$\begin{aligned} \omega_p^I &= p\omega_0^I - 2m_s p d_{IS} \\ &= p\omega_0^I \pm p d_{IS} \end{aligned} \tag{10}$$

Here, the term $+pd_{IS}$ applies for spin states with $m_S = -\frac{1}{2}$ (as shown in Figure 1), and $-pd_{IS}$ applies for $m_S = +\frac{1}{2}$. The spectral line broadening caused by the orientation dependence of d_{IS} is thus proportional to p. The above relation is also valid for higher spin numbers like ^{27}Al ($I = \frac{5}{2}$) coupled to a nucleus with $I = \frac{1}{2}$.

For clarity, the quadrupolar effects on the energy levels of spin I have been omitted in this derivation. To first order, the quadrupolar interaction is easily taken into account also in the simple energy level picture. The quadrupolar interaction ω_Q is strongest when the principal axis associated with the largest eigenvalue of the quadrupolar coupling tensor is aligned with the external magnetic field, and may be expressed by [133, 135]:

$$\omega_Q = \frac{3e^2qQ}{\hbar 2I(2I-1)} \tag{11}$$

For $I = \frac{3}{2}$, the $m_I = -\frac{3}{2} \rightarrow -\frac{1}{2}$ transition is modified by $-\omega_Q$, and the $m_I = +\frac{1}{2} \rightarrow +\frac{3}{2}$ transition by $+\omega_Q$, while leaving the central transition ($m_I = -\frac{1}{2} \rightarrow +\frac{1}{2}$) unaffected. The relative frequencies of single- and triple-quantum transitions shown in Figure 1 thus remain the same, as the contributions of ω_Q cancel. The expositions of Duer [174] and Friedrich et al. [175] are more complex, as they additionally include the effects of magic-angle spinning. In these derivations [174, 175], the quadrupolar interaction is also considered to first order only, but the same result of p-fold amplification of the dipolar interaction for a p quantum transition is obtained. Because of the p-fold dephasing, application of spin decoupling sequences is especially important for MQMAS experiments.

References

[1] E. M. Purcell, H. C. Torrey and R. V. Pound. Resonance absorption by nuclear magnetic moments in a solid. *Phys. Rev.* 69 (1946) 37–38.

[2] F. Bloch, W. W. Hansen, and M. Packard. Nuclear induction. *Phys. Rev.* 69 (1946) 127–127.

[3] A. Abragam. *The Principles of Nuclear Magnetism.* Oxford Press (1961).

[4] H. Günther. *NMR Spectroscopy: Basic Principles, Concepts, and Applications in Chemistry.* Wiley (1995).

[5] M. H. Levitt. *Spin Dynamics: Basics of Nuclear Magnetic Resonance.* Wiley (2001).

[6] M. Mehring. *High Resolution NMR Spectroscopy in Solids.* Springer-Verlag, Germany (1976).

[7] M. J. Duer. *Introduction to Solid-State NMR.* Blackwell Sciences, U.K. (2002).

[8] D. D. Laws, H. M. L. Bitter, and A. Jerschow. Solid-state NMR spectroscopic methods in chemistry. *Angew. Chem. Int. Ed.* 41 (2002) 3096–3129.

[9] P. Zeeman. The effect of magnetisation on the nature of light emitted by a substance. *Nature* 55 (1897) 347–347.

[10] R. K. Harris, E. D. Becker, S. M. C. de Menezes, R. Goodfellow and P. Granger. NMR nomenclature: Nuclear spin properties and conventions for chemical shifts (IUPAC recommendations 2001). *Concepts Magn. Reson.* 14 (2002) 326–346.

[11] F. Bloch. Nuclear induction. *Phys. Rev.* 70 (1946) 460–473.

[12] W. C. Dickinson. Dependence of the ^{19}F nuclear resonance position on chemical compound. *Phys. Rev.* 77 (1950) 736–737.

[13] W. G. Proctor and F. C. Yu. The Dependence of a nuclear magnetic resonance frequency upon chemical compound. *Phys. Rev.* 77 (1950) 717–717.

[14] G. E. Pake. Nuclear resonance absorption in hydrated crystals: fine structure of the proton line. *J. Chem. Phys.* 16 (1948) 327–336.

[15] T. Gullion and J. Schaefer. Rotational-echo double-resonance NMR. *J. Magn. Reson.* 81 (1989) 196–200.

[16] T. Gullion and J. Schaefer. Detection of weak heteronuclear dipolar coupling by rotational-echo double-resonance nuclear magnetic resonance. *Adv. Magn. Reson.* 13 (1989) 57–83.

[17] D. Massiot, F. Fayon, M. Deschamps, S. Cadars, P. Florian, V. Montouillout, N. Pellerin, J. Hiet, A. Rakhmatullin and C. Bessada. Detection and use of small J couplings in solid state NMR experiments. *C. R. Chim.* 13 (2010) 117–129.

[18] T. Bräuniger, S. Ghedia and M. Jansen. Covalent bonds in α-SnF$_2$ monitored by J-couplings in solid-state NMR spectra. *Z. Anorg. Allg. Chem.* 636 (2010) 2399–2404.

[19] E. R. Andrew, A. Bradbury and R. G. Eades. Nuclear magnetic resonance spectra from a crystal rotated at high speed. *Nature* 182 (1958) 1659–1659.

[20] M. Ernst, S. Bush, A. C. Kolbert, and A. Pines. Second-order recoupling of chemical-shielding and dipolar-coupling tensors under spin decoupling insolid-state NMR. *J. Chem. Phys.* 105 (1996) 3387–3397.

[21] D. B. Zax. Field-dependent isotropic shifts and limitations to linewidths in solid state nuclear magnetic resonance: A Floquet treatment. *J. Chem. Phys.* 105 (1996) 6616–6625.

[22] F. Bloch. Line narrowing by double-frequency irradiation . *Phys. Rev.* 93 (1954) 944–945.

[23] A. L. Bloom and J. N. Shoolery. Effects of perturbing radiofrequency fields on nuclear spin coupling. *Phys. Rev.* 97 (1955) 1261–1265.

[24] F. Bloch. Theory of line narrowing by double-frequency irradiation. *Phys. Rev.* 111 (1958) 841–853.

[25] L. R. Sarles and R. M. Cotts. Double nuclear magnetic resonance and the dipole interaction in solids. *Phys. Rev.* 111 (1958) 853–859.

[26] S. R. Hartmann and E. L. Hahn. Nuclear double resonance in the rotating frame. *Phys. Rev.* 128 (1962) 2042–2053.

[27] A. Pines, M. G. Gibby and J. S. Waugh. Proton-enhanced NMR of dilute spins in solids. *J. Chem. Phys.* 59 (1973) 569–590.

[28] E. O. Stejskal, J. Shaefer and J. S. Waugh. Magic-angle spinning and polarization transfer in proton-enhanced NMR. *J. Magn. Reson.* 28 (1977) 105–112.

[29] P. K. Madhu. High-resolution solid-state NMR spectroscopy of protons with homonuclear dipolar decoupling schemes under magic-angle spinning. *Solid State Nucl. Magn. Reson.* 35 (2009) 2–11.

[30] M. Lee and W. I. Goldburg. Nuclear-magnetic-resonance line narrowing by a rotating rf field. *Phys. Rev.* 140 (1965) A1261–A1271.

[31] M. Mehring and J. S. Waugh. Magic-angle NMR experiments in solids. *Phys. Rev. B* 5 (1965) 3459–3471.

[32] E. Vinogradov, P. K. Madhu and S. Vega. High-resolution proton solid-state NMR spectroscopy by phase-modulated Lee-Goldburg experiment. *Chem. Phys. Lett.* 314 (1999) 443–450.

[33] J. S. Waugh, L. M. Huber and U. Haeberlen. Approach to high-resolution NMR in solids. *Phys. Rev. Lett.* 20 (1968) 180–182.

[34] P. Mansfeld. Symmetrized pulse sequences in high resolution NMR in solids. *J. Phys. C* 4 (1971) 1444–1452.

[35] D. Burum and W. K. Rhim. Analysis of multiple pulse NMR in solids. III. *J. Chem. Phys.* 71 (1979) 944–956.

[36] K. Takegoshi and C. A. McDowell. A “magic echo” pulse sequence for the high-resolution NMR spectra of abundant spins in solids. *Chem. Phys. Lett.* 116 (1985) 100–104.

[37] M. Hohwy and N. C. Nielsen. Elimination of high order terms in multiple pulse nuclear magnetic resonance spectroscopy: Application to homonuclear decoupling in solids. *J. Chem. Phys.* 106 (1997) 7571–7586.

[38] M. Levitt. Symmetry-based pulse sequences in magic-angle spinning solid-state NMR. *Encyc. Nucl. Magn. Reson.* 9 (2002) 165–196.

[39] S. Paul, R. S. Thakur and P. K. Madhu. ^{1}H homonuclear dipolar decoupling at high magic-angle spinning frequencies with rotor-synchronised symmetry sequences. *Chem. Phys. Lett.* 456 (2000) 253–256.

[40] D. Sakellariou, A. Lesage, P. Hodgkinson and L. Emsley. Homonuclear dipolar decoupling in solid-state NMR using continuous phase modulation. *Chem. Phys. Lett.* 319 (2000) 253–260.

[41] M. H. Levitt, R. Freeman and T. Frenkiel. *Advances in Magnetic Resonance, Vol. 11.* Academic Press, New York (1982).

[42] A. J. Shaka, J. Keeler, T. Frenkiel and R. Freeman. An improved sequence for broadband decoupling: WALTZ-16. *J. Magn. Reson.* 52 (1983) 335–338.

[43] A. J. Shaka, P. B. Barker and R. Freeman. Computer-optimized decoupling scheme for wideband applications and low-level operation. *J. Magn. Reson.* 64 (1985) 547–552.

[44] A. J. Shaka, C. J. Lee and A. Pines. Iterative schemes for bilinear operators; application to spin decoupling. *J. Magn. Reson.* 77 (1988) 274–293.

[45] E. Kupce and R. Freeman. Adiabatic pulses for wideband inversion and broadband decoupling. *J. Magn. Reson.* 64 (1985) 547–552.

[46] E. L. Hahn. Spin echoes. *Phys. Rev.* 80 (1950) 580–594.

[47] H. Y. Carr and E. M. Purcell. Effects of diffusion on free precession in nuclear magnetic resonance experiments. *Phys. Rev.* 94 (1954) 630–638.

[48] S. Meiboom and D. Gill. Modified spin-echo method for measuring nuclear relaxation times. *Rev. Scientific Instruments* 29 (1958) 688–691.

[49] M. Mehring, G. Sinning and A. Pines. NMR line broadening in solids by slowing down of spin fluctuations. *Z. Phys. B.* 24 (1976) 73–76.

[50] G. Sinning, M. Mehring and A. Pines. Dynamics of spin decoupling in carbon-13–proton NMR. *Chem. Phys. Lett.* 43 (1976) 382–386.

[51] M. Mehring and G. Sinning. Dynamics of heteronuclear spin coupling and decoupling in solids. *Phys. Rev. B.* 15 (1977) 2519–2532.

[52] I. J. Shannon, K. D. M. Harris and S. Arumugan. High-resolution solid state ^{13}C NMR studies of ferrocene as a function of magic angle sample spinning frequency. *Chem. Phys. Lett.* 196 (1992) 588–594.

[53] D. L. Vanderhart, W. L. Earl and A. N. Garroway. Resolution in ^{13}C NMR of organic solids using high-power proton decoupling and magic-angle sample spinning. *J. Magn. Reson.* 44 (1981) 361–401.

[54] M. Ernst, H. Zimmermann and B. H. Meier. A simple model for heteronuclear spin decoupling in solid-state NMR. *Chem. Phys. Lett.* 162 (2003) 1–34.

[55] M. Ernst. Heteronuclear spin decoupling in solid-state NMR under magic-angle sample spinning. *J. Magn. Reson.* 162 (2003) 1–34.

[56] P. Hodgkinson. Heteronuclear decoupling in the NMR of solids. *Prog. Nucl. Magn. Reson. Spectrosc.* 46 (2005) 197–222.

[57] A. E. Bennett, C. M. Rienstra, M. Auger, K. V. Lakshmi and R. G. Griffin. Heteronuclear decoupling in rotating solids. *J. Chem. Phys.* 16 (1995) 6951–6958.

[58] B. M. Fung, A. K. Khitrin and K. Ermolaev. An improved broadband decoupling for liquid crystals and solids. *J. Magn. Reson.* 142 (2000) 97–101.

[59] T. Bräuniger, P. Wormald and P. Hodgkinson. Improved proton decoupling in NMR spectroscopy of crystalline solids using the SPINAL-64 sequence. *Monatsh. Chem.* 133 (2002) 1549–1554.

[60] G. de Paëpe, A. Lesage and L. Emsley. The performance of phase modulated heteronuclear dipolar decoupling schemes in fast magic-angle-spinning nuclear magnetic resonance experiments. *J. Chem. Phys.* 119 (2003) 4833–4841.

[61] P. Tekely, P. Palmas and D. Canet. Effect of proton spin exchange on the residual ^{13}C MAS NMR linewidths. Phase-modulated irradiation for efficient heteronuclear decoupling in rapidly rotating solids. *J. Magn. Reson. A* 107 (1994) 129–133.

[62] A. Detken, E. H. Hardy, M. Ernst and B. H. Meier. Simple and efficient decoupling in magic-angle spinning solid-state NMR: the XiX scheme. *Chem. Phys. Lett.* 356 (2002) 298–304.

[63] Z. Gan and R. R. Ernst. Frequency- and phase-modulated heteronuclear decoupling in rotating solids. *Solid State Nucl. Magn. Reson.* 8 (1997) 153–159.

[64] G. D. Paëpe, B. Elèna and L. Emsley. Characterization of heteronuclear decoupling through proton spin dynamics in solid-state nuclear magnetic resonance spectroscopy. *J. Chem. Phys.* 121 (2004) 3165–3180.

[65] R. Fu. Efficient heteronuclear dipolar decoupling in NMR of static solid samples using phase-wiggled two-pulse phase modulation. *Chem. Phys. Lett.* 483 (2009) 147–153.

[66] S. Paul. V. S. Mithu, N. D. Kurur and P. K. Madhu. Efficient heteronuclear dipolar decoupling in solid-state nuclear magnetic resonance at rotary resonance conditions. *J. Magn. Reson.* 203 (2009) 199–202.

[67] I. Scholz, P. Hodgkinson, B. H. Meier and M. Ernst. Understanding two-pulse phase-modulated decoupling in solid-state NMR. *J. Chem. Phys.* 130 (2009) 114510-1–114510-17.

[68] M. Eden and M. H. Levitt. Pulse sequence symmetries in the nuclear magnetic resonance of spinning solids: application to heteronuclear decoupling. *J. Chem. Phys.* 111 (1999) 1511–1519.

[69] J. Leppert, O. Ohlenschläger, M. Görlach, and R. Ramachandran. Adiabatic heteronuclear decoupling in rotating solids. *J. Biomol. NMR* 29 (2004) 319–324.

[70] M. Weingarth, P. Tekely and G. Bodenhausen. Efficient heteronuclear decoupling by quenching rotary resonance in solid-state NMR. *Chem. Phys. Lett.* 466 (2008) 247–251.

[71] X. Filip, C. Tripon and C. Filip. Heteronuclear decoupling under fast MAS by a rotor-synchronized Hahn-echo pulse train. *J. Magn. Reson.* 176 (2005) 239–243.

[72] R. S. Thakur, N. D. Kurur and P. K. Madhu. Swept-frequency two-pulse phase modulation for heteronuclear dipolar decoupling in solid-state NMR. *Chem. Phys. Lett.* 426 (2006) 459–463.

[73] C. V. Chandran and T. Bräuniger. Efficient heteronuclear dipolar decoupling in solid-state NMR using frequency-swept SPINAL sequences. *J. Magn. Reson.* 200 (2009) 226–232.

[74] M. Leskes, R. S. Thakur, P. K. Madhu, N. D. Kurur and S. Vega. Bimodal Floquet description of heteronuclear dipolar decoupling in solid-state nuclear magnetic resonance. *J. Chem. Phys.* 127 (2007) 24501-1–24501-17.

[75] T. G. Oas, R. G. Griffin and M. H. Levitt. Rotary resonance recoupling of dipolar interactions in solid-state nuclear magnetic resonance spectroscopy. *J. Chem. Phys.* 89 (1988) 692–695.

[76] N. C. Nielsen, H. Bildsøe, H. J. Jacobsen and M. H. Levitt. Double-quantum homonuclear rotary resonance: Efficient dipolar recovery in magic-angle spinning nuclear magnetic resonance. *J. Chem. Phys.* 101 (1994) 1805–1812.

[77] D. L. VanderHart and G. C. Campbell. Off-resonance proton decoupling on-resonance and near-resonance. *J. Magn. Reson.* 134 (1998) 88–112.

[78] R. S. Thakur, N. D. Kurur and P. K. Madhu. Analysis of phase-modulated heteronuclear dipolar decoupling sequences in solid-state nuclear magnetic resonance. *J. Magn. Reson.* 193 (2008) 77–88.

[79] R. S. Thakur, N. D. Kurur and P. K. Madhu. An experimental study of decoupling sequences for multiple-quantum and high-resolution MAS experiments in solid-state NMR. *Magn. Reson. Chem.* 46 (2008) 166–169.

[80] R. S. Thakur, N. D. Kurur and P. K. Madhu. Improved heteronuclear dipolar decoupling sequences for liquid-crystal NMR. *J. Magn. Reson.* 185 (2007) 264–269.

[81] C. V. Chandran, P. K. Madhu, N. D. Kurur and T. Bräuniger. Swept-frequency two-pulse phase modulation (SW$_f$TPPM) sequences with linear sweep profile for heteronuclear decoupling in solid-state NMR. *Magn. Reson. Chem.* 46 (2008) 943–947.

[82] M. Leskes, P. K. Madhu and S. Vega. Floquet theory in solid-state nuclaer magnetic resonance. *Prog. Nucl. Magn. Reson. Spectrosc.* 57 (2010) 345–380.

[83] S. Paul, C. V. Chandran, T. Bräuniger and P. K. Madhu. Sweep direction and efficiency of the swept-frequency two pulse phase modulated scheme for heteronuclear dipolar-decoupling in solid-state NMR. *J. Magn. Reson.* 209 (2011) 261–268.

[84] M. Veshtort and R. G. Griffin. SPINEVOLUTION: A powerful tool for the simulation of solid and liquid state NMR experiments. *J. Magn. Reson.* 178 (2006) 248–282.

[85] R. S. Thakur, N. D. Kurur and P. K. Madhu. Pulse duration and phase modulated heteronuclear dipolar decoupling schemes in solid-state NMR. *Proc. Ind. Nat. Sci. Acad.* Springer Verlag (2009).

[86] B. M. Fung. The effect of radio-frequency heating in carbon-13 NMR studies of liquid crystals. *J. Magn. Reson.* 86 (1990) 160–163.

[87] B. M. Fung. ^{13}C NMR studies of liquid crystals. *Prog. Nucl. Magn. Reson. Spectrosc.* 41 (2002) 171–186.

[88] S. V. Dvinskikh, K. Yamamoto, U. H. N. Dürr and A. Ramamoorthy. Sensitivity and resolution enhancement in solid-state NMR spectroscopy of bicelles. *J. Magn. Reson.* 184 (2007) 228–235.

[89] T. Schaller, D. B. Dingwell, H. Keppler, W. Knöller, L. Merwin and A. Sebald. Fluorine in silicate glasses: a multinuclear nuclear magnetic resonance study. *Geochim. Cosmochim. Acta* 56 (1992) 701–707.

[90] E. W. Hagaman. ^{13}C-^{19}F dipolar dephasing in monofluorinated organic substances. Characterization by ^{1}H-^{13}C-^{19}F triple-resonance ^{13}C CP/MAS and ^{19}F MAS NMR. *J. Magn. Reson.* 104 (1993) 125–131.

[91] M. Pruski, D. P. Lang, C. Fernandez and J. P. Amoureux. Multiple-quantum magic-angle spinning NMR with cross-polarization: Spectral editing of high-resolution spectra of quadrupolar nuclei. *Solid State Nucl. Magn. Reson.* 7 (1997) 327–331.

[92] B. Bureau, G. Silly and J. Y. Buzaré. CP-MAS ^{207}Pb with ^{19}F decoupling NMR spectroscopy: medium range investigation in fluoride materials. *Solid State Nucl. Magn. Reson.* 15 (1999) 79–89.

[93] P. Bertani, J. Raya, P. Reinheimer, R. Gougeon, L. Delmotte and J. Hirschinger. ^{19}F/^{29}Si distance determination on fluoride-containing octadecasil by Hartmann-Hahn cross-polarization under fast magic-angle spinning. *Solid State Nucl. Magn. Reson.* 13 (1999) 219–229.

[94] J. C. C. Chan and H. Eckert. High-resolution ^{27}Al-^{19}F solid-state double resonance NMR studies of AlF_3-BaF_2-CaF_2 glasses. *J. Non-Cryst. Solids* 284 (2001) 16–21.

[95] G. Scholz and O. Korup. High-energy ball milling - a possible synthesis route for cryolite and chiolite. *Solid State Sci.* 8 (2006) 678–684.

[96] J. Giraudet, M. Dubois, K. Guérin, A. Hamwi and F. Masin. Solid state NMR studies of covalent graphite fluorides $(CF)_n$ and $(C_2F)_n$. *J. Phys. Chem. Solids* 67 (2006) 1100–1105.

[97] L. Zhang, C. C. de Araujo and H. Eckert. Structural role of fluoride in aluminophosphate sol-gel glasses: high-resolution double-resonance NMR studies. *J. Phys. Chem. B* 111 (2007) 10402–10412.

[98] J. Giraudet, M. Dubois, K. Guérin, C. Delabarre, P. Pirotte, A. Hamwi and F. Masin. Heteronuclear dipolar recoupling using Hartmann-Hahn cross polarization: A probe for ^{19}F-^{13}C distance determination of fluorinated carbon materials. *Solid State Nucl. Magn. Reson.* 31 (2007) 131–140.

[99] F. J. Berry, E. Moore, M. Mortimer, X. Ren, R. Heap, P. Slater and M. F. Thomas. Synthesis and structural investigation of a new oxide fluoride of composition $Ba_2SnO_{2.5}F_3$. xH_2O ($x\approx$ 0.5). *J. Solid State Chem.* 181 (2008) 2185–2190.

[100] C. Serre, M. Haouas, F. Taulelle, W. Van Beek and G. Férey. Synthesis, structure and solid state NMR analysis of new templated titanium (III/IV) fluorophosphate. *C. R. Chim.* 13 (2010) 336–342.

[101] S. V. Dvinskikh, R. Sitnikov and I. Furó. ^{13}C PGSE NMR experiment with heteronuclear dipolar decoupling to measure diffusion in liquid crystals and solids. *J. Magn. Reson.* 142 (2000) 102–110.

[102] G. Silly, C. Legein, J. Y. Buzaré and F. Calvayrac. Electric field gradients in fluoride crystalline powders: correlation of NMR measurements with ab initio calculations. *Solid State Nucl. Magn. Reson.* 25 (2004) 241–251.

[103] M. Gerken, P. Hazendonk, J. Nieboer and G. J. Schrobilgen. NMR spectroscopic study of xenon fluorides in the gas phase and of XeF_2 in the solid state. *J. Fluorine Chem.* 125 (2004) 1163–1168.

[104] P. Florian, E. M. Anghel and C. Bessada. Structured description of the $Na_2B_4O_7$-Na_3AlF_6-TiO_2 system. 2. A multinuclear NMR approach of melts and solids. *J. Phys. Chem. B* 111 (2007) 968–978.

[105] A. Pawlik, R. König, G. Scholz, E. Kemnitz, G. Brunklaus, M. Bertmer and C. Jäger. Access to local structures of HS-AlF_3 and its precursor determined by high-resolution solid-state NMR. *J. Phys. Chem. C* 113 (2009) 16674–16680.

[106] P. K. Pallathadka, S. S. Tay, L. Tinaxi and P. Sprenger. Solid state ^{19}F NMR study of crystal transformation in PVDF and its nanocomposites. *Poly. Sci. Engg.* 46 (2006) 1684–1690.

[107] N. G. Karpukhina, U. W- Zwanziger, J. W. Zwanziger and A. A. Kiprianov. Preferential binding of fluorine to aluminium in high peralkaline aluminosilicate glasses. *J. Phys. Chem. B* 111 (2007) 10413–10420.

[108] S. Hoyer, T. Emmler and K. Seppelt. The structure of xenon hexafluoride in solid state. *J. Fluorine Chem.* 127 (2006) 1415–1422.

[109] B. Zhou, B. L. Sherriff, J. S. Hartman and G. Wu. ^{27}Al and ^{23}Na NMR spectroscopy and structural modeling of aluminofluoride minerals. *Am. Miner.* 92 (2007) 34–43.

[110] C. V. Chandran, P. K. Madhu, P. Wormald and T. Bräuniger. Frequency-swept pulse sequences for ^{19}F heteronuclear spin decoupling in solid-state NMR. *J. Magn. Reson.* 206 (2010) 255–263.

[111] G. Antonioli, D. E. McMillan and P. Hodgkinson. Line-splitting and broadening effects from ^{19}F in the ^{13}C NMR of liquid crystals and solids. *Chem. Phys. Lett.* 344 (2001) 68–74.

[112] J. C. Cherryman and R. K. Harris. New multinuclear experiments on solid organotin fluorides. *J. Magn. Reson.* 128 (1997) 21–29.

[113] A. Nordon, R. K. Harris, L. Yeo and K. D. M. Harris. Application of triple-channel ^{13}C{^{1}H, ^{19}F} NMR techniques to probe structural properties of disordered solids. *Chem. Comm.* 33 (1997) 2045–2046.

[114] R. K. Harris, A. Nordon and K. D. M. Harris. Ring inversion of fluorocyclohexane in its solid thiourea inclusion compound. *Magn. Reson. Chem.* 37 (1999) 15–24.

[115] R. K. Harris and L. A. Crowe. Solid-state NMR studies of fluorinated diazadiphosphetidines. *J. Chem. Soc., Dalton Trans.* 28 (1999) 4315–4323.

[116] M. Bechmann, K. Hain, C. Marichal and A. Sebald. X-{^{1}H, ^{19}F} triple resonance with a X-{^{1}H} CP MAS probe and characterisation of a ^{29}Si-^{19}F spin pair. *Solid State Nucl. Magn. Reson.* 23 (2003) 50–61.

[117] X. Helluy, R. Pietschnig and A. Sebald. ^{29}Si and ^{19}F MAS NMR spectra of isolated ^{29}Si(^{19}F)$_2$ and ^{29}Si(^{19}F)$_3$ spin systems: experiments and simulations. *Solid State Nucl. Magn. Reson.* 24 (2003) 286–300.

[118] J. P. Donoso, T. J. Bonagamba, P. L. Frare, N. C. Mello, C. J. Magon and H. Panepucci. Nuclear magnetic relaxation study of poly(propylene oxide) complexed with lithium salt. *Electrochim. Acta* 40 (1995) 2361–2363.

[119] P. Holstein, U. Scheler and R. K. Harris. Triple-channel solid-state NMR investigation of poly(vinylidene fluoride) polymorphs. *Mag. Reson. Chem.* 35 (1997) 647–649.

[120] J. Vaara, K. Oikarinen, J. Jokisaari and J. Lounila. Anisotropy of the ^{1}H and ^{13}C shielding tensors in chloroform. *Chem. Phys. Lett.* 253 (1996) 340–348.

[121] B. R. Appleman and B. P. Dailey. Fluorine shielding anisotropy in $CFCl_3$. *J. Magn. Reson.* 16 (1974) 265–273.

[122] S. G. Kukolich. Proton magnetic shielding tensors from spin-rotation measurements on H_2CO and NH_3. *J. Am. Chem. Soc.* 97 (1975) 5704–5707.

[123] T. Kupka, B. Ruscic and R. E. Botto. Hartree-Fock and density functional complete basis-set (CBS) predicted nuclear shielding anisotropy and shielding tensor components. *Solid State Nucl. Magn. Reson.* 23 (2003) 145–167.

[124] M. R. Baker, C. H. Anderson and N. F. Ramsey. Nuclear magnetic resonance antishielding of nuclei in molecules. Magnetic moments of ^{19}F, ^{14}N and ^{15}N. *Phys. Rev.* 133 (1964) A1533–1536.

[125] A. B. Harris, E. Hunt and H. Mayer. Anisotropy of the ^{19}F chemical shift of trapped CHF_3 and NF_3. *J. Chem. Phys.* 42 (1965) 2851–2862.

[126] C. Coupry, M. -T. Chenon and L. G. Werbelow. ^{13}C nuclear magnetic resonance study of the solution-state dynamics of benzene. *J. Chem. Phys.* 101 (1994) 899–904.

[127] M. Mehring, R. G. Griffin and J. S. Waugh. ^{19}F shielding tensors from coherently narrowed NMR powder spectra. *J. Chem. Phys.* 55 (1971) 746–755.

[128] C. S. Yannoni, B. P. Dailey and G. P. Ceasar. Studies of chemical shift anisotropy in liquid crystal solvents. IV. Results for some fluorine compounds. *J. Chem. Phys.* 54 (1971) 4020–4023.

[129] T. K. Halstead, H. W. Spiess and U. Haeberlen. ^{19}F and ^{1}H shielding tensors and crystal structure of 4,4'-difluorobiphenyl. *Mol. Phys.* 31 (1976) 1569–1583.

[130] K. Dorai and A. Kumar. Fluorine chemical shift tensors in substituted fluorobenzenes using cross correlations in NMR relaxation. *Chem. Phys. Lett.* 335 (2001) 176–182.

[131] Q. Chen and K. Schmidt-Rohr. ^{19}F and ^{13}C NMR signal assignment and analysis in a perfluorinated ionomer (Nafion) by two-dimensional solid-state NMR. *Macromolecules* 37 (2004) 5995–6003.

[132] C. Augustine and N. D. Kurur. Heteronuclear dipolar decoupling in liquid-crystal NMR using supercycled SW$_f$-TPPM sequences. *Magn. Reson. Chem.* 48 (2010) 798–803.

[133] A. J. Vega. Quadrupolar nuclei in solids. *Encyc. Nucl. Magn. Reson.* 6 (1996) 3869–3889.

[134] D. Freude. Quadrupolar nuclei in solid state nuclear magnetic resonance. *Encyc. Anal. Chem.* 10 (2000) 12188–12224.

[135] A. Jerschow. From nuclear structure to the quadrupolar NMR interaction and high-resolution spectroscopy. *Prog. Nucl. Magn. Reson. Spectrosc.* 46 (2005) 63–78.

[136] D. Massiot, F. Fayon, M. Capron, I. King, S. Le Calve, B. Alonso, J. Durand, B. Bujoli, Z. Gan and G. Hoatson. Modelling one- and two-dimensional solid-state NMR spectra. *Magn. Reson. Chem.* 40 (2002) 70–76.

[137] T. M. Gesing and W. Jeitschko. Crystal structure of aluminium carbide. *Z. Naturforsch.* 50b (1995) 196–196.

[138] T. Bräuniger, C. V. Chandran, U. Wedig and M. Jansen. NMR Chemical Shift and Quadrupolar Interaction Parameters of Carbon-Coordinated ^{27}Al in Aluminium Carbide, Al_4C_3. *Z. Anorg. Allg. Chem.* 637 (2011) 530–535.

[139] M. J. S. Dewar, D. B. Patterson and W. I. Simpson. A study of bonding in some organoaluminium compounds by ^{27}Al nuclear quadrupole resonance spectroscopy. *J. Chem. Soc., Dalton Trans.* (1973) 2381–2390.

[140] P. Blaha, K. Schwarz, G. K. H. Madsen, D. Kvasnicka and J. Luitz. *WIEN2k*, An Augmented Plane Wave + Local Orbitals Program for Calculating Crystal Properties. *ISBN 3–9501031–1–2* Techn. Universtät, Wien, Austria (2001).

[141] J. P. Perdew, K. Burke and M. Ernzerhof. Generalized Gradient Approximation Made Simple. *Phys. Rev. Lett.* 77 (1996) 3865–3868.

[142] K. Harindranath, K. A. Viswanath, C. V. Chandran, T. Bräuniger, P. K. Madhu, T. G. Ajithkumar and P. A. Joy. Evidence for the co-existence of distorted tetrahedral and trigonal bipyramidal aluminium sites in $SrAl_{12}O_{19}$ from ^{27}Al NMR studies. *Solid State Commun.* 150 (2010) 262–266.

[143] S. R. Jansen, H. T. Hintzen, R. Metselaar, J. W. de Haan, L. J. M. van de Ven, A. P. M. Kentgens and G. H. Nachtegaal. Multiple Quantum ^{27}Al Magic-Angle-Spinning Nuclear Magnetic Resonance Spectroscopic Study of $SrAl_{12}O_{19}$: Identification of a ^{27}Al Resonance from a Well-Defined AlO_5 Site. *J. Phys. Chem. B* 102 (1998) 5969–5976.

[144] L.-S. Du and J. F. Stebbins. Calcium and strontium hexaluminates: NMR evidence that "pentacoordinate" cation sites are four-coordinated. *J. Phys. Chem. B* 108 (2004) 3681–3685.

[145] S. M. Lee, E. Pippel, U. Gösele, C. Dresbach, Y. Qin, C. V. Chandran, T. Bräuniger, G. Hause and M. Knez. Greatly increased toughness of infiltrated spider silk. *Science* 324 (2009) 488–492.

[146] J.-B. d'Espinosa de Lacaillerie, C. Fretigny and D. Massiot. MAS NMR spectra of quadrupolar nuclei in disordered solids: The Czjzek model. *J. Magn. Reson.* 192 (2008) 244–251.

[147] D. R. Neuville, L. Cormier and D. Massiot. Al environment in tectosilicate and peraluminous glasses: A ^{27}Al MQ-MAS NMR, Raman, and XANES investigation. *Geochim. Cosmochim. Acta* 68 (2004) 5071–5079.

[148] G. Czjzek, J. Fink, F. Götz and H. Schmidt. Atomic coordination and the distribution of electric field gradients in amorphous solids. *Phys. Rev. B* 23 (1981) 2513–2530.

[149] R. N. Devi, P. Wormald, P. A. Cox and P. A. Wright. Novel pillared aluminum ethylene diphosphonate displaying reversible dehydration-rehydration behavior. *Chem. Mater.* 16 (2004) 2229–2237.

[150] A. Samoson, E. Lippmaa and A. Pines. High-resolution solid-state NMR averaging of 2^{nd}-order effects by means of a double-rotor. *Mol. Phys.* 65 (1988) 1013–1018.

[151] K. T. Müller, B. Q. Sun, G. C. Chingas, J. W. Zwanziger, T. Terao and A. Pines. Dynamic-angle spinning of quadrupolar nuclei. *J. Magn. Reson.* 86 (1990) 470–487.

[152] L. Frydman and J. S. Harwood. Isotropic spectra of half-integer quadrupolar spins from bidimensional magic-angle spinning NMR. *J. Am. Chem. Soc.* 117 (1995) 5367–5368.

[153] L. Frydman. Fundamentals of multiple quantum magic angle spinning NMR on half-integer quadrupolar nuclei. *Encyc. Nucl. Magn. Reson.* 9 (2002) 262–274.

[154] A. Goldbourt and P. K. Madhu. Multiple-quantum magic-angle spinning: high-resolution solid state NMR spectroscopy of half-integer quadrupolar nuclei. *Monatsh. Chem.* 133 (2002) 1497–1534.

[155] A. Goldbourt and P. K. Madhu. Multiple-quantum magic-angle spinning: high-resolution solid state NMR spectroscopy of half-integer quadrupolar nuclei. *Annu. Rep. NMR Spec.* 54 (2004) 81–153.

[156] S. P. Brown, S. J. Heyes and S. Wimperis. Two-dimensional MAS multiple-quantum NMR of quadrupolar nuclei. Removal of inhomogeneous second-order broadening. *J. Magn. Reson.* 119A (1996) 280–284.

[157] S.P. Brown and S. Wimperis. Two-dimensional multiple-quantum MAS NMR of quadrupolar nuclei. Acquisition of the whole echo. *J. Magn. Reson.* 124 (1997) 279–285.

[158] P. K. Madhu, O. G. Johannessen, K. J. Pike, R. Dupree, M. E. Smith and M. H. Levitt. Application of amplitude-modulated radiofrequency fields to the magic-angle spinning NMR of spin-7/2 nuclei. *J. Magn. Reson.* 163 (2003) 310–317.

[159] K. J. Pike, R. P. Malde, S. E. Ashbrook, J. McManus and S. Wimperis. Multiple-quantum MAS NMR of quadrupolar nuclei. Do five-, seven- and nine-quantum experiments yield higher resolution than the three-quantum experiment?. *Solid State Nucl Magn. Reson.* 16 (2000) 203–215.

[160] J. -P. Amoureux and J. Trébosc. Homogeneous broadenings in 2D solid-state NMR of half-integer quadrupolar nuclei. *J. Magn. Reson.* 179 (2006) 311–316.

[161] A. P. M. Kentgens and R. Verhagen. Advantages of double frequency sweeps in static, MAS and MQMAS NMR of spin I = 3/2 nuclei. *Chem. Phys. Lett.* 300 (1999) 435–443.

[162] D. Iuga, H. Schäfer, R. Verhagen and A. P. M. Kentgens. Population and coherence transfer induced by double frequency sweeps in half-integer quadrupolar spin systems. *J. Magn. Reson.* 147 (2000) 192–209.

[163] G. Wu, D. Rovnyak and R. G. Griffin. Quantitative multiple-quantum magic-angle-spinning NMR spectroscopy of quadrupolar nuclei in solids. *J. Am. Chem. Soc.* 118 (1996) 9326–9332.

[164] R. Siegel, T. T. Nakashima and R. E. Wasylishen. Sensitivity enhancement of NMR spectra of spin 3/2 nuclei using hyperbolic secant pulses. *Chem. Phys. Lett.* 403 (2005) 353–358.

[165] S. Vega and Y. Naor. Triple quantum NMR on spin systems with I = 3/2 in solids. *J. Chem. Phys.* 75 (1981) 75–86.

[166] P. K. Madhu, A. Goldbourt, L. Frydman and S. Vega. Sensitivity enhancement of the MQMAS NMR experiment by fast amplitude modulation of the pulses. *Chem. Phys. Lett.* 307 (1999) 41–47.

[167] A. Goldbourt, P. K. Madhu and S. Vega. Enhanced conversion of triple to single-quantum coherence in the triple-quantum MAS NMR spectroscopy of spin-5/2 nuclei. *Chem. Phys. Lett.* 320 (2000) 448–456.

[168] T. Bräuniger and P. K. Madhu. Fast amplitude-modulated pulse trains with frequency sweep (SW-FAM) in solid-state NMR of spin-7/2 nuclei. *J. Magn. Reson.* 193 (2008) 102–109.

[169] C. V. Chandran, J. Cuny, R. Gautier, L. Le Polles, C. J. Pickard and T. Bräuniger. Improving sensitivity and resolution of MQ-MAS spectra: A ^{45}Sc-NMR case study of scandium sulphate pentahydrate. *J. Magn. Reson.* 203 (2010) 226-235.

[170] A. Goldbourt and S. Vega. Signal enhancement in 5QMAS spectra of spin-5/2 quadrupolar nuclei. *J. Magn. Reson.* 154 (2002) 280–286.

[171] C. J. Pickard and F. Mauri. All-electron magnetic response with pseudopotentials: NMR chemical shifts. *Phys. Rev. B* 63 (2001) 245101-1–245101-13.

[172] P. E. Blöchl. Projector augmented-wave method. *Phys. Rev. B* 50 (1994) 17953–17979.

[173] G. K. Madsen, P. Blaha, K. Schwarz, E. Sjöstedt and L. Nordström. Efficient linearization of the augmented plane-wave method. *Phys. Rev. B* 64 (2001) 195134-1–195134-9.

[174] M. J. Duer. Determination of structural data from multiple-quantum magic-angle spinning NMR experiments. *Chem. Phys. Lett.* 277 (1997) 167–174.

[175] U. Friedrich, I. Schnell, S. P. Brown, A. Lupulescu, D. E. Demco and H. W. Spiess. Spinning-sideband patterns in multiple-quantum

magic-angle spinning NMR spectroscopy. *J. Magn. Reson.* 95 (1998) 1209–1227.

[176] M. Hanaya and R. K. Harris. Effects of ^{1}H-decoupling in two-dimensional multiple-quantum MAS NMR spectroscopy of ^{23}Na in a hydrous layered silicate. *Solid State Nucl Magn. Reson.* 8 (1997) 147–151.

[177] V. Lacassagne, P. Florian, V. Montouillout, C. Gervais, F. Babonneau and D. Massiot. Resolution enhancement in solid-state MQ-MAS experiments achieved by composite decoupling. *Magn. Reson. Chem.* 36 (1998) 956–959.

[178] S. Ganapathy, L. Delevoye, J. -P. Amoureux and P. K. Madhu. Heteronuclear dipolar decoupling effects on multiple-quantum and satellite-transition magic-angle spinning NMR spectra. *Magn. Reson. Chem.* 46 (2008) 948–954.

[179] Y. Millot and P. P. Man. Procedures for labeling the high-resolution axis of two-dimensional MQ-MAS NMR spectra of half-integer quadrupole spins. *Solid State Nucl Magn. Reson.* 21 (2001) 21–43.

[180] A. B. Ilyukhin and S. P. Petrosvants. Crystal structure of scandium sulfates $Sc_2(SO_4)_3.5H_2O$, $(C(NH_2)_3)_3[Sc(SO_4)_3].3H_2O$, and $[H_3N(CH_2)_6NH_3][Sc(H_2O)_2(SO_4)_2]_2.2H_2O$. *Russ. J. Inorg. Chem.* 49 (2004) 1232–1239.

[181] S. E. Ashbrook and S. Wimperis. Multiple-quantum cross-polarization and two-dimensional MQMAS NMR of quadrupolar nuclei. *J. Magn. Reson.* 147 (2000) 238–249.

[182] M. Pompetzki, L. van Wüllen and M. Jansen. The system $LiSO_3CF_3/RbSO_3CF_3$: phase diagram, solid state nuclear magnetic resonance investigations and ionic conductivity. *Z. Anorg. Allg. Chem.* 630 (2004) 484–490.

[183] L. van Wüllen, L. Hildebrandt and M. Jansen. Cation mobility and anion reorientation in lithium trifluoromethane sulfonate, $LiCF_3SO_3$. *Solid State Ionics* 176 (2005) 1449–1456.

[184] L. van Wüllen, N. Sofina, L. Hildebrandt, C. Mühle and M. Jansen. NMR studies of cation transport in the crystalline ion conductors of MCF_3SO_3 (M = Li, Na) and Li_7TaO_6. *Solid State Ionics* 177 (2006) 1665–1672.

[185] L. Ghassemzadeh, M. Marrony, R. Barrera, K. D. Kreuer, J. Maier and K. Müller. Chemical degradation of proton conducting perfluorosulfonic acid ionomer membranes studied by solid-state nuclear magnetic resonance spectroscopy *J. Power Sources* 186 (2009) 334–338.

[186] C. V. Chandran, G. Hempel and T. Bräuniger. ^{19}F-decoupling of half-integer spin quadrupolar nuclei in solid-state NMR: Application of frequency-swept decoupling methods. *Solid State Nucl Magn. Reson.* 40 (2011) 84–87.

[187] G. Scholz, M. Feist and E. Kemnitz. On the influence of humidity on the mechanochemical reaction between NaF and AlF_3. *Solid State Sciences* 10 (2008) 1640–1650.

[188] H. Yang, S. Ghose and D. M. Hatch. Ferroelastic phase transition in cryolite, Na_3AlF_6, a mixed fluoride perovskite: High temperature single crystal X-ray diffraction study and symmetry analysis of the transition mechanism. *Phys. Chem. Miner.* 19 (1993) 528–544.

[189] D. R. Spearing, J. F. Stebbins and I. Farnan. Diffusion and the dynamics of displacive phase transitions in cryolite (Na_3AlF_6) and chiolite ($Na_5Al_3F_{14}$): multi-nuclear NMR studies. *Phys. Chem. Miner.* 21 (1994) 373–386.

[190] V. Lacassagne, C. Bessada, D. Massiot, P. Florian and J. P. Coutures. High resolution NMR study of the mobility in solid cryolite Na_3AlF_6 from room temperature up to 300 degree C. *J. Chim. Phys.* 95 (1998) 322–326.

[191] C. Bessada and E. M. Anghel. ^{11}B, ^{23}Na, ^{27}Al and ^{19}F NMR study of solid and molten Na_3AlF_6-$Na_2B_4O_7$. *Inorg. Chem.* 42 (2003) 3884–3890.

[192] M. Kotecha, S. Chaudhuri, C. P. Grey and L. Frydman. Dynamic effects in MAS and MQMAS NMR spectra of half-integer quadrupolar nuclei: calculations and an application to the double perovskite cryolite. *J. Am. Chem. Soc.* 127 (2005) 16701–16712.

Curriculum Vitae

Personal data

Name : Vinod Chandran C.
Father's Name: Chandrasekharan Nair
Date of birth : 30.05.1982
Place of birth : Kerala, India

Schooling

1987-1991 : Lower-primary school, Kerala, India
1991-1994 : Upper-primary school, Kerala, India
1994-1996 : High school, Kerala, India
1996-1997 : Secondary school, Kerala, India

University studies

1997-1999 : Pre-degree, University of Kerala,
: Kerala, India
1999-2002 : B.Sc., University of Kerala,
: Kerala, India
2002-2004 : M.Sc., Mahatma Gandhi University,
: Kerala, India
2009-2011 : Ph.D., Universität Stuttgart,
: Stuttgart, Germany

Work experience

2004-2007 : Project assistantship,
: National Chemical Lab., Pune, India
2007-2009 : Research assistantship,
: Universität Halle, Halle, Germany

Hiermit erkläre ich an Eides statt, Dass ich diese Dissertation unter Verwendung der angegebenen Hilfsmittel selbstständig angefertigt und bisher noch keinen Promotionsversuch unternommen habe.

Stuttgart,
den 19.12.2011

Vinod Chandran C.